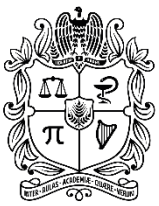

UNIVERSIDAD
NACIONAL
DE COLOMBIA

Application of Time-Frequency Transformations in Polarimetric Ultra-Wideband MIMO-GPR signals for Detection of Colombian Improvised Explosive Devices

Sergio Alonso Gutiérrez Duarte

Universidad Nacional de Colombia

Facultad de Ingeniería, Departamento de Ingeniería Eléctrica y Electrónica

Bogotá, Colombia

2019

Application of Time-Frequency Transformations in Polarimetric Ultra-Wideband MIMO-GPR signals for Detection of Colombian Improvised Explosive Devices

Sergio Alonso Gutiérrez Duarte

Tesis presentada como requisito parcial para optar al título de:

Doctor en Ingeniería, Ingeniería Eléctrica

Director:

José Félix Vega Stavro, Ph.D.

Línea de Investigación:

Electromagnetismo aplicado, Radar

Grupo de Investigación:

EMC-UN

Universidad Nacional de Colombia

Facultad de Ingeniería, Departamento de Ingeniería Eléctrica y Electrónica

Bogotá, Colombia

2019

A mi esposa María Alejandra, a mis padres y a mis hermanos.

¡Empecé un doctorado y encontré el amor!
Gracias María Alejandra por tu apoyo, comprensión, cariño y alegría
que me permitió tener tranquilidad y avanzar
durante todo este proceso.

¡Te amo!

Acknowledgements

I want to say thanks to a lot of people and institutions that helped me and gave me different kind of support during this research.

First of all, I want to give special thanks to my advisor, José Félix Vega Stavro, for guiding me into strategies to solve the problems that were presented and for his contributions to this research. I have special gratitude with people and researchers from Germany. Christoph Baer, thanks for your support, friendship and for helping me with the stay in Germany, which included assistance to access to important resources and facilities. My most sincere gratefulness to Jürgen Sachs and Thomas Just from the Technische Universität Ilmenau, for your pleasant collaboration and for our mathematical discussions. Thanks to all people in the Institute of Electronic Circuits of the Ruhr University Bochum on the head of Thomas Musch. My wife and I had good times there and good memories from Germany thanks to all of you. My gratitude with Professor David Koltick, to share your knowledge about neutron detectors, gamma rays, and to let me work within your research laboratory at the Purdue University.

Thanks to all members of the research group EMC-UN on the head of Francisco Roman, for your company and discussions during my studies, special thanks to David Martinez, for your collaboration during the permittivity measurements and field measurements. I would like to thank CENAM (Centro Nacional Contra Artefactos Explosivos y Minas), especially to CT Buitrago and ST Niño, for their assistance during the permittivity measurements, and for their security suggestions to perform measurements of explosives. I am also indebted to Ilmesens Gmbh for sponsoring the UWB-MIMO-system. And thanks to the Universidad Nacional de Colombia – Sede Bogota, for the assistance received from people and departments that are part of the research and investigation structure. Thanks to Janeth Alejandra Garcia, for your style corrections work.

Last but not least, thanks to Colciencias that provided me financial support with the fellowships 567 “Doctorados Nacionales de Colciencias” and 655 “Pasantias en la Universidad de Purdue 2014”.

Abstract

In this thesis, a new radar technique for GPR detection and discrimination of Improvised Explosive Devices is presented and validated. Data processing, consisting of adaptive filters and time-frequency transformations, are applied to polarimetric GPR data, in order to construct feature vectors of the targets. These vectors are used as inputs of a support vector machine algorithm, in order to discriminate buried targets either as improvised explosive device (IED) or clutter.

The main contributions of this thesis are as follows. First, the permittivity of improvised ANFO explosives is measured. This information is used for manufacturing inert surrogates of IEDs. Second, we proposed the construction of target feature vectors (TFVs) from polarimetric GPR measurements. Third, recursive algorithms and background removal are combined to improve the clutter removal. Data processing methods are assembled, combining clutter removal stage, time-frequency transformation and singular value decomposition. In total, eight data processing methods are proposed. Moreover, for every method, 13 TFVs are assembled. Then, the TFVs are used to train and test support vector machines (SVM) under a binary classification approach. Classification results are validated by using the leave-two-out cross-validation. Accuracy of 87.02% in the best classifier was obtained.

The main conclusion of this thesis is that combining polarimetric GPR measurements, feature extraction using time-frequency transformations, and SVM classifications allows obtaining discriminating features that improve the IED detection rates compared with metal detector performance. Furthermore, the proposed approach can be implemented in a hand-held detection device and to be used in a humanitarian demining scenario.

Keywords: Classification of improvised explosive devices, feature extraction, ground penetrating radar, permittivity of explosives, polarimetric measurements, support vector machines, ultra-wideband MIMO radar.

Resumen

En esta tesis, se presenta y valida una nueva técnica de radar para realizar mediciones GPR. Se proponen estructuras de procesamiento de datos GPR que utilizan filtros adaptativos y transformaciones tiempo-frecuencia como parte de la construcción de vectores de características de los objetos. Estos vectores son utilizados como entradas de un algoritmo de máquinas de soporte vectorial para discriminar los objetos enterrados como un artefacto explosivo improvisado (IED) o como un objeto aleatorio (Non-IED).

Los principales aportes de esta tesis son los siguientes. Primero, se mide y se reporta la permitividad de explosivos improvisados de tipo ANFO, información que posteriormente es usada para la fabricación de objetos inertes sustitutos de los IEDs. Segundo, se propone utilizar medidas polarimétricas GPR de objetos enterrados para la construcción de vectores de características (TFVs). Tercero, dentro de las técnicas de procesamiento de las medidas polarimétricas, se propone combinar los algoritmos recursivos y la supresión de señales de fondo para mejorar la eliminación de las señales no deseadas (clutter). Además, se ensamblan ocho métodos diferentes de procesamiento de señales, los cuales combinan la fase de eliminación del clutter, transformadas de tiempo-frecuencia y la descomposición de valores singulares. Adicionalmente, para cada método, se ensamblaron 13 TFVs. Posteriormente, se utilizan estos TFVs para entrenar y probar máquinas de soporte vectorial que funcionan bajo una estructura de clasificación binaria. Los resultados de clasificación son corroborados utilizando la validación cruzada *leave-two-out* (“dejar dos fuera”). El mejor clasificador que se obtuvo tiene una exactitud de 87.02%.

La principal conclusión de esta tesis es que al combinar las medidas GPR polarimétricas, la extracción de características mediante transformaciones tiempo-frecuencia y las máquinas de soporte vectorial, se pueden obtener características discriminatorias que mejoran las tasas de detección de IEDs, en comparación con un detector de metales. Adicionalmente, el enfoque propuesto puede ser implementado en un dispositivo de detección portátil y usarse en un escenario de desminado humanitario.

Palabras clave: Clasificación de artefactos explosivos improvisados, extracción de características, radar de penetración terrestre, permitividad de explosivos, máquinas de soporte vectorial, medidas polarimétricas, radar MIMO de banda ultra ancha.

Contents

Page.

List of figures

Page.

List of tables

Page.

List of Abbreviations

AN	Ammonium Nitrate
ANFO	Ammonium Nitrate and Fuel Oil
APL	Anti-Personnel Landmine
ATM	Anti-Tank Mine
BaTiO3	Barium Titanate
CWT	Continuous Wavelet Transform
EED	Electro Explosive Device
ERW	Explosives Remnants of War
FN	False Negatives
FNR	False Negative Rate
FP	False Positives
FPR	False Positive Rate
FT	Fourier Transform
GPR	Ground Penetrating Radar
IED	Improvised Explosive Device
IFT	Inverse Fourier Transform
IR	Impulse Response
LPC	Linear-Predictive-Coding
LTI	Linear Time-Invariant
MIMO	Multiple Inputs Multiple Outputs
MRE	Mine Risk Education
MUT	Material Under Test
Non-IED	Non-Improvised Explosive Device / Clutter object
RLS	Recursive Least-Squares
Rx	Receiver/Reception
SFCW	Stepped-Frequency Continuous-Wave
SVD	Singular Value Decomposition
SVM	Support Vector Machines
TFV	Target Feature Vector
TN	True Negatives
TP	True Positives
TPR	True Positive Rate/Recall
TRL	Through-Reflection-Line
Tx	Transmitter/Transmission

UWB	Ultra-Wide Band
UXO	Unexploded Ordnance
VNA	Vector Network Analyzer
VOIED	Victim-Operated Improvised Explosive Device
WVD	Wigner-Ville-Distribution

1. Introduction

This chapter summarizes the different types of improvised explosives devices that can be found in Colombia and constitute a humanitarian problem. Furthermore, the humanitarian actions against the mine problem that are developed by the Colombian government and civilian organizations are explained. Additionally, the use of ground penetrating radar for landmine detection is described. Finally, the objectives and framework of this thesis are presented.

1.1 Demining problem in Colombia

1.1.1 Improvised explosive devices

An Improvised Explosive Device is defined in the International Mine Action Standards (IMAS 4.10) as “a device placed or fabricated in an improvised manner incorporating explosive material, destructive, lethal, noxious, incendiary, pyrotechnic materials or chemicals designed to destroy, disfigure, distract or harass. It may incorporate military stores, but is normally devised from nonmilitary components” [1].

As minimum, an IED is composed of: a switch, a power source, an initiator, a container and explosives [2]. Being a nonstandard object, IEDs have variable characteristics, for example, the casing can be a plastic pipe, a wooden case, a glass bottle or a plastic can. These explosive devices can have significant amounts of dielectric material, such as plastic beads, stones, bamboo, glass and other nonmetallic parts used as shrapnel. IEDs can be classified by their kind of activation as: timed, commanded, and victim-operated (VOIED) [2]. Depending on the design, an IED can fit within the definition of Anti-personnel landmine (APL) and Anti-tank mine (ATM). Sometimes, based on the IEDs physic characteristics, local names are used to identify IEDs.

In general terms, “an IED may meet the definition of a mine, booby trap, and/or other type of explosive ordnance depending on its construction. These devices may also be referred to as

improvised, artisanal, or locally manufactured mines, booby traps, or other types of explosive ordnance" [1].

Figure 1-1 shows Colombian IEDs seized by the army from March 2013 until March 2014, according to the data processed from the Colombian army news [3] by EMC-UN research group. In this data, IEDs with no name in the news or reports are labeled as unidentified. We can see that from a total of 10729 seized IEDs, the VOIED or APL is the most common IED with 73%.

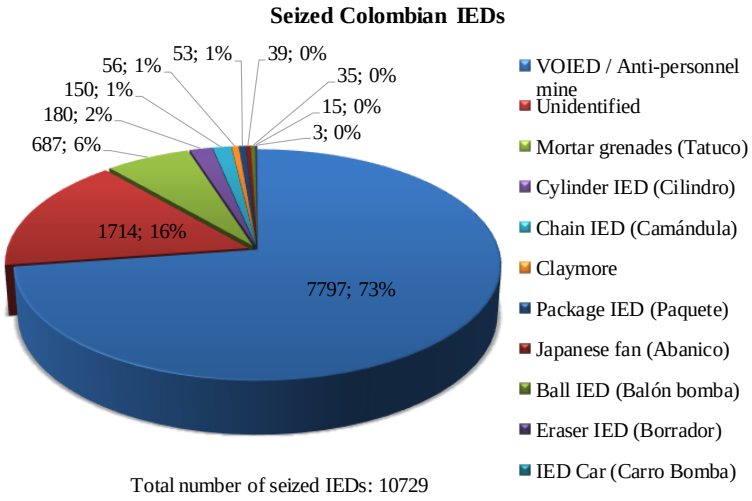

Figure 1-1: Seized IEDs, data processed from Colombian army news (March 2013-2014) by EMC-UN research group.

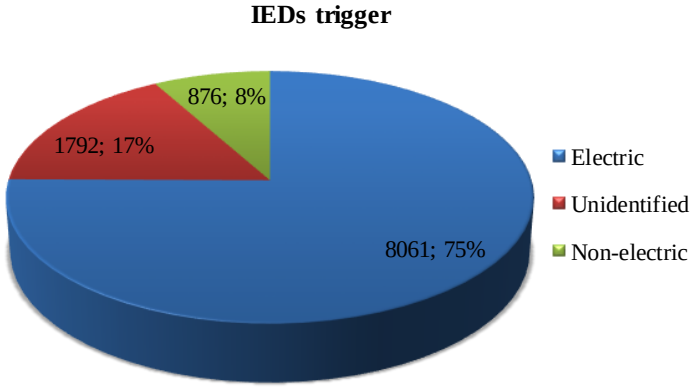

Figure 1-2: Initiation mechanism of seized IEDs. Data processed from Colombian army news (March 2013-2014.) by EMC-UN research group.

Related with activation mechanism of landmines, reports of demining activities, news and military information show that IED initiation mechanisms used by illegal groups in Colombia can vary between electric and non-electric, as shown in Figure 1-2. Moreover, researchers have found that an

electro-explosive device (EED) is a common element in the IED activation mechanism and the IED main charge usually is ammonium nitrate and fuel-oil (ANFO) [4], [5]. In summary, in Colombia there are a huge variability on IEDs shapes, materials and triggering methods. However, most IEDs have two common factors: ANFO as the main explosive charge and the EED as the trigger of the IED. Models of electrically activated IEDs are shown in Figure 1-3.

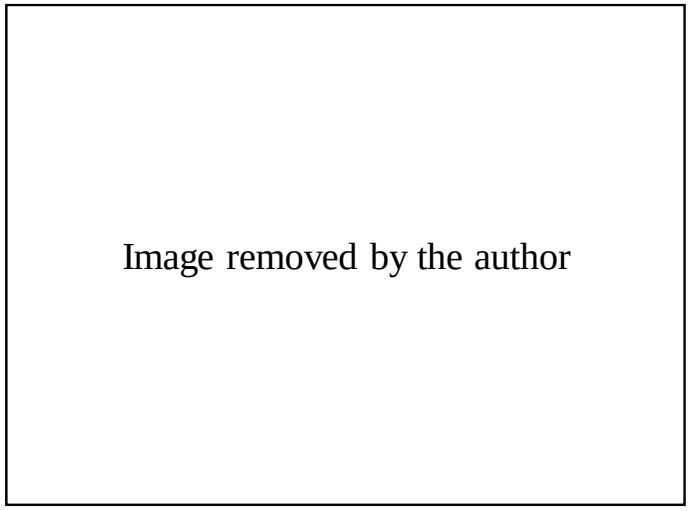

Figure 1-3: Models of an IED activated electrically. Source: Author

1.1.2 Humanitarian demining action

The Colombian government has implemented the so-called “Acción integral Contra Minas Antipersonal - AICMA”. It is a presidential program for the integral action against anti-personnel mines, which involves the following activities: Mine Risk Education (MRE) and risk prevention activities; assistance for APL, IED, unexploded ordnance (UXO), or explosive remnants of war (ERW) victims; and humanitarian demining. The AICMA program is on charge of the Department for Comprehensive Action Against Antipersonnel Mines (Dirección para la Acción Integral contra Minas Antipersonal – Descontamina Colombia) [4].

The statistics of the Colombian government indicate that between 1990 and 31 of March 2019, 11735 persons have been victims of IEDs/ERW [4], [6]. The year with most victims was 2006 with 1228 victims [4]. In 2018, 136 persons were IEDs victims, from which 80 were civilian and 56 militaries [6].

The IEDs and ERW casualties have been recorded in all the 32 departments and nearly all casualties have been caused by a VOIED that acts like antipersonnel landmine [7]. These mine/ERW casualties are referred to as anti-personnel mines in the casualty data for Colombia [4], [7].

Regarding humanitarian demining, it starts with a pilot project in August 2015, after the peace agreement between the government and the non-state armed group, Revolutionary Armed Forces of Colombia – FARC. Moreover, a global demining initiative for Colombia was launched in 2016 and supported by 12 donors [8]. Nowadays, humanitarian demining operations are running with the aim to identify, define and remove all contamination or suspicion of IEDs, UXO or other ERW in Colombia. Results of mine clearance in 2017 are reported in Table 1-1, which was extracted from [9]. Further statistics of humanitarian demining can be found in [10].

Table 1-1: Mine clearance in 2017 [9].

Department	Operator	Areas cleared	Area cleared (m^2)	IED/APL destroyed	UXO destroyed
Antioquia	BRDEH	21	62,325	31	3
Antioquia	HALO	12	60,2	21	0
Bolivar	AEDIM	8	30,39	0	1
Caldas	BRDEH	6	33,798	35	1
Caquetá	BRDEH	10	29,515	2	0
Cauca	HI	1	408	0	0
Huila	CCCM	1	3,591	0	0
Meta	BRDEH	5	31,09	3	1
Meta	CCCM	1	1,426	0	0
Meta	HALO	14	81,904	6	0
Santander	BRDEH	1	150	2	0
Tolima	BRDEH	4	8,298	4	6
Tolima	HALO	9	40,856	0	0
Totals		93	383,951	104	12

In order to develop the Comprehensive Action Against Antipersonnel Mines (AICMA), Colombia adopted national mine actions standards, which include standards on IED/UXO clearance and explosive ordnance disposal [9], [11], [12]. Among the national operating standards, three stages are defined in humanitarian demining: non-technical survey, technical survey and clearance.

The demining techniques, defined in the clearance stage, can be manual demining, mechanical demining and mine detection dogs [12]. Since the most common IED has EED as trigger, then the metal detector is the detection method used to localize metallic parts inside the IEDs. However, dual sensors such as metal detector combined with ground penetrating radar (GPR) can be used as a detection method [13]. Demining techniques must inspect the 100% of the territory of a suspected or confirmed hazardous area in order to clear all the IEDs and UXO for 13 cm depth [13].

1.2 Ground penetrating radar for landmine detection

Humanitarian and military demining projects have been launched to detect and neutralize mines, IEDs, UXO and ERW, as summarized in [14]–[16]. Among the reported demining detection techniques, there are metal detectors, GPR, acoustic sensors, biosensors (artificial nose), impedance tomography, neutron backscattering, X-ray backscattering, nuclear quadrupole resonance, and others that use biological subjects such as dogs, rats, bees, and bacteria. Currently, metal detectors and GPR have already been implemented as detection techniques for manual clearance in humanitarian demining [14], [17].

GPR is a system that can irradiate electromagnetic waves below the earth surface and can detect buried objects [18]. The electromagnetic waves emitted by GPR propagates through the soil. The interaction between electromagnetic waves and the objects located in the illuminated area by the radar produce an echo signal that propagates back to the surface (backscattered). This signal can be detected by an antenna radar receiver and processed to have underground maps or information related to buried objects [19]. Furthermore, in the demining context, GPR allows to detect both metallic and nonmetallic targets in a noninvasive way [16], [20]. Therefore, a GPR-based system can be combined later with metal detectors in order to improve detection and false alarm rate.

In general, landmine detection with GPR consists of three stages. The first stage is data acquisition and processing, whose aims are to measure the backscattered signal of the targets of interest and to decrease unwanted return signals, known as clutter, such as multiple reflections between ground and antenna, ground reflections and antenna effects, among other. Several methods have been applied to remove the clutter effects, such as modeling the clutter and the soil heterogeneity, background removal, filtering, wavelet reconstruction, deconvolution and other techniques described in [16], [21]–[27].

In the second stage, called radar imaging, an image is generated with the aim to detect a region of interest or any image anomalies where mines or clutter objects are localized. Researches on GPR have proposed imaging techniques such as Synthetic Aperture Radar SAR-algorithms, hyperbole identification, time domain migration techniques, propagation models or nonlinear inversion models to create maps in two or three dimensions [22], [28]–[31].

The third stage is decision making, which is required to discriminate the targets between mines and other objects present in the soil. Usually, target discrimination is performed using target features by a classification approach. These features, such as characteristic frequencies, eigenvalues and energy density spectrum, are extracted from the target measurements by using SEM, joint time-frequency-domain representation or PCA [32]–[34]. Consequently, in order to provide more features from the measurements and improve the classification performance, the combination of the described target features is used. However, polarimetric properties of the targets can also be considered to increase the number of features by using a GPR array, as described in [35], [36].

1.3 Objectives

Landmine detection techniques have been proposed for standard APLs, UXOs and ATMs. However, due to variability in the composition, size, shape of the Colombian IEDs, and its similarity with clutter objects (Non-IEDs), classification of both types of targets is challenging in the frame of humanitarian demining. Therefore, this thesis is focused on finding target features, extracted from GPR measurements, that can be used to discriminate between Colombian IEDs and clutter objects. Moreover, it performs validation processes to verify if those target features can be considered for humanitarian demining.

The main goal of this thesis is to establish the discriminating features identifying Improvised Explosive Devices used in Colombia.

The secondary objectives of this work are:

- To extract the features of a common IED from their backscattered signal.
- To develop a method in order to identify IEDs in the detected targets.
- To evaluate the efficiency of the proposed method to discriminate Colombian IEDs in a controlled environment.

1.4 Thesis Framework

This thesis has been supported by the EMC-UN research group of the Universidad Nacional de Colombia – Sede Bogotá and has received scientific cooperation from the Institute of Electronic Circuits of the Ruhr University Bochum, the Technische Universität Ilmenau and los Andes University. Moreover, this thesis received the financial support of the fellowship 567 "Doctorados Nacionales de Colciencias" and was developed in the framework of the Colciencias Project 573-2015 "Humanitarian Microwave Detection of Improvised Explosive Devices in Colombia (MEDICI)".

MEDICI is a scientific cooperation project between Colombian and German Universities: Universidad Nacional de Colombia – Sede Bogotá and Universidad de los Andes from Colombia, and Ruhr University Bochum and Technische Universität Ilmenau from Germany. The project aims to contribute to the solution of a humanitarian problem by the development of new IEDs detection technologies for specific Colombian constraints like the non-standardized IEDs and the challenging soil and environmental conditions.

In this thesis, the dual-polarized Vivaldi antennas and the multi-channel ultra-wideband M-Sequence device, which were developed in the MEDICI project by the German partners, are used to assembly a UWB-MIMO-GPR and perform polarimetric GPR measurements. Additionally, the M-sequence device is used in the proposed field-deployable system for the measurement of permittivity in improvised explosives.

2. Complex-permittivity measurements of ANFO-type improvised explosives[1]

In this chapter, the permittivity of improvised ANFO explosives is measured and reported. These measurements contribute to the knowledge and characterization of Colombian IEDs. Furthermore, these measurements are used for manufacturing inert materials and inert surrogates of IEDs. Then, these devices are used as test objects in GPR measurements, as described in chapter 3.

The measured permittivity can be afterward inserted in theoretical calculations, algorithms and electromagnetic simulations.

Part of the information and results presented in this chapter were previously published in [37] by the author of this thesis. The paper was entitled "Field-Deployable System for the Measurement of Complex Permittivity of Improvised Explosives and Lossy Dielectric Materials". It was the result of the research developed by the main author and it was developed under the guidance and advising of the co-authors.

2.1 Introduction

A typical Colombian Improvised Explosive Device (IED) is composed of a main explosive, an electric detonator, a switch (made to be accidentally operated by victims), and a dielectric casing (generally a plastic pipe, a wooden case, a glass bottle or a plastic can) [38]. Usually, the primary

[1] Part of the results shown in this chapter was published in S. Gutierrez, T. Just, J. Sachs, C. Baer, and F. Vega, 'Field-Deployable System for the Measurement of Complex Permittivity of Improvised Explosives and Lossy Dielectric Materials', IEEE Sensors Journal, vol. 18, no. 16, pp. 6706–6714, 2018. DOI: 10.1109/JSEN.2018.2849322.

explosive is manufactured by mixing ammonium nitrate, extracted from fertilizers, and fuel oil. This mixture is known as ANFO.

Due to the dissimilarity of the manufacturing process, permittivity measurements of ANFO are of interest for GPR. Measuring this parameter could serve as an identification mechanism aimed to fingerprint the explosive.

In this research, we measure the complex permittivity of improvised explosives made of Ammonium Nitrate-Fuel Oil (ANFO). Moreover, this knowledge is applied in manufacturing inert surrogates of IEDs, as explained in Appendix A, which are used in this research as test objects for laboratory and field GPR measurements.

In order to approach a field deployable and cost-efficient measurement concept, we have developed a measurement procedure that avoids the use of vector network analyzers [37]. Instead, the S-parameters of the specimen holder containing the explosive sample are calculated from time domain measurements.

This chapter is organized as follows. First of all, the method for estimation of the permittivity of bulk materials is described in section 2.2. Second, the proposed method is explained in section 2.3. Then, the measurement setup is described in section 2.4, and the measurements procedure is validated in section 2.5. Finally, the measurements of the dielectric constant of several types of ANFO are presented and discussed in section 2.6.

2.2 Permittivity estimation of bulk materials

The permittivity estimation of bulk materials within the microwave range, or dielectric spectroscopy, is a task typically performed measuring the S-parameter of a sample of the material, using resonant methods or transmission/reflection line methods [39], [40]. The measurements techniques can either use calibration-dependent [39]–[42] or calibration-independent techniques [43]–[46].

Open-ended coaxial probe and cavity resonators were used in [47] to measure the permittivity of secondary high explosives (explosives with medium sensitivity to external stimuli as trinitrotoluene (TNT), and the nitramide RDX) at frequencies between 1 and 18 GHz. Cavity resonators were also used in [48] to calculate the permittivity of neat explosives (explosives in pure form as TNT, RDX,

nitroamine high explosive HMX, and pentaerythritol tetranitrate (PETN)) at 10 GHz. In [49], a coaxial waveguide was used to measure the permittivity of improvised explosives between 0.375-3 GHz.

The described permittivity measurement methods are constrained to specific frequencies, materials, or applications. The open-ended coaxial probe is suitable for liquids or semi-solid materials with no air inclusions on it. Cavity resonators are very accurate for narrowband measurements. Nevertheless, this method requires the use of a VNA with high-frequency resolution. The coaxial waveguide has been used to measure low-loss and lossy materials in the broadband range. However, the accuracy is limited by the air-gaps between the Material Under Test (MUT) and the fixture electrodes, and half-wavelength resonances [41], [50]. All these measurements techniques are performed under laboratory conditions, with the aid of an expert in electromagnetic theory.

2.3 Proposed method

We propose a method that can be used for field measurement scenarios, (e.g., fingerprinting the explosives on the field and calibrating detection devices as GPRs), where broadband permittivity measurements of solids/granular explosives are required. Moreover, the method can be implemented by technicians with few or no background in electromagnetic theory.

2.3.1 Derivation

The permittivity of the material is estimated from the measured Scattering parameters of a coaxial specimen holder containing the material. The S-parameters are calculated from time domain measurements, performed using an M-sequence device. The setup is depicted in Figure 2-1.

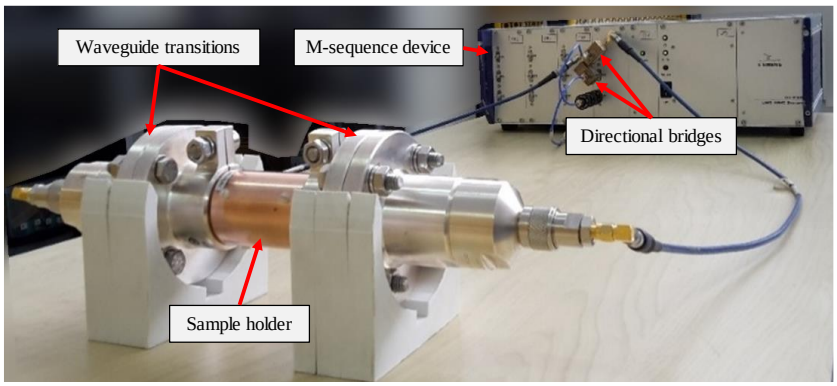

Figure 2-1: Measurement setup based on a coaxial sample holder and an M-sequence device.

The longitudinal cross-section of the coaxial specimen holder is presented in Figure 2-2. As it can be seen, the space between the inner and outer conductor is filled with the MUT. The measured permittivity frequency range is limited by the cut-off frequency f_c, e.g. using the diameters of the coaxial specimen holder, $d_1 = 38.8$ mm and $d_2 = 16.9$ mm, the cut-off frequency for a PTFE sample with $\varepsilon_r' = 2$ is $f_c = 2.42$ GHz, which can be calculated using Equation (2.1), assuming $\mu_r = 1$ [41]:

$$f_c = \left[190.85 \Big/ \left((d_1 + d_2)(\varepsilon_r')^{1/2} \right) \right] (\text{GHz}), \tag{2.1}$$

$$\varepsilon_r = \varepsilon_r' + j\varepsilon_r'', \tag{2.2}$$

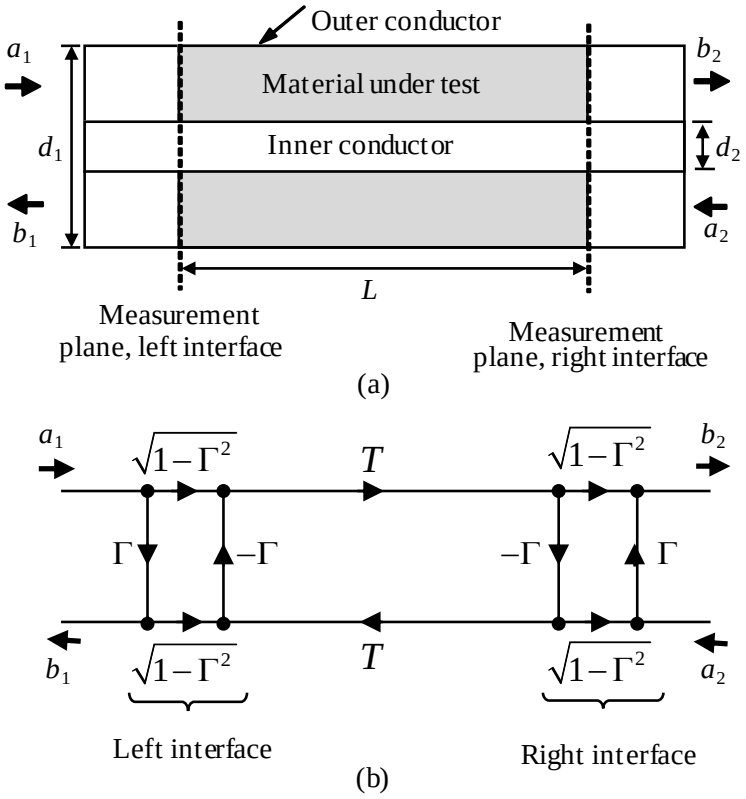

Figure 2-2: Coaxial line. (a) Longitudinal cut view of a specimen holder, (b) Mason-graph of wave propagation. a and b are incident or emanating normalized waves.

where d_1 and d_2 represent the diameters of the outer and inner conductor of the coaxial, respectively; ε_r is the relative complex permittivity with real part ε_r', and imaginary part $\text{Im}(\varepsilon_r) \leq 0$.

The measurable quantity of the specimen holder is its S-matrix (2.3):

$$\mathbf{S}_{MUT} = \begin{bmatrix} S_{11} & S_{12} \\ S_{21} & S_{22} \end{bmatrix}; S_{ij} = \left[b_j / a_i \right]\Big|_{a_{j\neq i}=0}, \quad i, j = 1, 2. \tag{2.3}$$

Symbols in capital letters refer to complex-valued frequency domain quantities, and bold symbols are matrices.

Assuming a coaxial specimen holder, filled with homogeneous material, the wave propagation can be modeled by a Mason-graph as shown in Figure 2-2. Consequently, the $\mathbf{S}_{MUT}$ parameters related to measurement planes can be expressed as:

$$S_{11} = S_{22} = \Gamma\left(1 - T^2\right) \Big/ \left(1 - \Gamma^2 T^2\right), \tag{2.4}$$

$$S_{12} = S_{21} = T\left(1 - \Gamma^2\right) \Big/ \left(1 - \Gamma^2 T^2\right), \tag{2.5}$$

where Γ represents the frequency-dependent complex reflection coefficient at the interface air to MUT. This parameter is related to the relative permittivity of the MUT by (2.6):

$$\Gamma = \left(1 - \left(\varepsilon_r\right)^{1/2}\right) \Big/ \left(1 + \left(\varepsilon_r\right)^{1/2}\right). \tag{2.6}$$

T is the transmission coefficient of the bulk material, given by [41]:

$$T = \exp\left[-j 2\pi f \left(\varepsilon_r\right)^{1/2} \left(L / c_0\right) \right], \tag{2.7}$$

where L is the length of the MUT probe and c_0 is the vacuum speed of light.

Several methods have been applied in order to extract ε_r from the S-parameters in Equations (2.4) and (2.5), see e.g. [41]. In this paper, we apply a direct method based on the solutions of equations (2.4), (2.5), (2.6), and (2.7) as follows:
Solving (2.4) for Γ reads,

$$\Gamma = \frac{-1 + T^2 \pm \left(1 - 2T^2 + 4{S_{11}}^2 T^2 + T^4\right)^{1/2}}{2 S_{11} T^2}, \tag{2.8}$$

substituting any of the two Γ solutions into (2.5), we obtain

$$T_{(1,2)} = \frac{1 - {S_{11}}^2 + {S_{21}}^2 \pm \left(\left(1 - {S_{11}}^2 + {S_{21}}^2\right)^2 - \left(2 S_{21}\right)^2\right)^{1/2}}{2 S_{21}}. \tag{2.9}$$

Solving (2.5) for T and replacing it into (2.4), we get

$$\Gamma_{(1,2)} = \frac{1 + S_{11}{}^2 - S_{21}{}^2 \pm \left(\left(1 - S_{11}{}^2 + S_{21}{}^2\right)^2 - \left(2S_{21}\right)^2 \right)^{1/2}}{2S_{11}}. \tag{2.10}$$

Rearranging for two port measurement, assuming $S_{11}{}^2 = S_{11}S_{22}$ and $S_{21}{}^2 = S_{21}S_{12}$, we can simplify (2.9) and (2.10) as:

$$\Gamma_{(1,2)} = \frac{1 + \det\left(\mathbf{S}_{MUT}\right) \pm \left(\left(1 - \det\left(\mathbf{S}_{MUT}\right)\right)^2 - (2S_{21})^2 \right)^{1/2}}{2S_{11}}, \tag{2.11}$$

$$T_{(1,2)} = \frac{1 - \det\left(\mathbf{S}_{MUT}\right) \pm \left(\left(1 - \det\left(\mathbf{S}_{MUT}\right)\right)^2 - (2S_{21})^2 \right)^{1/2}}{2S_{21}}, \tag{2.12}$$

where $\det\left(\mathbf{S}_{MUT}\right)$ means the determinant of matrix $\mathbf{S}_{MUT}$.

From this, the permittivity can be calculated by two methods. In Method 1, the permittivity is calculated via inversion of Γ in Equation (2.6). The relative complex permittivity can be expressed as:

$$\begin{aligned} \left(\boldsymbol{\varepsilon}_r\right)^{1/2} &= \mathbf{Y} = \left(1 - \boldsymbol{\Gamma}\right) \big/ \left(1 + \boldsymbol{\Gamma}\right), \quad \mathbf{Y} \in \mathbb{C}, \\ \boldsymbol{\varepsilon}_r &= \left|\mathbf{Y}\right|^2 \exp\left[j2(\arg(\mathbf{Y})) \right], \end{aligned} \tag{2.13}$$

where $\mathbf{Y}$ is the normalized admittance of MUT, and $\arg(\mathbf{Y})$ is the argument of $\mathbf{Y}$.

In Method 2, ε_r is calculated directly from T in Equations (2.7) and (2.12) as follows:

$$\boldsymbol{\varepsilon}_r = \left[-\left(c_0^2 \left(\ln\left|\boldsymbol{T}\right| + j\overline{\arg(\mathbf{T})} \right)^2 \right) \Big/ (2\pi fL)^2 \right], \tag{2.14}$$

where $\overline{\arg(\mathbf{T})}$ is the phase-unwrapping term of $\arg(\mathbf{T})$. Notice that the logarithm of the complex elements in T has an imaginary part with an infinite number of roots, defined by the argument of the complex number plus $2m\pi$, where m is an integer [51]. We solved the phase ambiguity for ε_r (absolute jumps greater than π radians) by applying phase-unwrapping to $\arg(\mathbf{T})$ [51], [52].

Regarding the sign of ambiguity in (2.11) and (2.12), we selected the correct root by satisfying the passivity conditions $\left|\Gamma\right| \le 1$ and $\left|T\right| \le 1$ for Γ and T, respectively.

2.3.2 Calibration and de-embedding

The mechanical transitions adapting the standard SMA RF connectors and the coaxial specimen holder depicted in Figure 2-1, are represented in the two-port network diagram presented in Figure 2-3. A de-embedding procedure was put in place, in order to eliminate the effect of the transitions in the measurement.

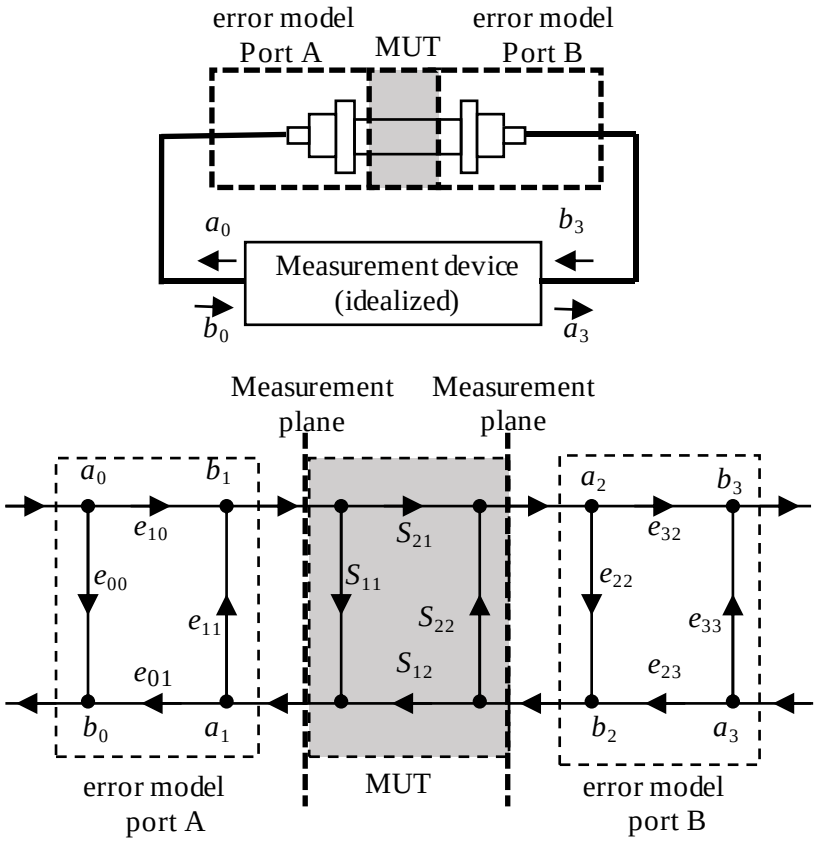

Figure 2-3: Mason-graph of the measurement set-up.

Using transmission parameters, the measured matrix $\mathbf{T}_M$ can be expressed as:

$$\mathbf{T}_M = \mathbf{T}_A \mathbf{T}_{MUT} \mathbf{T}_B, \tag{2.15}$$

where $\mathbf{T}_A$ and $\mathbf{T}_B$ represent the T-parameters of the transitions A and B, respectively and $\mathbf{T}_{MUT}$ represents the transmission matrix of the coaxial specimen holder.

From this, $\mathbf{T}_{MUT}$ can be calculated from:

$$\mathbf{T}_{MUT} = \mathbf{T}_A^{-1} \mathbf{T}_M \mathbf{T}_B^{-1} = \begin{bmatrix} T_{11} & T_{12} \\ T_{21} & T_{22} \end{bmatrix}, \tag{2.16}$$

the $\mathbf{S}_{MUT}$ matrix can be calculated using [53]:

$$\mathbf{S}_{MUT} = \frac{1}{T_{22}}\begin{bmatrix} T_{12} & \det(\mathbf{T}_{MUT}) \\ 1 & -T_{21} \end{bmatrix}. \tag{2.17}$$

In order to determine $\mathbf{T}_A$ and $\mathbf{T}_B$, we selected the TRL-calibration procedure (Through-Reflection-Line) using an eight-error term model [53].We performed a set of two port measurements of a through-connection $\mathbf{S}_{M\_Through}$, a symmetric reflection $\mathbf{S}_{M\_Reflect}$, and a line $\mathbf{S}_{M\_Line}$.

The theoretical S-parameters of the transitions are:

$$\begin{aligned} &\mathbf{S}_{Through} = \begin{bmatrix} 0 & 1 \\ 1 & 0 \end{bmatrix},\ \mathbf{S}_{Reflect} = -\begin{bmatrix} 1 & 0 \\ 0 & 1 \end{bmatrix}, \\ &\mathbf{S}_{Line} = \exp\left[\left(-j2\pi fL_{Line}\right)/c_0\right]\begin{bmatrix} 0 & 1 \\ 1 & 0 \end{bmatrix}. \end{aligned} \tag{2.18}$$

The de-embedding requires, therefore, solving (2.18) in conjunction with $\mathbf{S}_{M\_Through}$, $\mathbf{S}_{M\_Reflect}$, $\mathbf{S}_{M\_Line}$, which yields 12 independent equations. Detailed information about the process can be found in [53].

Figure 2-4 depicts the longitudinal cut view of the sample holder and the TRL-calibration standards. The sample holder is built with two copper tubes forming a coaxial specimen holder. The actual length of the MUT sample is 30 mm and the length of the Line-calibration standard is 45 mm. Two acryl glass disks, machined using a CNC, center the inner conductor and limit the MUT volume. Furthermore, the coaxial specimen holder must be symmetric within the measurement planes, whereas the coaxial adapters left and right could be asymmetric since they are described by two different matrices $\mathbf{T}_A$ and $\mathbf{T}_B$. However, due to ease of manufacturing, we preferred symmetrical coaxial components at the left and right of the reference plane. Proper machining was required because scratches and metallic residues might lead to errors in permittivity calculations. Moreover, machining inaccuracies modify the reference-plane position and impedance coupling, which may reduce the accuracy of permittivity determination.

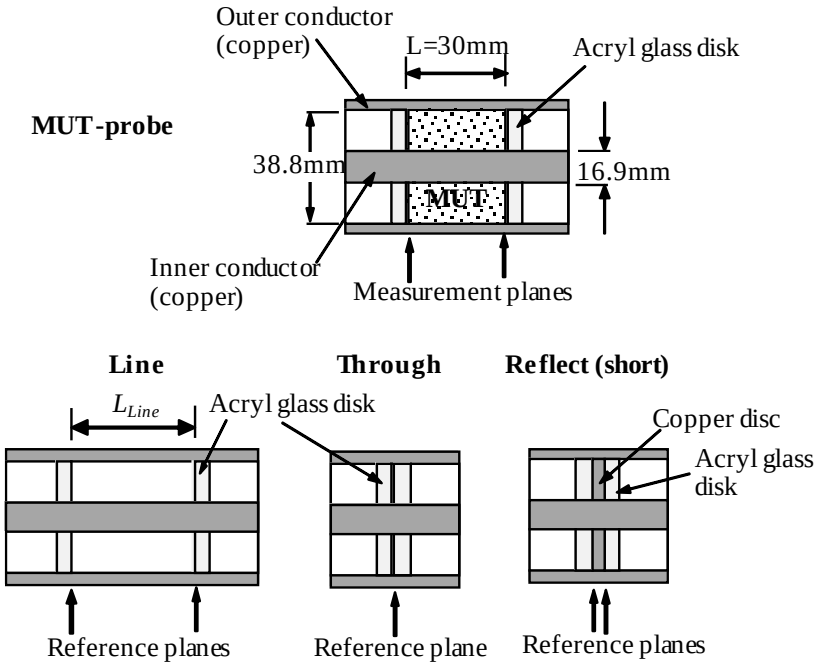

Figure 2-4: Longitudinal cut view of the MUT-probe and TRL-calibration standards.

Notice that, after calibration, the position of the measurement plane is the same of the calibration plane. Therefore, the equations (2.11) and (2.12) are reference-plane-dependent.

2.4 Measurement setup

The measurement was performed using an ultra-wideband M-sequence device, m:explore®, from Ilmsens. This device estimates the S-parameter from time domain measurements, based on the concept presented in [54], [55]. The basic device structure is depicted in Figure 2-5.

The measurement setup based on a minimal configuration is depicted in Figure 2-6. Two of the units described in Figure 2-5 were used synchronized by the same RF-clock.

The RF-clock generates a frequency f_c =12 GHz, whose stability determines largely the properties of the M-sequence device. In order to reach the impulse response of the MUT, the linear feedback shift register provides an ultra-wideband M-sequence [21]. This signal acts as stimulus ($m_1(t)$ and $m_2(t)$) of the specimen holder. By enabling/disabling the shift register, the stimulus is applied to port A or port B in the specimen holder and its response is $v_1(t)$ or $v_2(t)$, as depicted in Figure 2-6.

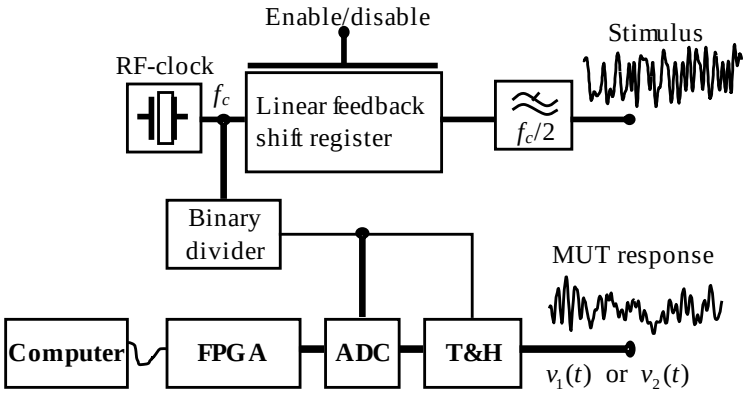

Figure 2-5: Block schematic of the ultra-wideband pseudo-noise sensor.

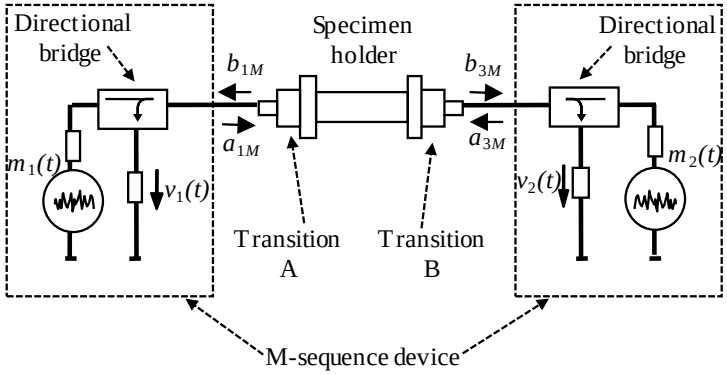

Figure 2-6: Setup to measure the scattering parameters of the MUT. The reference of the directional bridges is BDCA-10-25+.

The M-sequence is an ultra-wideband CW signal of low power (about 200 mV peak voltage and –8 dBm maximum power). According to the criteria of the explosive expert from the Colombian Army involved in the preparation of the samples, this power level is safer for measurements.

The capturing of the MUT response (i.e. reflection and transmission) is done in parallel by two ADCs. The bandwidth of the ADCs is increased by the insertion of a fast track-and-hold circuit (T&H) before the ADC input. Both elements are controlled by the binary divider in order to exploit subsampling, as shown in Figure 2-5 (taken from [21]). Since the equivalent sampling rate is equal to the clock rate f_c, the Nyquist sampling theorem is met by the receiver. The ADCs outputs provide the digitized MUT response to the FPGA stage.

The FPGA processing task can be summarized in two parts. First, the captured data are synchronously averaged to improve the signal-to-noise ratio. Second, the wanted impulse response

is achieved and transferred via USB to the computer. Note that the MUT can be defined as a linear time-invariant (LTI) system. Additionally, the impulse response of an LTI system in frequency-domain is its transfer function [52]. Therefore, applying the superposition of the input impulse signal $\delta(t)$ and using an appropriate window function w(t), the system impulse response (2.19) and its matrix transfer function (2.20) can be calculated as follows:

$$\mathbf{s}_M(t) = \begin{bmatrix} v_1(t)\Big|_{\substack{m_2(t)=0 \\ m_1(t)=\delta(t)}} & v_1(t)\Big|_{\substack{m_1(t)=0 \\ m_2(t)=\delta(t)}} \\ v_2(t)\Big|_{\substack{m_2(t)=0 \\ m_1(t)=\delta(t)}} & v_2(t)\Big|_{\substack{m_1(t)=0 \\ m_2(t)=\delta(t)}} \end{bmatrix} \cdot w(t). \tag{2.19}$$

$$\mathbf{S}_M(f) = \mathrm{FT}\{\mathbf{s}_M(t)\}. \tag{2.20}$$

2.5 Validation procedure

The following procedure was developed in order to validate the proposed methods and the performance of the M-sequence device.

The procedure consisted of measuring a material of known permittivity, in this case a sample of polytetrafluoroethylene (PTFE), using both a vector network analyzer (VNA) and an M-sequence device. The results were compared with data reported in the literature. In both cases, identical TRL-calibration standards (PTFE) were used. The frequency range was 0.3-3 GHz.

The permittivity of the PTFE-sample was calculated using the proposed methods 1 (2.13) and 2 (2.14). The results of the PTFE measurements in the frequency domain, performed with the VNA and the M-sequence device, are shown in Figure 2-7. Here, the method 1 is labeled as $\varepsilon_r(\Gamma)$, and the method 2 as $\varepsilon_r(T)$. We can see that the measurements performed using the VNA and the M-sequence device coincide with the expected values. Additionally, despite the measurement fluctuations, both devices provided close results to those reported in Fig. 27 and Fig. 28 of [41].

Regarding the performance of the calculating methods, the best result is provided by method 1. The permittivity results for the M-sequence device measurements well agree with PTFE theoretical values. Method 2 provides good results for the real component of the permittivity. However, this method fails calculating the imaginary part of the permittivity.

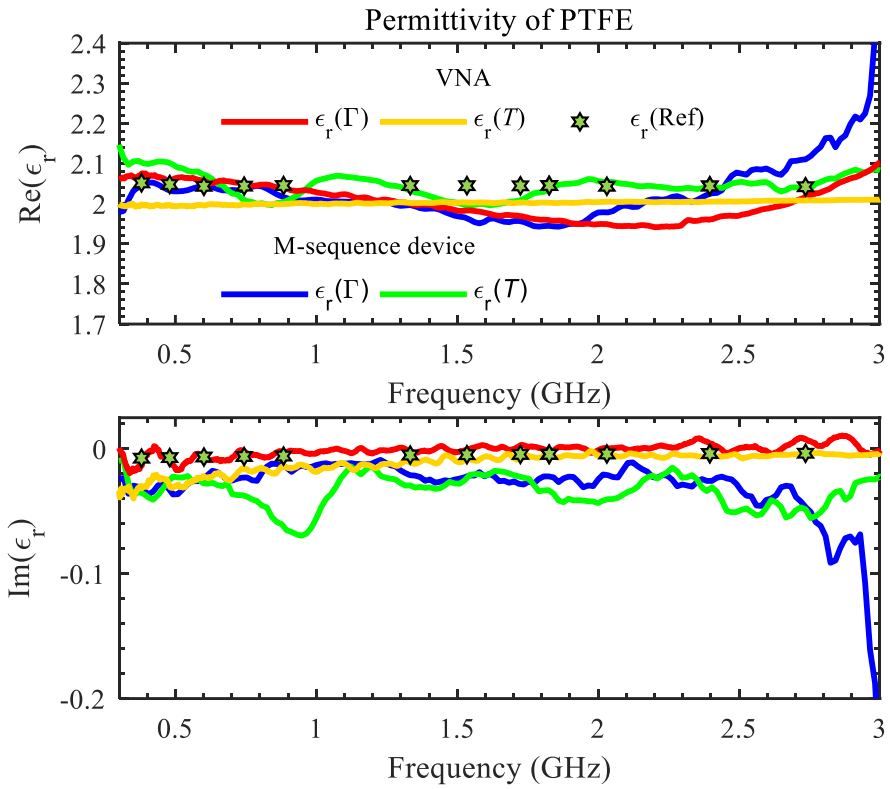

Figure 2-7: Complex permittivity of PTFE-sample calculated from VNA and M-sequence device measurements. $\varepsilon_r(\Gamma)$ is for the permittivity results of method 1. $\varepsilon_r(T)$ is for the permittivity results of method 2.

In general, the calculations of the relative complex permittivity using the proposed methods are in good agreement with the expected values of simulations, presented in [37], and the PTFE-sample measurements. Measurements in time domain provided satisfactory results like those produced by the VNA.

Results obtained applying method 1 to the M-sequence device signals agree with the expected values. Moreover, the method 1 has the particularity that MUT length (L) is not required in the calculations. In contrast, L has to be well known in the method 2, where a variation on the L-parameter affects directly (2.14). Therefore, we prefer using method 1 for field measurements with the M-sequence device.

2.6 Permittivity measurements of ANFO

ANFO is an explosive mixture composed of Ammonium Nitrate (AN) and fuel oil. Artisanal manufactured ANFO constitutes the main charge in most of the IED installed in Colombia [4], [38].

AN is an inorganic salt (NH_4NO_3), not explosive by itself. It acts as the oxidizing agent in the mixture. On the other hand, fuel oil acts as chemical reactive to produce rapid decomposition of the AN within the shock velocities [56]. Sometimes other petroleum derivatives, emulsions, and slurries such as lacquer, mineral oil or aluminum powder are added to the artisanal ANFO in order to increase the initiation sensitivity and blasting power of the charge.

Illegal groups in Colombia have used artisanal ANFO as main charge of the IED. As it is not a standardized manufacturing process, the exact proportion of the materials in the mixture and the mixture content itself can vary.

In order to gain a broad understanding of the dielectric properties of this material, measurements were performed on five types of ANFO and a sample of fertilizer, as shown in Table 2-1 and Figure 2-8.

Table 2-1: Measured MUT samples.

Code	**Name of material**
M1	Commercial ANFO (Manufactured by Indumil Colombia). This explosive is used in mining application.
M2	Artisanal ANFO. Manufactured by illegal groups. This material was provided for the test by the Colombian army from material seized from illegal groups.
M3	Improvised ANFO. This sample was manufactured ex profeso for this experiment with the assistance of experts in explosives from the Colombian Army.
M4	Improvised ANFO + Lacquer. The same manufacturing process as M3. At the end of the process, the lacquer was added. This is made by the illegal groups to increase the velocity of detonation of the explosive.
M5	Improvised ANFO + Paint. The same manufacturing process as M3. At the end of the process, the paint was added. This is made by the illegal groups to change the blasting power of ANFO.
F	Fertilizer-sample. Material usually used by illegal groups to extract the AN.

Figure 2-8: ANFO-explosives samples.

Preparation, management, and manipulation of the explosives were performed by certified experts from the Colombian Army. Several safety procedures were used to handle ANFO properly and prevent any accidental initiation of the explosive. For this reason, during measurements, the maximum power of the m:explore M-sequence device was set to a maximum value of -8 dBm.

In order to reduce the risk, the operator was protected behind a metal barrier five meters away from the test setup and the m:explore was controlled via USB connection.

The measurement procedure consisted of the following steps: First, safety procedures were checked and implemented by all personnel involved in the measurement. Second, coaxial probes and connectors were cleaned using isopropanol. Third, in order to avoid air-gaps in the sample, the material under test was compressed into the probes using a coaxial hand press tool. Six different coaxial probes of the same dimensions were prepared, one for each sample. Fourth, calibration was performed using the procedure explained in section 2.3. Fifth, each probe with the MUT was measured using the setup shown in Figure 2-6. Finally, the permittivity of the MUT was calculated using an automatic script.

Figure 2-9 shows the Nyquist plot of the measured permittivity of the six samples. Figure 2-10 shows the frequency measurements. Both graphics include permittivity values of ANFO reported in [49], this is labeled as ANFO(ref).

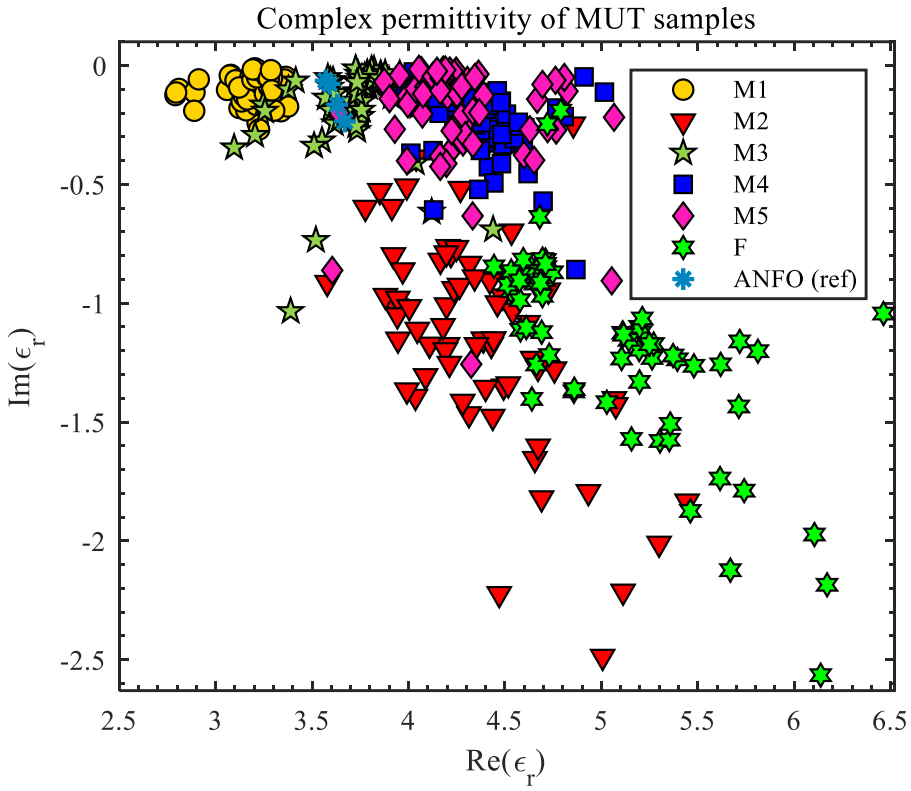

Figure 2-9: Nyquist plot of complex permittivity of measured materials. See Table 2-1 for reference. ANFO(ref) is an improvised explosive reported in [49].

We can differentiate each type of ANFO in the Nyquist plot and these can be grouped by their origin (e.g. commercial, artisanal, or improvised) or by their fabrication process. For example, the commercial ANFO (M1) is in the upper left side of the plot, where its complex permittivity values are concentrated from 3 to 3.4 in the real part, and from -0.27 to - 0.01 in the imaginary part. Then, the improvised ANFOs (M3, M4, M5) are grouped in the same range of the imaginary part where M1 is located, but with a shift to the right. The real part of the improvised ANFOs are defined as follows: M3 vary from 3.5 to 3.9, M4 from 3.9 to 4.3, and M5 from 4.2 to 5. Notice that the permittivity of the improvised ANFO reported in [49] (ANFO(ref)) is similar to M3. Finally, the permittivity values of the artisanal ANFO (M2) are located between 3.6 and 5, which is the same range where improvised ANFO is located. However, M2 is differentiated from M3, M4, and M5, by its lower imaginary part that covers values from -2.4 to - 0.5.

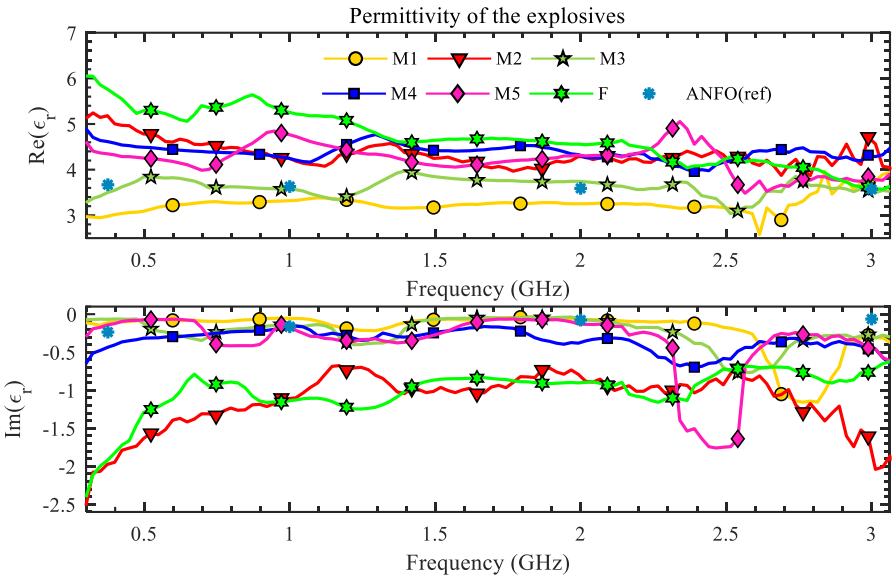

Figure 2-10: Complex permittivity of explosives and fertilizer. Labels are according to Table 2-1. ANFO(ref) is an improvised explosive reported in [49].

Figure 2-10 shows that real part of the permittivity has a flat response in the frequency domain, for all the types of ANFO studied here. Regarding the imaginary part of MUT-permittivity, the behavior is continuous for all measured materials, despite the discontinuity near to 2.5 GHz (resonant effects) for the samples M1, M3, M4, and M5. Additionally, a similarity in the imaginary part can be seen between the artisanal ANFO (M2) and the fertilizer-sample (F).

2.7 Conclusion

The permittivity of improvised ANFO was successfully measured in frequency domain, using the proposed methodology. The obtained results can now be included in electromagnetic simulations or theoretical calculation and applied in the manufacturing of inert surrogates of IEDs, which will be used as test objects in GPR measurements.

The results indicate that the different preparation can be clearly discriminated and identified using the value of the permittivity. This can be used, for example, to fingerprint specific preparations of improvised explosives, identifying its source.

3. GPR measurements[2]

In this chapter, the concept of a polarimetric GPR system is presented and the data processing of the polarimetric GPR signals is explained. A combination of recursive algorithms and background removal techniques are proposed as clutter removal strategy. Additionally, a change in the antenna incidence angle is proposed to decrease the ground reflections. Finally, the acquisition system and the data processing stage are validated using laboratory and field GPR measurements of IEDs and Non-IEDs targets.

The results show that the tilted antenna configuration combined with the proposed data processing structure is useful as a clutter removal strategy. This increases the chance to discriminate the IEDs from the Non-IEDs targets. The proposed technique permits to identify buried objects as a discontinuity in the B-scans. These results are used as input in chapter 4.

Part of the information and results presented in this chapter were previously published in [57] by the author of this thesis. The paper was entitled "Application of Polarimetric Features and Support Vector Machines for Classification of Improvised Explosive Devices".

3.1 Introduction

GPR is a well-established approach for the contactless detection and imaging of buried objects in the fields of archeology, glaciology, or geophysics [22]. Moreover, it is a promising and reliable technique for the detection of unexploded ordnance (UXO) or landmines [16], [58], [59]. Data processing techniques of co-polarized GPR measurements have been used to remove unwanted

[2] Part of the results shown in this chapter was published in S. Gutierrez, F. Vega, F. A. Gonzalez, C. Baer, and J. Sachs, 'Application of Polarimetric Features and Support Vector Machines for Classification of Improvised Explosive Devices', IEEE Antennas and Wireless Propagation Letters, pp. 1–4, 2019. DOI: 10.1109/LAWP.2019.2934691.

reflections such as surface ground reflections, antenna effects, reflections from the soil, among others [16], [60]. Furthermore, advanced data processing techniques have been proposed as promising procedures to increase the signal to clutter ratio and detect buried targets [24]–[26], [61], [62].

In this research, we use polarimetric GPR measurements in order to reduce the soil-clutter reflection improving the chances of discriminating between IEDs and clutter objects. Additionally, recursive least square and linear predictive coding algorithms, are used for data processing and clutter removal of the time-domain signal.

This chapter is organized as follows. The polarimetric GPR-measurement setup is described in section 3.2. Data processing is presented in section 3.3. Experimental data collection is explained in section 3.4. The polarimetric GPR measurement results are reported in section 3.5. The experimental data collection is carried out in two test groups. In the first group, the measurements are performed in the frequency domain, whereas in the second one, the measurements are accomplished in the time- domain.

3.2 GPR-measurement setup

The GPR system is composed of three main parts: antenna, acquisition system, and positioning system, as summarized in Figure 3-1. It can record GPR images in X and Y direction and its frequency range is from 0.8 GHz to 5 GHz. Two different GPR systems were used. The first one uses a VNA, works in frequency-domain and it is designed to perform measurements in laboratory (indoor) scenarios, whereas the second one uses an M-sequence device, it operates in time-domain and is used for GPR measurements in field (outdoor) scenarios. In the following subsections, we describe each part of the system and the measurement scenarios.

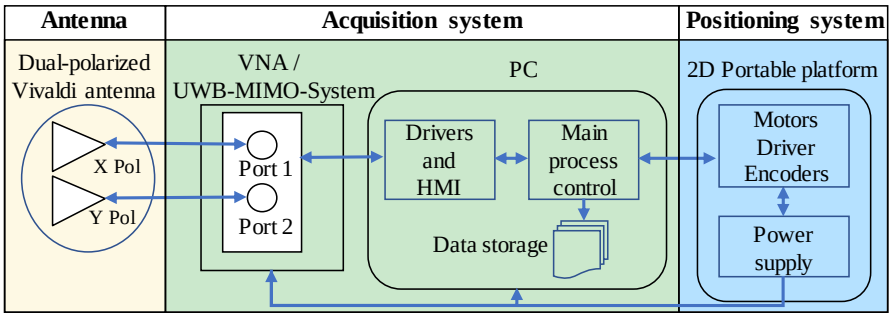

Figure 3-1: Block diagram of the GPR system.

3.2.1 Antenna

The antenna was designed in the framework of the MEDICI project by the Institute of Electronic Circuits at Ruhr University Bochum, Germany. In addition to the requested frequency range, the main design parameters for the GPR antenna were: A polarimetric setup for recording trans-polarizing effects; low antenna ringing in order to distinguish between multiple antenna reflections and low reflective targets in close antenna proximity; sidelobe suppression for avoiding cross-talk in multi-static radar setups; and reasonable gain for increasing the signal-to-noise ratio.

The developed antenna is a dual-polarized Vivaldi antenna, as shown in Figure 3-2. This antenna satisfies the requested GPR frequency range, has a maximum gain of 9 dBi, a cross talk suppression better than 30 dB and a ringing suppression of more than 40 dB in 15 cm distance. Additional information on the designed antenna can be found in [63].

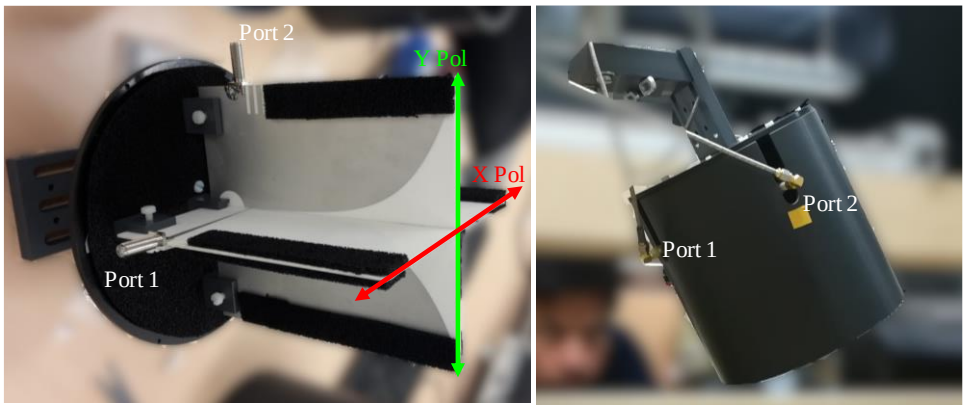

(a) (b)

Figure 3-2: Dual-polarized Vivaldi antenna: (a) internal view and (b) complete antenna with housing.

3.2.2 Acquisition system

Two acquisition system were tested. The first one is a frequency domain system, used during a set of laboratory tests. It consisted of a Rohde&Schwarz ZNB 8 VNA, operating as wideband stepped frequency (SFCW) radar. This device has two channels, and its frequency range was set from 800 MHz to 5 GHz with 1 kHz in the IF bandwidth and 2009 frequency points.

The second acquisition system consisted on a time-domain ultra-wideband MIMO system, called m:explore®, manufactured by Ilmsens. This was used during a set of outdoor tests. This UWB-MIMO-System is composed of four ultra-wideband M-sequence radar-units, which are internally

synchronized. Each unit has one transmitting channel and two receiving channels, as shown in Figure 3-3. In total, two of those units were used in the outdoor test. The working principle of the M-sequence is based on a pseudo-noise signal, herein an M-sequence of order 9. Further information regarding the working principle of the M-sequence system can be found in section 2.4 and in [21]. The main control and the processing unit are carried out by a laptop linked via USB/Ethernet with the UWB radar. This device has a battery-backup option, which makes it useful for field measurements under an operational ambient temperature from 0°C to 40°C. The resulting stored data are the impulse response of each radar channel, i.e. GPR-measurements in time-domain.

Figure 3-3: Front-panel of the UWB-MIMO-System, SH-3140 model. This system is composed of four ultra-wideband M-sequence units, labeled as T1R2, which are internally synchronized by the CLK unit. Each T1R2 unit has one transmitting channel and two receiving channels. The power supply of the system is provided by a UPS module.

3.2.3 Positioning system

GPR measurements were performed using a 2D portable platform, controlled by a positioning system. The system is suitable to configure the GPR in the common offset survey mode, i.e. with a fixed separation between the transmitter (Tx) and receiver antennas (Rx) [16]. In this mode, the transmission and the reception antenna scan the ground surface, as shown in Figure 3-4.

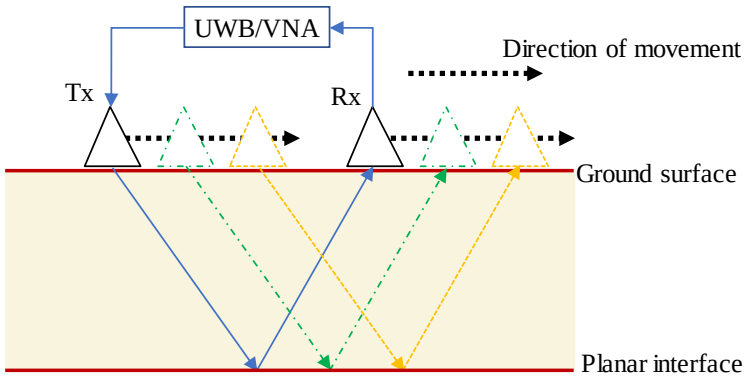

Figure 3-4: Geophysical common offset survey mode.

In the case of the indoor test, the platform was placed over a sandbox of dimensions 2.5m x 1.2m x 1.2m filled with coarse sandy soil, as shown in Figure 3-5. During the outdoor test, the scanning area was a rectangle of dimensions 1.5m x 2.5m and the soil was a typical Andean soil from Colombia, as shown in Figure 3-6.

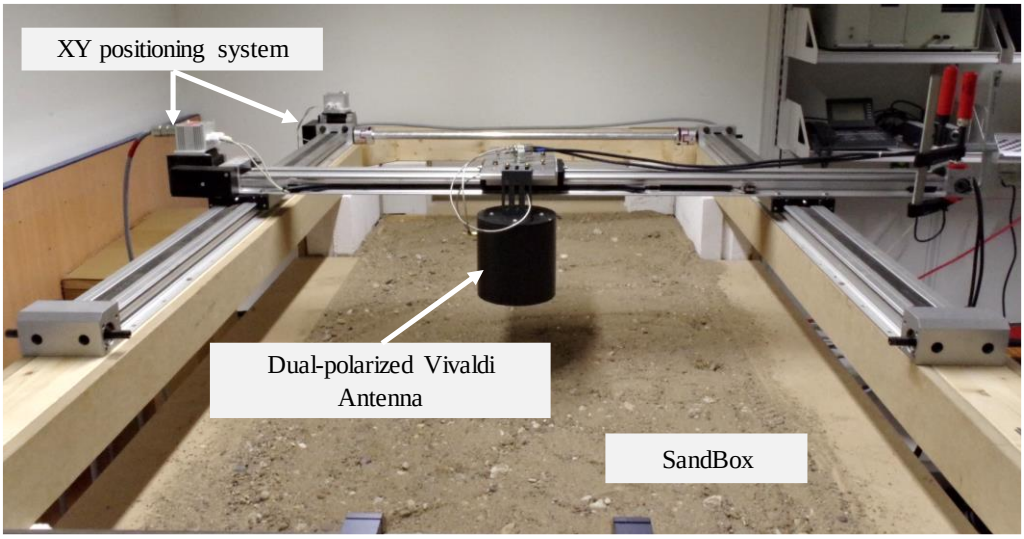

Figure 3-5: Indoor test scenario, sandbox measurement setup.

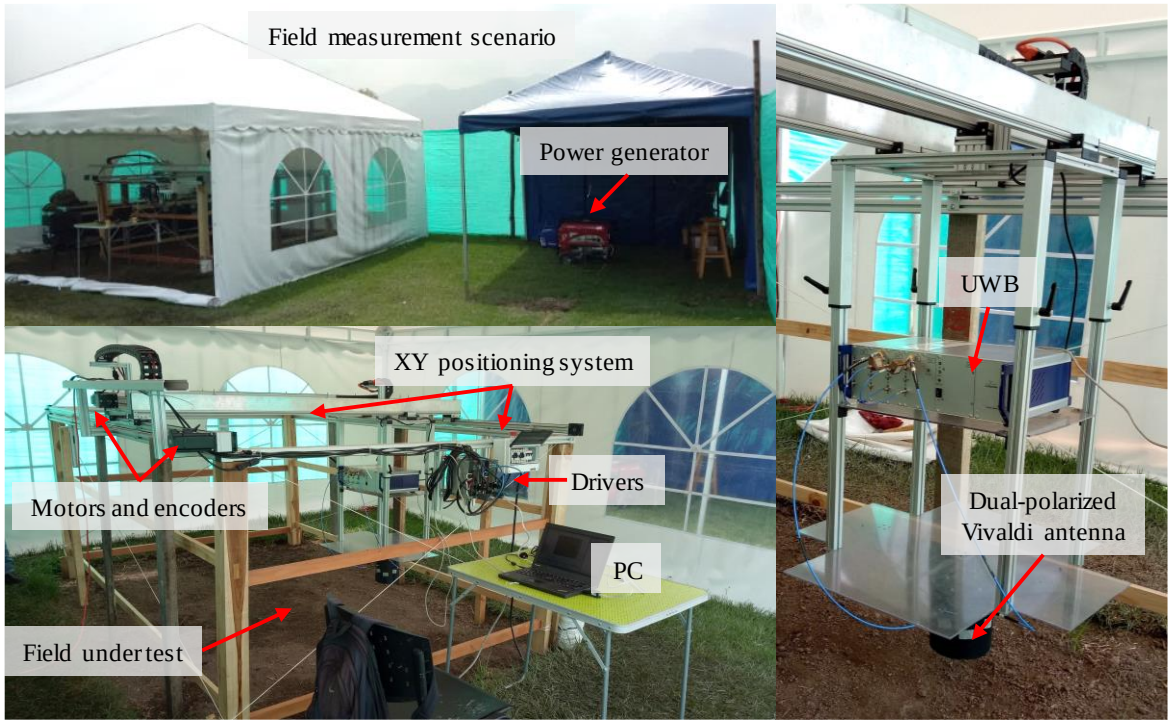

Figure 3-6: Outdoor measurement setup.

3.2.4 Polarimetric data acquisition

Polarimetric measurements were achieved connecting dual-polarized Vivaldi antennas in a two-port configuration and measuring all the possible ports combination with the described acquisition systems. The polarimetric data acquisition for the two GPR systems will be described for both scenarios as follows.

A. Polarimetric data acquisition in indoor tests

In the test performed in the laboratory, the Vivaldi antenna in X polarization was connected to port- 1 of the VNA, while the antenna with Y polarization was connected to the VNA port-2, as shown in Figure 3-7. The polarimetric data measured with the VNA can be expressed as

$$\mathbf{A}(n,\omega)=\begin{pmatrix}\mathbf{A}_{xx}(n,\omega) & \mathbf{A}_{xy}(n,\omega)\\ \mathbf{A}_{yx}(n,\omega) & \mathbf{A}_{yy}(n,\omega)\end{pmatrix}=\begin{pmatrix}\mathbf{S}_{11}(n,\omega) & \mathbf{S}_{12}(n,\omega)\\ \mathbf{S}_{21}(n,\omega) & \mathbf{S}_{22}(n,\omega)\end{pmatrix}, \tag{3.1}$$

where $\mathbf{A}(n,\omega)$ is a matrix with the full-polarimetric data in frequency-domain, n is the antenna position where the measurement is performed, and the $\mathbf{S}$ elements are scattering parameters measured with the VNA. In order to get the polarimetric data in time-domain, the IFFT was applied.

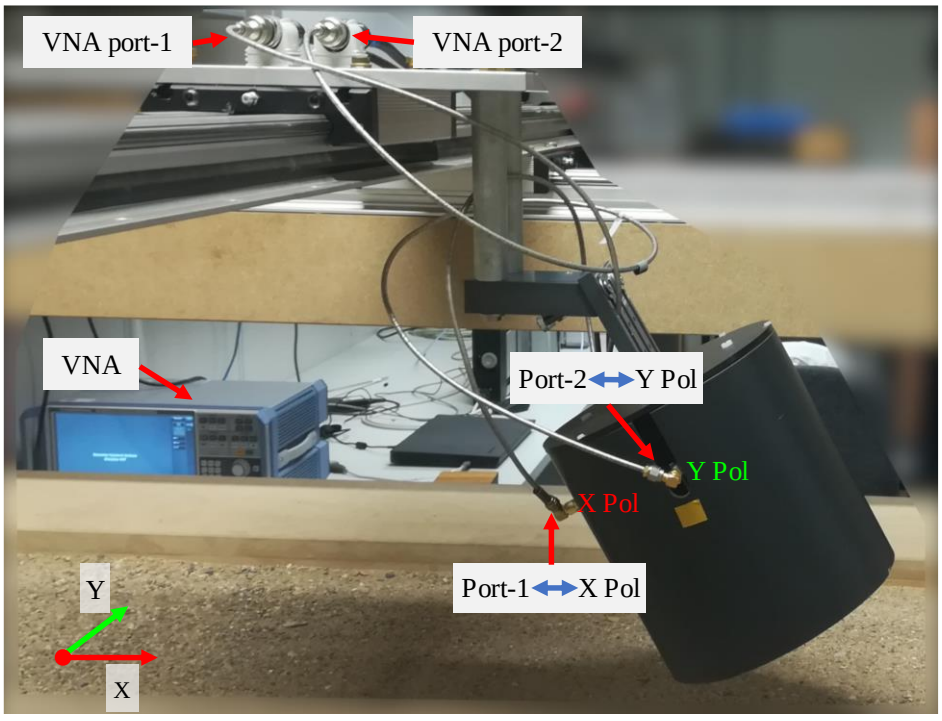

Figure 3-7: Polarimetric data acquisition setup in the laboratory test scenario. The dual-polarized Vivaldi antenna is connected to the two-port VNA. Blue lines indicate the signal direction between the ports of the VNA and the antennas.

B. Polarimetric data acquisition in the outdoor scenario

In the field measurement scenario, two UWB units and two dual-polarized Vivaldi antennas are configured as a two-input/output system, as shown in Figure 3-8. Therefore, the full polarimetric data are expressed in time-domain as:

$$\mathbf{a}(n,t) = \begin{pmatrix} \mathbf{a}_{xx}(n,t) & \mathbf{a}_{xy}(n,t) \\ \mathbf{a}_{yx}(n,t) & \mathbf{a}_{yy}(n,t) \end{pmatrix} = \begin{pmatrix} \mathbf{y}_{31}(n,t) & \mathbf{y}_{32}(n,t) \\ \mathbf{y}_{41}(n,t) & \mathbf{y}_{42}(n,t) \end{pmatrix}, \tag{3.2}$$

where $\mathbf{a}(n,t)$ is the full polarimetric A-scan measured at the antenna position n. The term $\mathbf{y}(n,t)$ is the impulse response for each input/output port configuration.

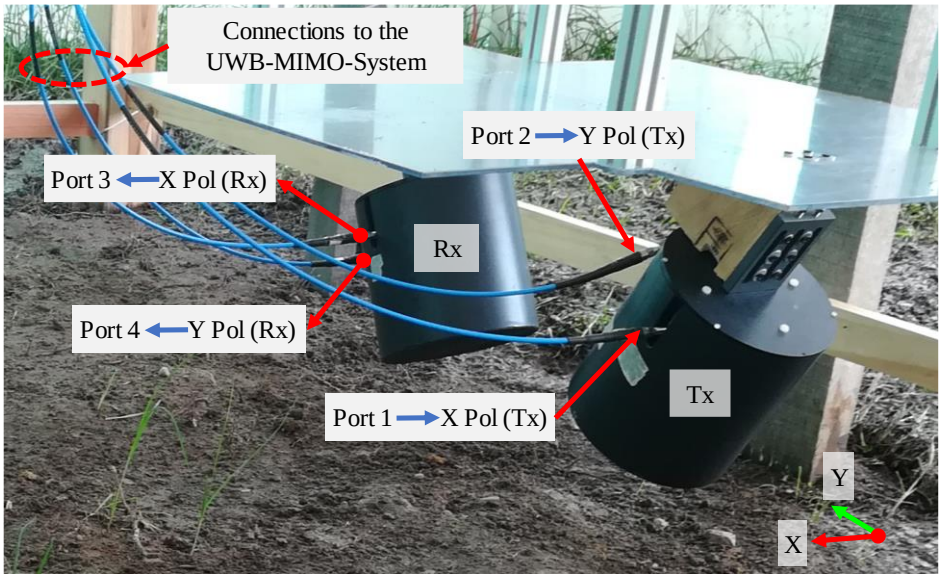

Figure 3-8: Polarimetric data acquisition setup in the field test scenario. Two dual-polarized Vivaldi antennas are connected to the UWB-MIMO-System in a two-input/output configuration. The signal direction between the UWB ports and the antennas are indicated with blue lines.

3.3 Data processing

GPR measurements produce a radargram or B-scan, which is a collection of impulse responses or A-scans measured while the GPR is moving along a straight track line over the soil. In other words, the radargram is a representation of cumulative time-domain signals measured at different *n*-positions of the antenna. Moreover, GPR measurements can be considered as the Impulse Response (IR) $h(t)$ of a Linear Time-Invariant (LTI) system, where the input signal of the LTI system is defined as $x(t)$ and the LTI output signal as $y(t)$, which can be written as follows [52]:

$$\begin{aligned} y(t) &= x(t) \otimes h(t) \xleftrightarrow[IFT]{FT} Y(j\omega) = X(j\omega)H(j\omega), \\ y(t) &= \delta(t) \otimes h(t) \xleftrightarrow[IFT]{FT} Y(j\omega) = H(j\omega), \\ y(t) &= h(t) \xleftrightarrow[IFT]{FT} Y(j\omega) = H(j\omega), \end{aligned} \tag{3.3}$$

where $\otimes$ is the convolution operator; $X(j\omega)$ and $Y(j\omega)$ are the Fourier Transform (FT) of the input $x(t)$ and the output $y(t)$, respectively; and $H(j\omega)$ is the frequency response function or the FT of $h(t)$.

Therefore, if an LTI system is excited by a Dirac impulse $\delta(t)$, the output becomes equal to the impulse response $h(t)$ ($H(j\omega)$ in frequency-domain) as shown in Figure 3-9.

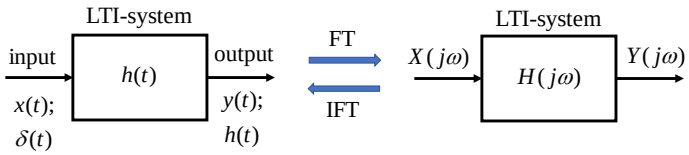

Figure 3-9: LTI-system representation.

In this context, the GPR measurements are the relationship of the input-output discretized signals of the LTI system defined by the antennas, air, soil, and buried targets. The basic system model, shown in Figure 3-10, can be expressed as:

$$a(k) = y(k) = x(k) \otimes h(k) = x(k) \otimes \left(h_c(k) + h_t(k)\right), \tag{3.4}$$

where k is the discretized propagation time, $a(k)$ is the discretization of an A-scan measurement and it is equal to the LTI output signal $y(k)$. The term $h(k)$ is the system IR composed of the clutter IR $h_c(k)$ and target IR $h_t(k)$. The clutter is considered as unwanted returns from sources different than the targets of interest [22], such as antenna crosstalk, surface ground reflections, antenna effects, reflections from the soil, and backscattering from non-targets [16], [21], [27].

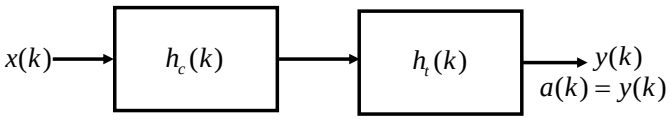

Figure 3-10: GPR signal model, system impulse response.

In general, the processing is focused on removing as much clutter as possible without losing information from the target. This means to remove $h_c(k)$ or at least decrease its effects in the

measured signal $a(k)$. Among clutter removal, the most common techniques are subtraction of the mean of all scans and moving average along a sliding window [16], [21], [62]. Other techniques remove the clutter effects based on modeling the soil and clutter. These models are made by using wavelet packet decomposition, autoregressive moving average models, system identification, and deconvolution [16], [24]–[27], [29], [64]. Moreover, techniques such as recursive algorithms and filtering structures are also proposed to reduce the clutter effects [24], [27].

In this research, we combine background subtraction and adaptive filters in order to remove the clutter in polarimetric measurements, as shown in Figure 3-11. This will be introduced in the following subsections.

Figure 3-11 shows the block diagram of the data processing. The two main stages are the GPR measurements, described in the current chapter, and the polarimetric extraction of polarimetric data, which will be explained in chapter 4.

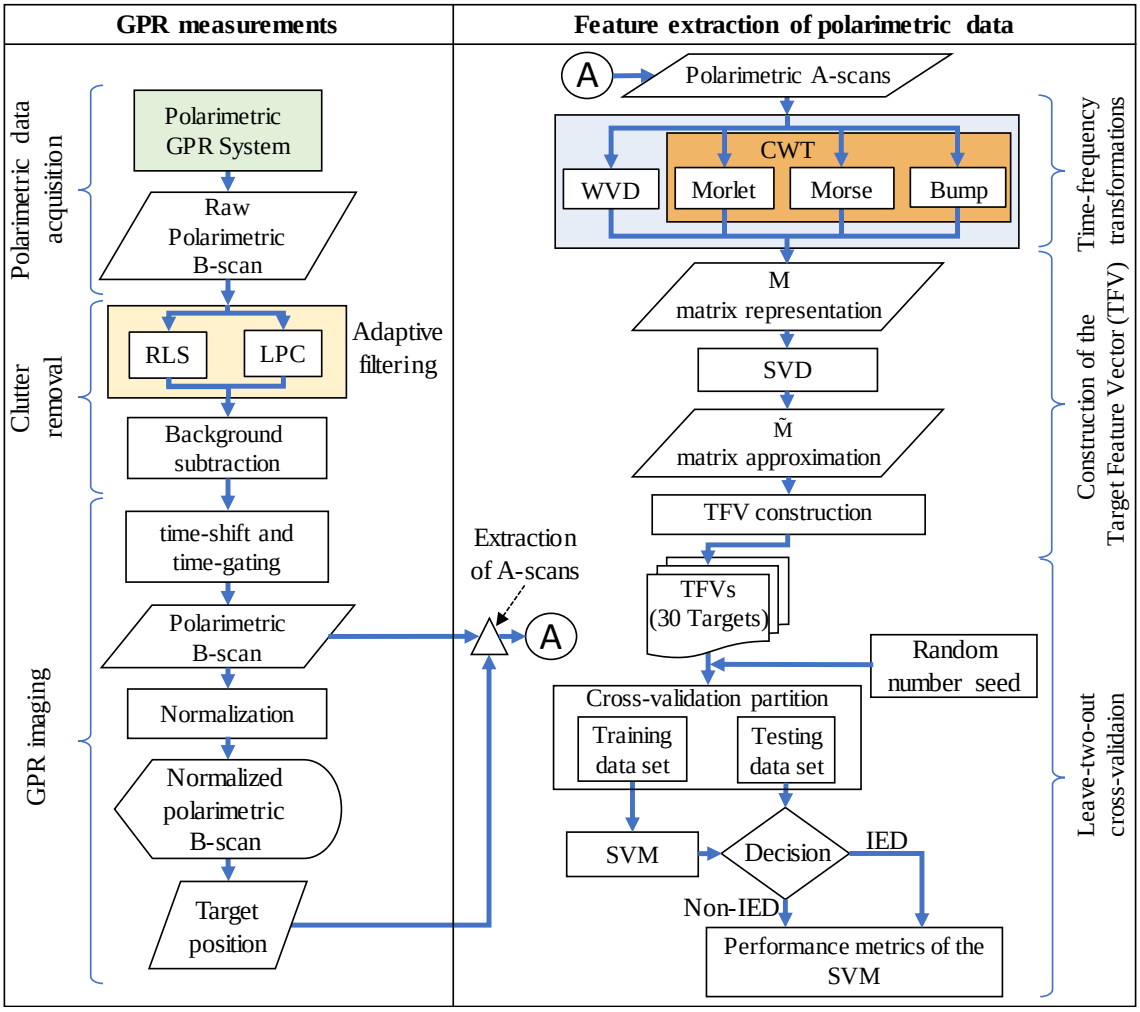

Figure 3-11: Data processing block diagram. Two stages are presented: the GPR measurements stage and the feature extraction of polarimetric data. Eight data processing alternatives are possible by the combination between the two adaptive filters with the four time-frequency transformations.

3.3.1 Background subtraction

Part of the clutter signals has stationary behavior, i.e. unwanted reflections from the environment that appear at the same time in the A-scans and produce horizontal lines in the B-scan. These stationary effects, recognized as background, were determined by a sliding horizontal averaging in the B-scan. Afterward, this background was subtracted from the B-scan, as follows:

$$\begin{aligned} \overline{b}_{k,n}(k) &= a_n(k) - \overline{g}_n(k), \\ \overline{g}_n(k) &= \frac{1}{s_w} \sum_{j=n-\frac{s_w-1}{2}}^{n+\frac{s_w-1}{2}} a_j(k); \; n = 1, 2, \ldots, N, \end{aligned} \tag{3.5}$$

where $\bar{b}_{k,n}(k)$ is the B-scan with background subtraction, $a_n(k)$ is the n^{th} A-scan, N is the total number of antenna positions, k is the discretized propagation time and $\bar{g}_n(k)$ is the centered moving average estimated using a sliding window of size s_w that is moved along n direction, which allows the removal of the stationary effects present in neighboring A-scans measurements.

3.3.2 Adaptive filters for clutter reduction

The basic adaptive filter structure is depicted as a block diagram in Figure 3-12. A characteristic of an adaptive filter is that their coefficients are updated recursively, which makes it useful for online processing.

Moreover, the adaptive filter aims to extract information from the filter input signal $x(k)$ in order to match the desired signal $d(k)$. For this purpose, the adaptive algorithm generates the filter coefficients to minimize the error between the desired signal and the filter output, $e(k) = d(k) - y(k)$ [65]. Consequently, the filter parameters are updated from one iteration to the next [66].

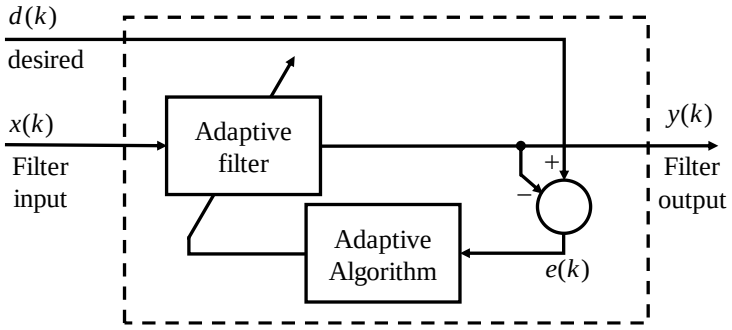

Figure 3-12: Adaptive filter.

Typical filter structures are noise cancellation, inverse modeling, linear prediction, and feed-forward control. These structures define how the filter output signal is computed from its input signal. Further details can be found in [52], [65]–[67].

In this research, adaptive filters were used as a system identification method. In special, the Recursive-Least-Squares (RLS) method and the Linear-Predictive-Coding (LPC) method were used to estimate the clutter model $h_c(k)$ in Equation (3.4). However, RLS requires prior information of

the clutter to perform estimation, e.g. target-free soil measurements. In contrast, LPC works without prior clutter information.

Clutter removal method using the RLS is shown in Figure 3-13, where the desired signal $d(k)$ is the prior clutter information. The filter input signal $x(k)$ is the measured A-scans under analysis $a_n(k)$ and $y_n(k)$ is the best clutter estimation extracted from each A-scan. The output is the measured A-scans with clutter removed $a_n(k) - y_n(k)$.

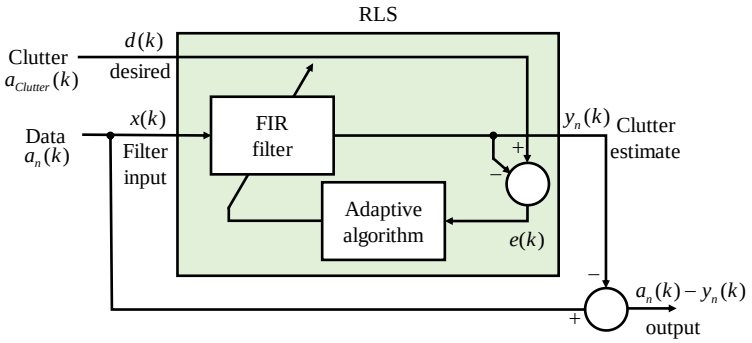

Figure 3-13: RLS method for clutter removal.

Regarding the LPC method, it estimates the coefficients $\{c_i\}$ of a forward linear predictive model of p^{th} order. Then, these coefficients are used to implement a filter which has a discrete transfer function $H_{\text{filter}}(z)$ defined as:

$$H_{\text{filter}}(z) = \frac{1}{1 - \sum_{i=1}^{p} c_i z^{-i}}. \tag{3.6}$$

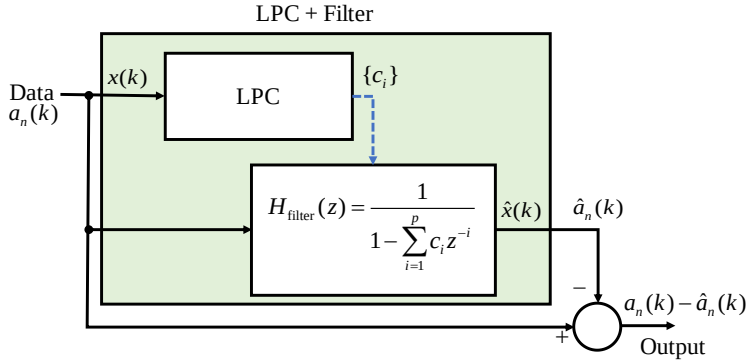

Figure 3-14: LPC method for clutter removal.

Therefore, the signal $\hat{x}(k)$ is a filtered estimate of the input data, as shown in Figure 3-14. The filtered process is performed for each A-scan $a_n(k)$, and the output is the residue between the input data and the estimated data $\hat{a}_n(k)$.

3.4 Experimental GPR data collection

The GPR systems described in section 3.2 were used to collect polarimetric data in laboratory and field measurement scenarios. The GPR antennas were set in the common offset mode at 15 cm above the soil surface. Moreover, in order to reduce the soil-clutter reflection, we used the forward-looking configuration in the indoor setup, as depicted in Figure 3-7, while the field setup used the side-look configuration, as depicted in Figure 3-8 and Figure 3-15. Both configurations had antennas with an angle of 30° off-normal incidence.

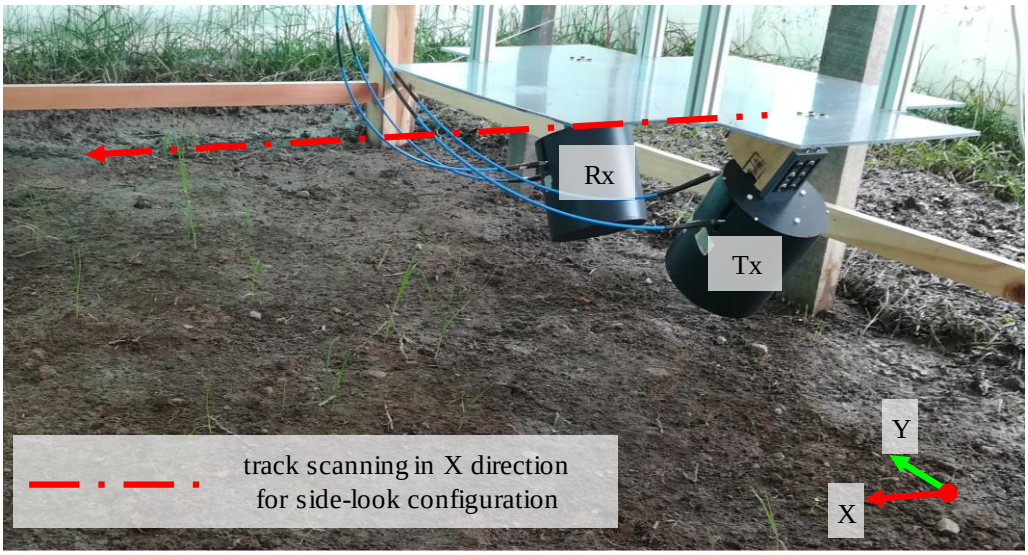

Figure 3-15: Side-look antenna configuration.

Based on the information provided by demining groups, inert IEDs were built with different containers, activation mechanisms, and materials such as those used to build real IEDs, as shown in Appendix A. The improvised inert devices were filled with a developed surrogate material that emulates the ANFO dielectric properties measured in section 2.6. Moreover, the electro-explosive device described in [68] or the detonator inside the surrogated IED was also inert. Additionally, clutter objects that can produce false alarms in demining activities were also used (plastic and glass bottles, razors, pocket knives, canned food, screws, straps, among other objects). Both targets, IED

and Non-IED, had low metal content. In total, thirty targets were buried between 2 cm and 15 cm, measured from the target top to the soil surface. In the laboratory setup, ten IEDs and ten Non-IEDs were used. The remaining five IEDs and five Non-IEDs were buried in the field scenario three months before scanning activities took place.

Afterward, the data acquisition procedure was carried out. The GPR system was moved on a straight track line over the targets, while the polarimetric data were measured every 0.5 cm.

In order to remove clutter reflections and detect the buried targets, the following data processing, depicted in Figure 3-11, was implemented. First, the raw polarimetric data, measured with the GPR system, were used as the input signal for both RLS and LPC adaptive filters, as explained in section 3.3.2. Second, the background removal with a sliding window was applied. Third, time-shift and time-gating were applied in order to localize the soil surface and focus on a region of interest of at least 20 cm depth. Fourth, polarimetric data were normalized between zero and one. Consequently, the normalized polarimetric B-scans were formed by the collection of the processed A-scans. Fifth, targets were detected, which appear as a discontinuity in the B-scans, as described in the following section.

3.5 Experimental results

In this research, a polarimetric B-scan figure is composed of four subfigures, each one related to the polarization scheme presented in 3.2.4. Therefore, two B-scans display the co-polarization measurements and two B-scans the cross-polarization measurements. Moreover, in the figure caption, RLS or LPC is the adaptive filter used in the data processing procedure.

3.5.1 Laboratory measurements results

Figure 3-16 shows the raw polarimetric B-scans data of the laboratory measurement labeled as sandbox174. In this measurement, two targets are scanned, the IED with label 16 and the clutter object with label 26. We can see the soil-reflections as a horizontal line in all polarizations. Moreover, the soil reflections in both cross-polarizations have a lower intensity than the co-polarizations measurements. Additionally, in the two cross-polarizations, some discontinuities under the soil surface are identified, however, no target is detected directly in the raw data.

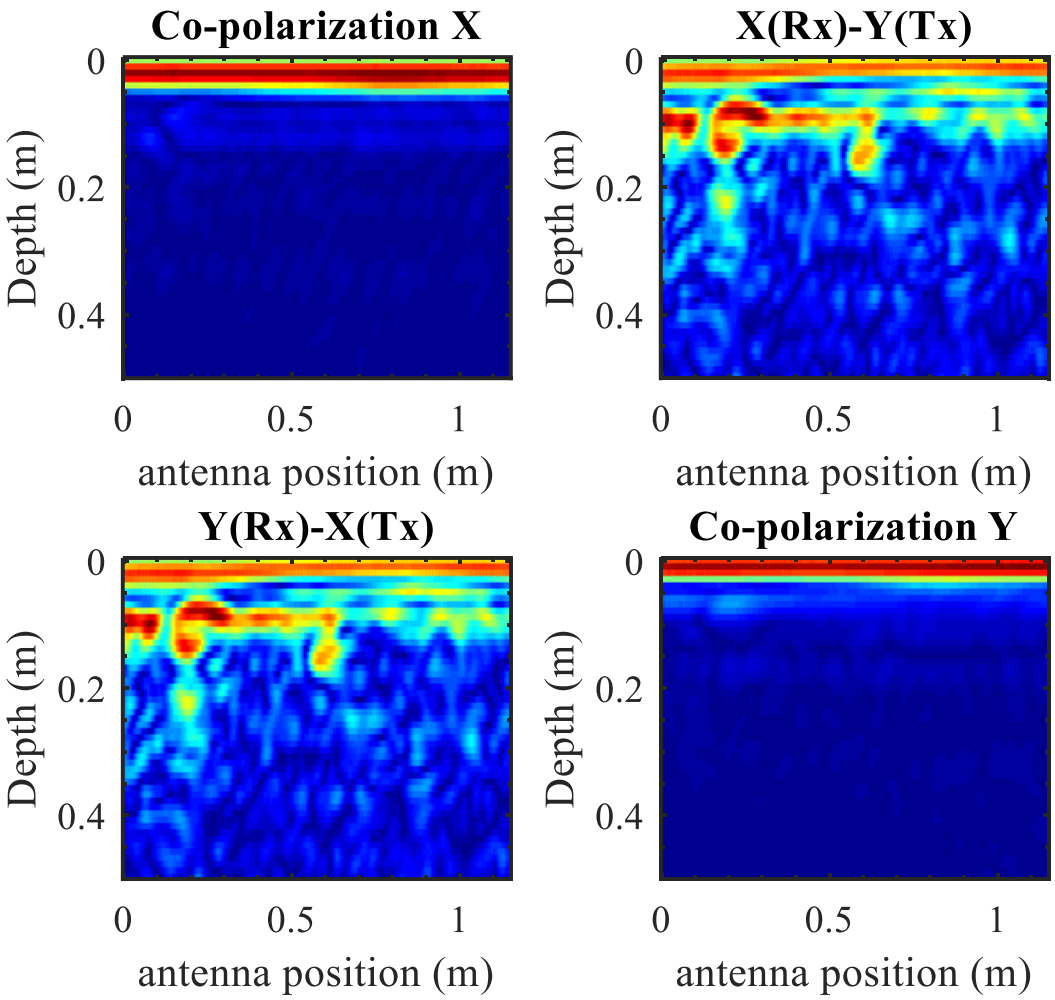

Figure 3-16: Raw data of the laboratory measurement for sandbox174. The polarimetric GPR measurements are depicted as four B-scans. The horizontal red lines are the reflections produced by the soil surface, which can be identified in all polarizations in the raw data.

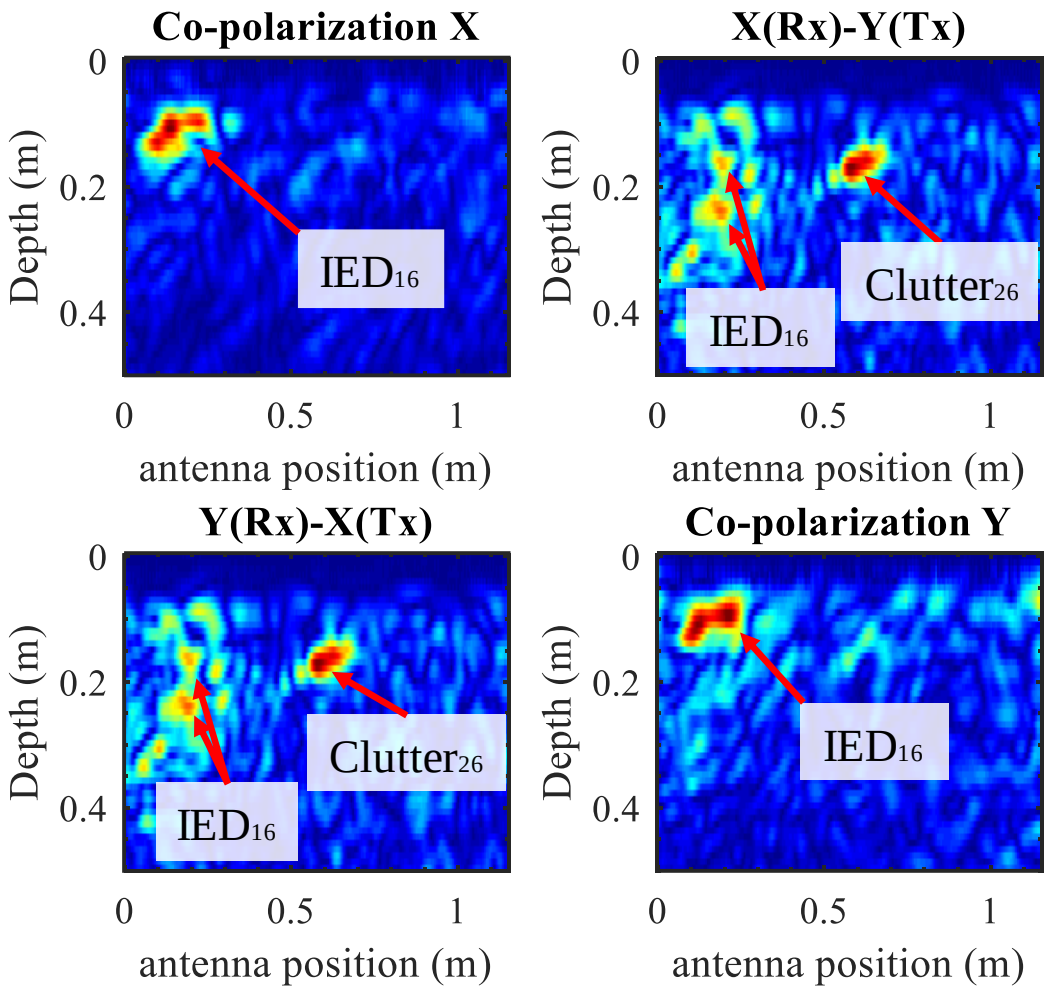

Figure 3-17: Polarimetric B-scan using RLS filter in data processing. Results of laboratory measurement for sandbox174. The soil reflections are successfully removed and no horizontal lines are present in the B-scans. The IED target discontinuity are localized in all polarizations and the Clutter object discontinuity are identified in the cross-polarized measurements.

Figure 3-17 shows the same data, after applying the RLS filter and the data processing procedure described in section 3.4. Similarly, Figure 3-18 shows the polarimetric B-scan when the LPC filter is used in data processing. Both configurations detect the two targets. Moreover, in this measurement, the clutter object is detected only in the cross-polarizations B-scans. In contrast, the IED is detected in all polarizations.

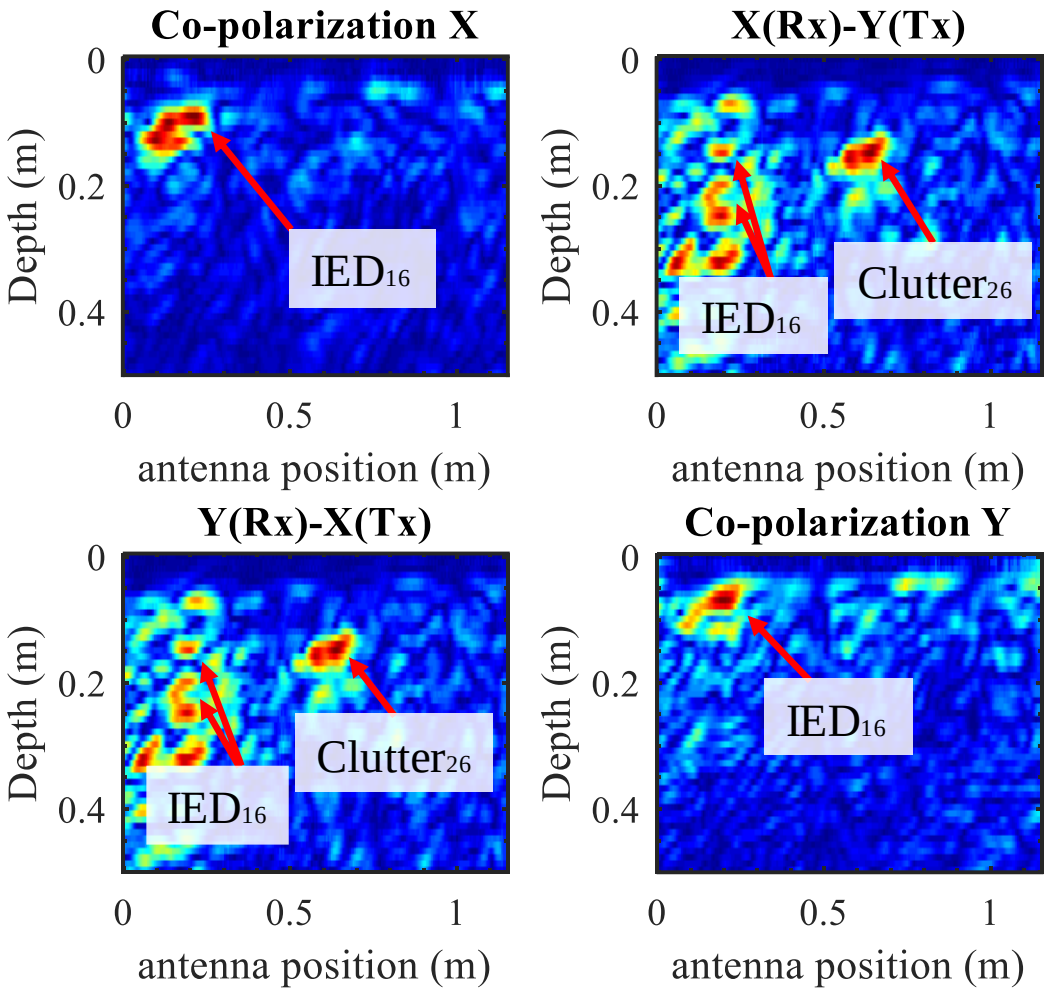

Figure 3-18: Polarimetric B-scan using LPC filter in data processing. Results of laboratory measurement for sandbox174. The soil reflections are removed and the clutter object is detected in the cross-polarized B-scans. In contrast, the IED target is detected in all polarizations, however, clutter reflections around the IED target are present in the cross-polarized B-scans.

In general, RLS and LPC filter configurations have satisfactory results for localizing the targets in the laboratory scenario. Furthermore, in the normalization stage and similarly to the described background subtraction procedure, a sliding window is also applied. This normalization with a sliding window is used to avoid that those targets with high reflectivity hide the discontinuity region of other targets, as shown in Figure 3-19.

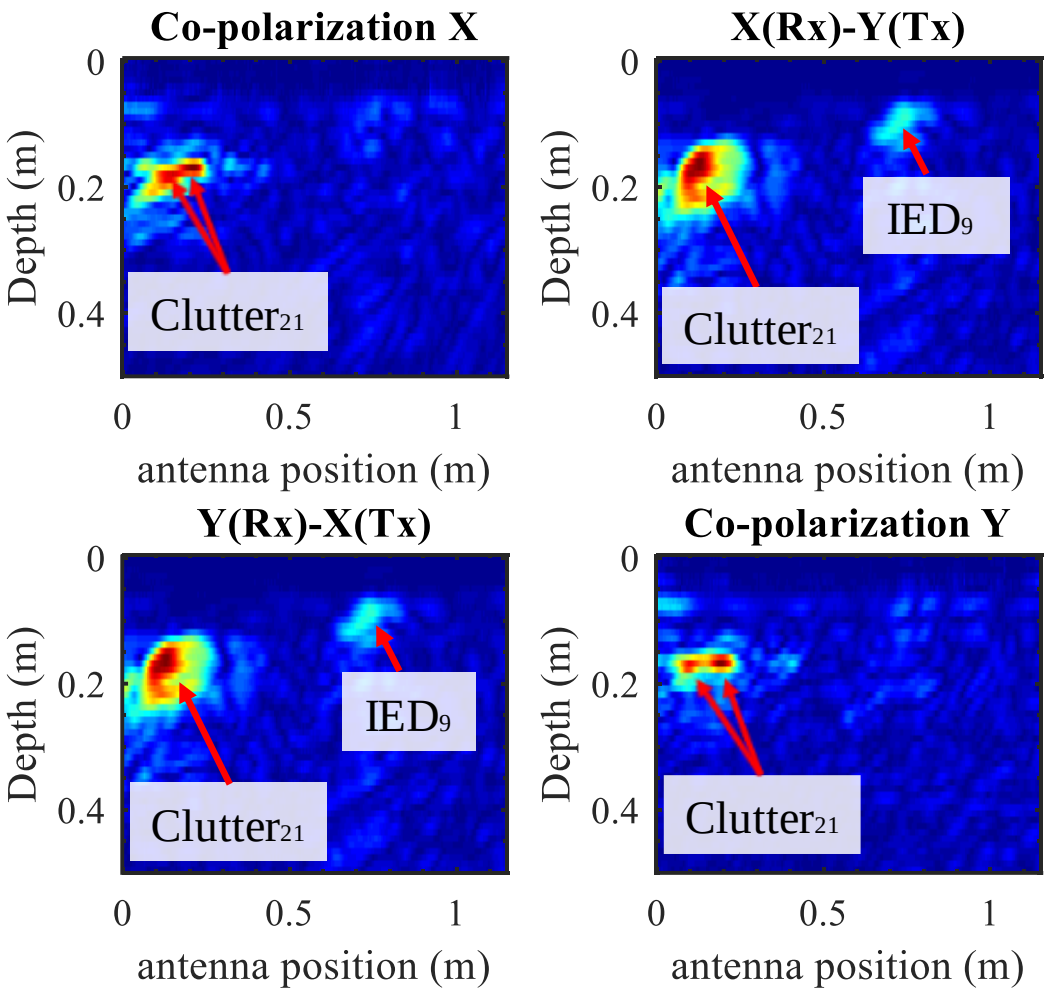

Figure 3-19: Polarimetric B-scan using LPC filter in data processing and applying normalization of data using the whole B-scan. Results of laboratory measurement for sandbox120. In this measurement, the high reflectivity of the clutter object hides the discontinuity of the IED.

Figure 3-19 to Figure 3-21 show the polarimetric B-scan after data processing of the laboratory measurement for sandbox120. This measurement scan one clutter object ($Clutter_{21}$) and one IED (IED_9). In Figure 3-19, we can see the both targets in the cross-polarized B-scans, however, the localization of those two targets are improved after the normalization with sliding window is applied, as shown in Figure 3-20 and Figure 3-21.

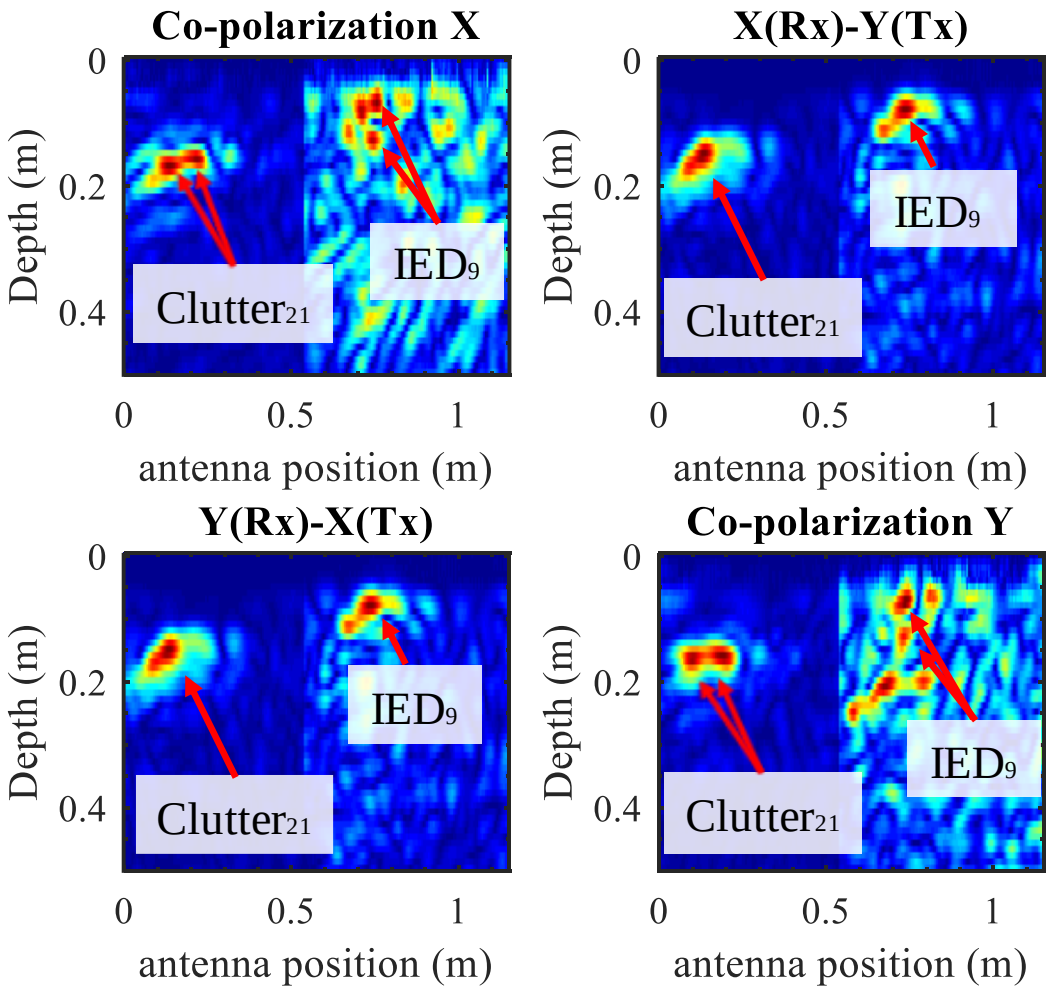

Figure 3-20: Polarimetric B-scan using RLS filter in data processing and applying a sliding windowing normalization of size 0.5 m width. Results of laboratory measurement for sandbox120. Two contrasting rectangular areas are distinguished and its width is equal to the normalization window size.

In Figure 3-20 and Figure 3-21, we can see both targets in all polarizations. Moreover, the two targets can be detected and localized easily in the cross-polarizations. In contrast to Figure 3-17 and Figure 3-18, the clutter object in Figure 3-20 and Figure 3-21 is detected in all polarizations.

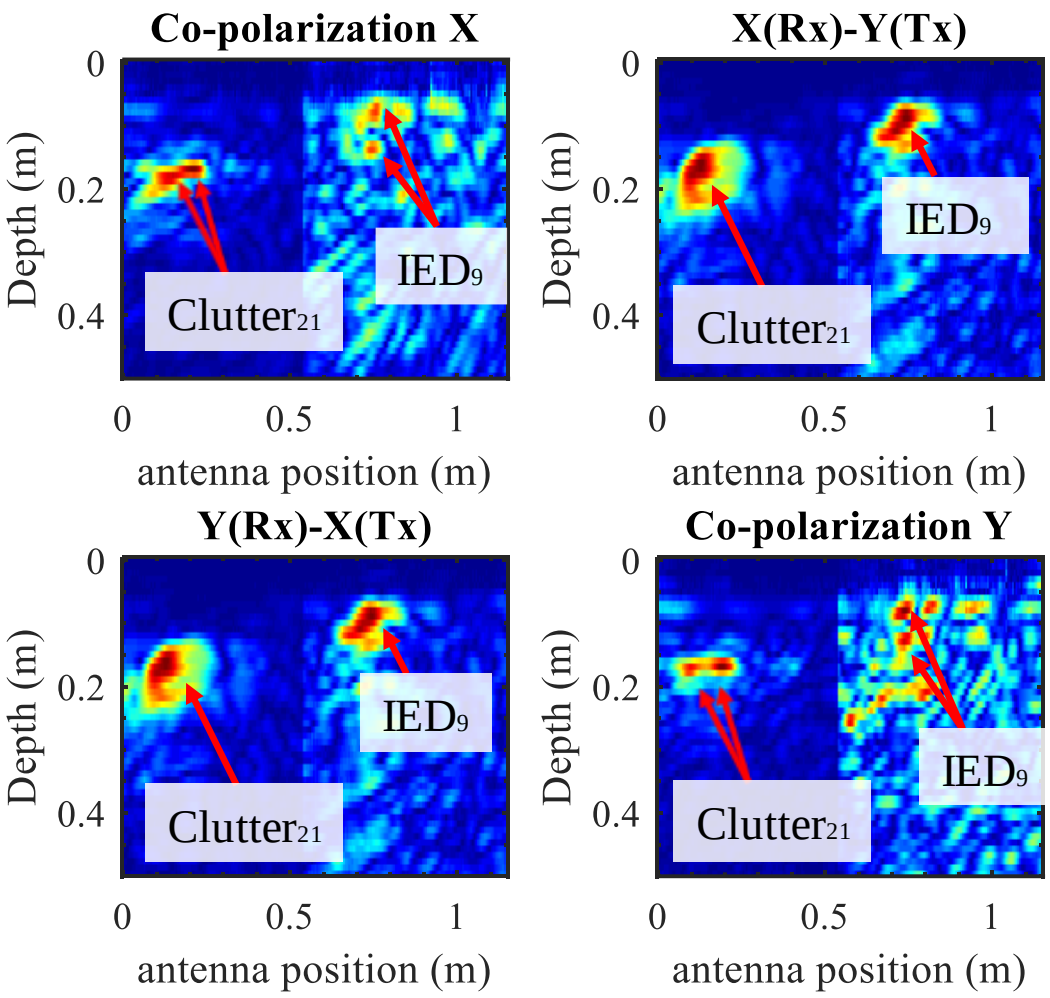

Figure 3-21: Polarimetric B-scan using LPC filter in data processing and applying a sliding windowing normalization of size 0.5 m width. Results of laboratory measurement for sandbox120. Clutter reflections around the IED target are increased after the sliding windowing normalization is applied.

3.5.2 Field measurements results

The field measurements are performed using different test targets to those used in laboratory measurements, as shown in Appendix A. Figure 3-22 and Figure 3-23 show the polarimetric B-scan after data processing using the RLS and LPC filters, respectively. This field measurement is labeled as field19, and two IEDs are scanned, IED_2 and IED_4.

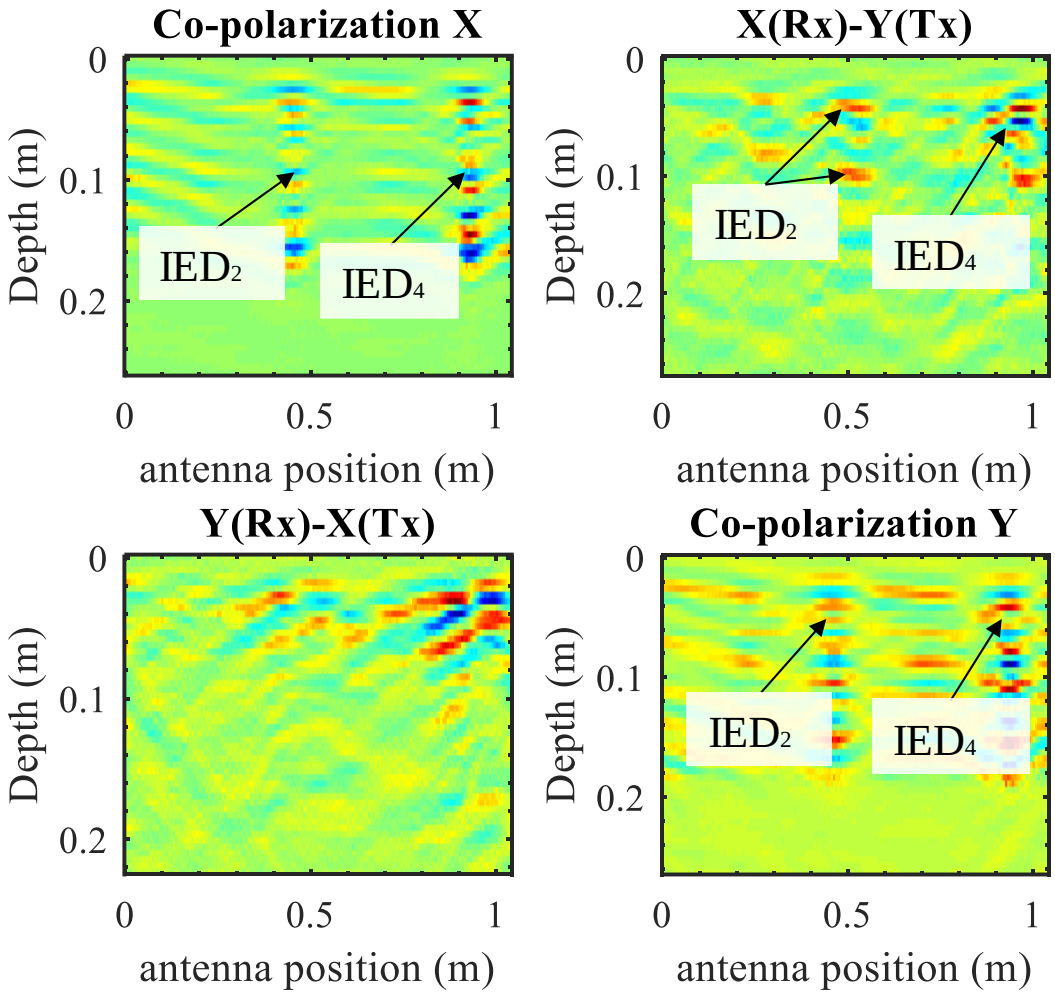

Figure 3-22: Polarimetric B-scan using RLS filter in data processing. Results of measurement for field19. The soil surface reflections are successfully removed. Clutter reflections are still present in the B-scans images. Both IED targets are localized in all polarizations.

In Figure 3-22 and Figure 3-23, we can see both IEDs in all polarizations. Moreover, multiple reflections are visualized in the co-polarization B-scans. In contrast, in the cross-polarization B-scan, the IEDs reflections are concentrated and visualized as spots in the position where the IEDs are buried.

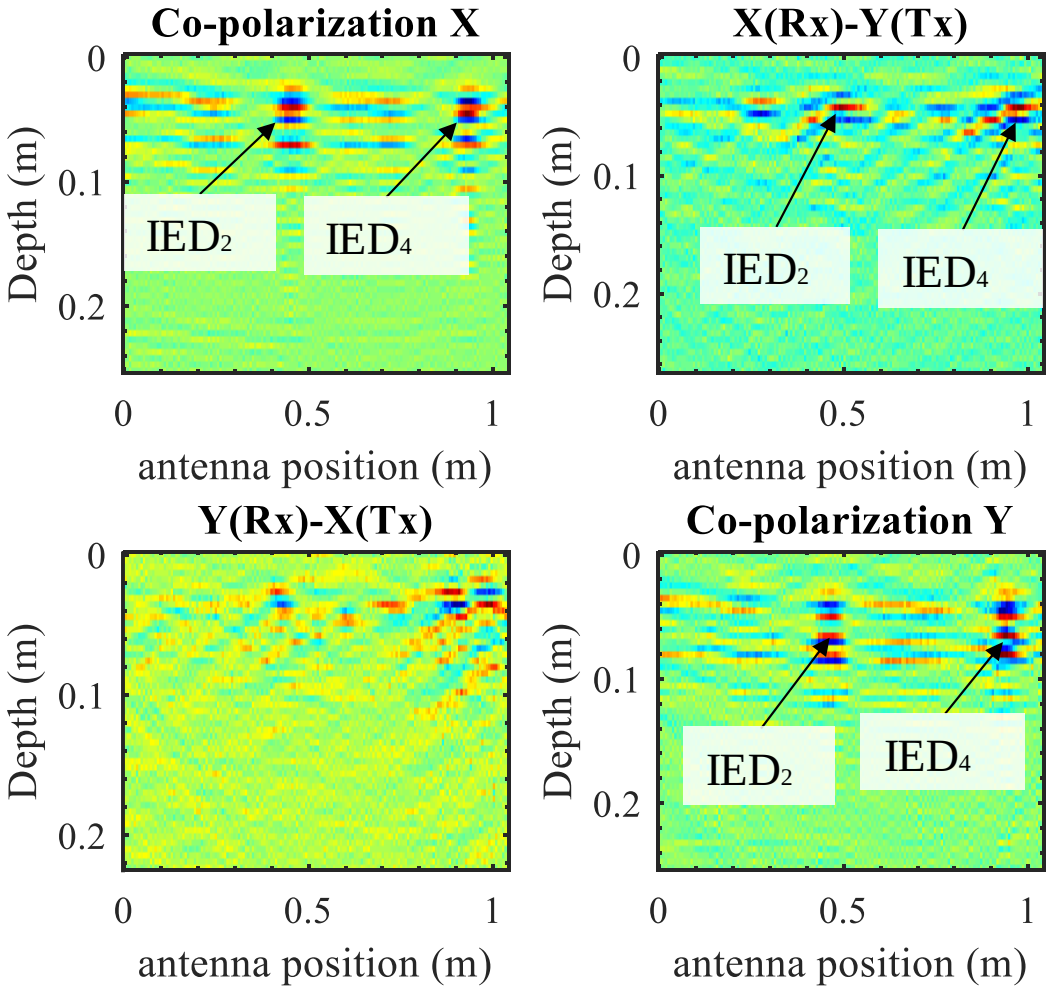

Figure 3-23: Polarimetric B-scan using LPC filter in data processing. Results of measurement for field19. Clutter reflections are present the B-scans images and the IEDs targets discontinuity is spread.

Figure 3-24 and Figure 3-25 show the polarimetric B-scans after data processing of the measurements labeled as field47. In this measurement, one clutter object is scanned, Clutter$_4$. We can observe the reflections of the clutter in all polarizations.

In the field measurements, results in Figure 3-22 to Figure 3-25 show that reflections from the soil are still in the B-scans. Furthermore, the target can be clearer seen with RLS than with LPC configuration. Therefore, in the field measurements, the target localization is selected from the RLS results.

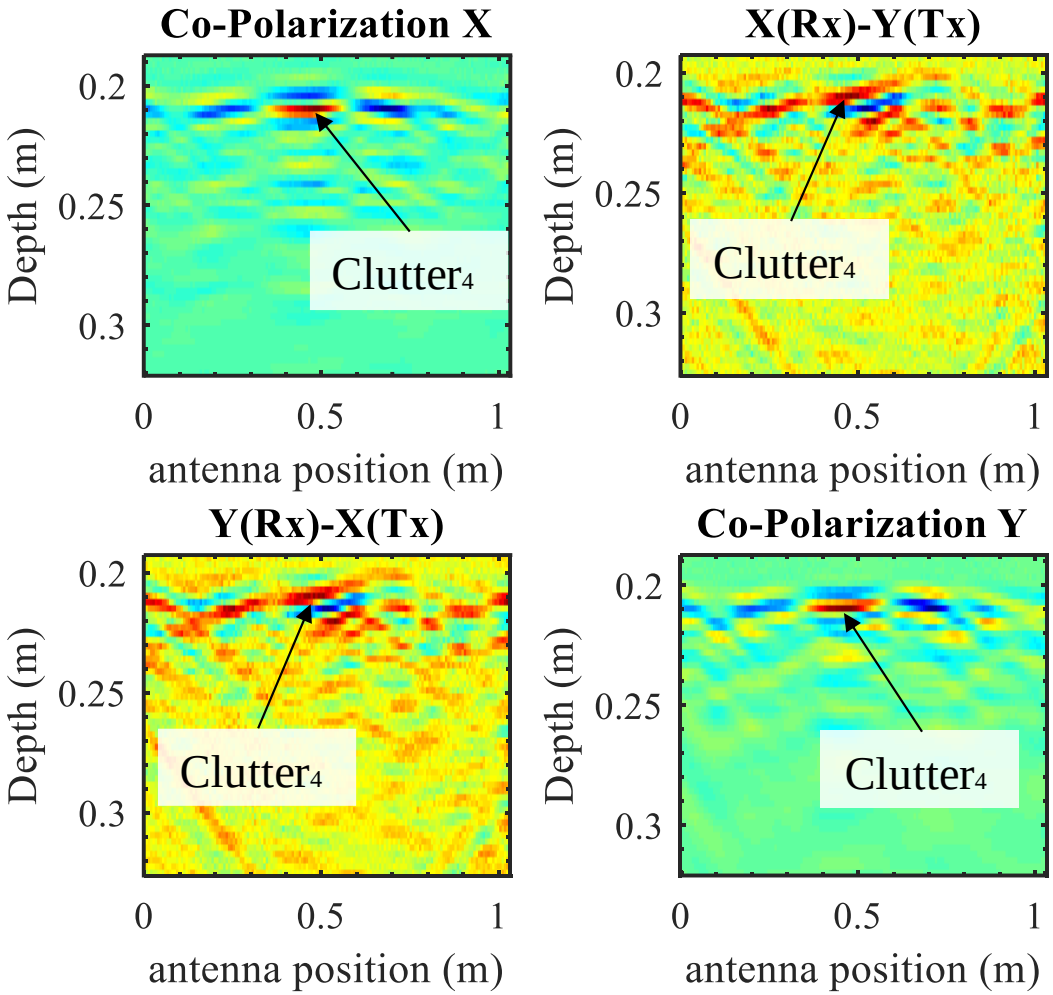

Figure 3-24: Polarimetric B-scan using RLS filter in data processing. Results of measurement for field47. The clutter object is well localized in the co-polarized images. In contrast, this clutter object produces cross-polarized reflections with similar values to clutter reflections and the target is difficult to be localized in the cross-polarized B-scan image.

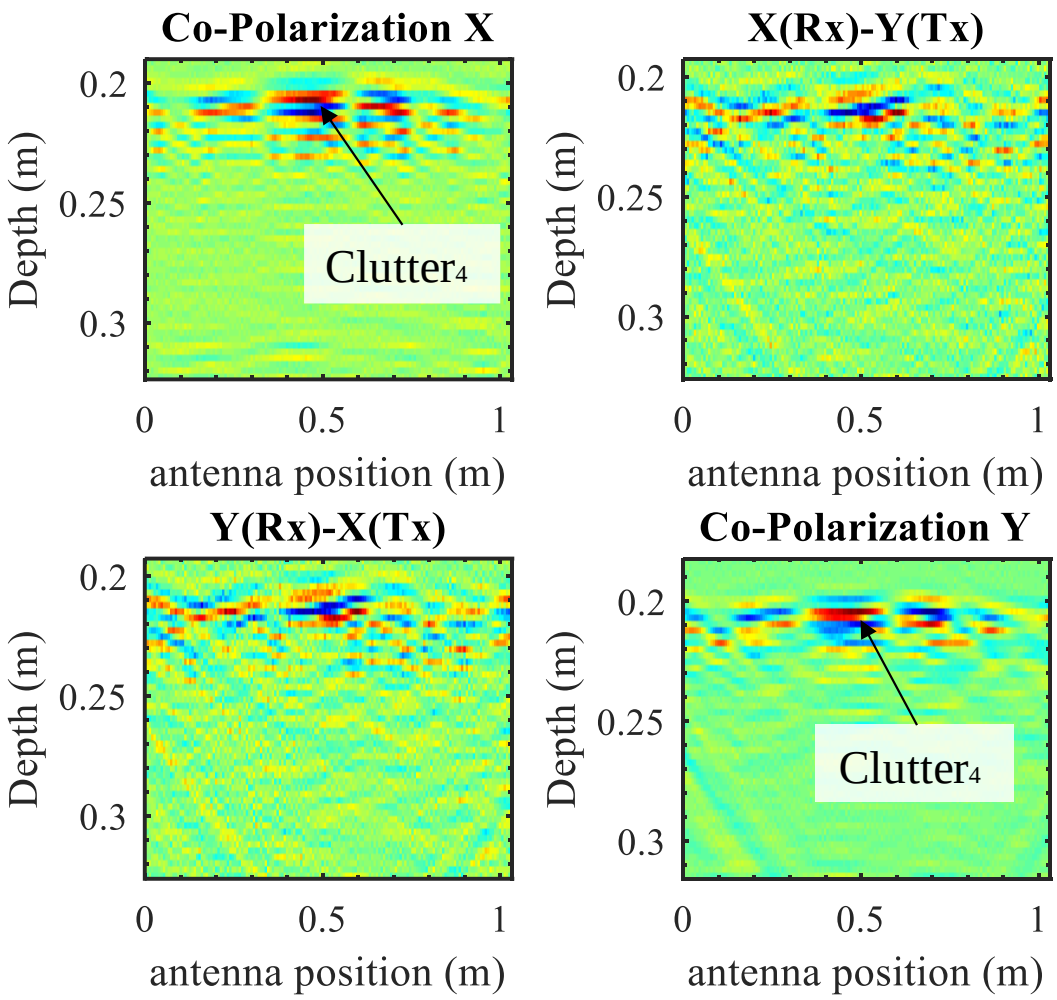

Figure 3-25: Polarimetric B-scan using LPC filter in data processing. Results of measurement for field47. The clutter object is localized in the co-polarized images.

3.6 Conclusion

The proposed polarimetric GPR system and data processing scheme were presented and discussed. The system was validated in two measurement scenarios.

The RLS and LPC adaptive filters were evaluated as data processing stages. The best results were provided by the RLS adaptive filter. This was even more noticeable in the field measurements.

The cross-polarization measurements make possible the detection of objects that partially trans-polarize the radiated signal. This behavior was evinced in the 40% of IEDs, which were clearly detected only in the cross-polarized B-scans.

The use of the sliding normalization window in the B-scan avoids that targets with high reflectivity hide the discontinuities of those with low reflectivity. Moreover, another strategy to avoid these hiding effects is using a smaller scanning track line, e.g. a track line of 40 cm instead of a 1 m track line.

4. Feature extraction of polarimetric data[3]

In this chapter, the construction of target feature vectors extracted from polarimetric GPR measurements is proposed. This procedure is applied to the polarimetric A-scans of the region of interest where the target is localized.

Time-frequency transformations and singular value decomposition are used as part of the feature extraction of polarimetric data and the proposed data processing methods. In total, eight data processing methods are used and the feature extraction of polarimetric data is performed for 30 targets. The extracted target feature vectors are validated in a binary classification approach using IED and Non-IED targets. The results are evaluated using performance metrics and the leave two-out cross-validation. Accuracy of 87.02% and a false positive rate of 10.53 % in the best classifier were obtained.

Part of the information and results presented in this chapter were previously published in [57] by the author of this thesis. The paper was entitled "Application of Polarimetric Features and Support Vector Machines for Classification of Improvised Explosive Devices".

4.1 Introduction

The previous chapter focused on the detection and localization of buried targets. However, the type of buried target is unknown. In this chapter, we are interested in knowing if these detected buried targets are an IED or a clutter object. In order to perform this categorization, the extraction of target features and a decision-making stage are developed.

---

[3] Part of the results shown in this chapter was published in S. Gutierrez, F. Vega, F. A. Gonzalez, C. Baer, and J. Sachs, 'Application of Polarimetric Features and Support Vector Machines for Classification of Improvised Explosive Devices', IEEE Antennas and Wireless Propagation Letters, pp. 1–4, 2019. DOI: 10.1109/LAWP.2019.2934691.

Target-signatures extracted from time-frequency transformations of co-polarized GPR measurements have been reported in [26], [69]–[71]. Furthermore, discrimination between landmines and dielectric targets, such as stones and plastic objects, by using singular values of time-frequency transformations have been proposed in [33], [61], [72].

The approach here proposed constructs the target feature vector (TFV) from the polarimetric GPR measurements, using two time-frequency transformations: the Wigner-Ville-Distribution (WVD) and the Continuous Wavelet Transform (CWT). The obtained TFV will be used as input of a Support Vector Machine (SVM) algorithm, in order to discriminate IEDs and Non-IEDs targets.

This chapter is organized as follows. The time-frequency transformations are explained in section 4.2. The extraction of polarimetric features is presented in section 4.3. Experimental data collection is described in section 4.4. The best support vector machine classifiers and their performance metrics are reported in section 4.6.

4.2 Time-Frequency transformations

4.2.1 Continuous Wavelet Transform

The Continuous Wavelet Transform (CWT) is a linear time-frequency transform able to achieve variable resolution in one domain, time or frequency, and multiresolution in the other domain [73]. The CWT uses a signal called wavelet, which is compressed or dilated by using a scale factor, in addition to being translated by a shifting parameter. Therefore, CWT decomposed the time signal $s(t)$ into a continuous set of wavelets at different scales and positions. Lower scales correspond to higher frequencies and vice versa. The CWT of a signal $s(t)$ is defined as:

$$\mathrm{CWT}(\alpha,\tau)=\frac{1}{\sqrt{\alpha}}\int_{-\infty}^{\infty}s(t)\psi\left(\frac{t-\tau}{\alpha}\right)dt, \tag{4.1}$$

where $\psi(t)$ is the mother wavelet, α is the scale factor, and τ is the time shift. The absolute value of (4.1) is known as a scalogram, which can be plotted as a time-frequency function.

The mother wavelet must satisfy some mathematical properties. For example, it must have finite energy and zero mean. Several kinds of wavelets have been defined, some of them are used depending on the application or their similarity with the signal under analysis.

4.2.2 Wigner-Ville distribution

The Wigner-Ville Distribution (WVD) is a quadratic transform that represents the energy of the signal as a time-frequency distribution. The WVD of an analytic signal $s(t)$ is given by [73], [74]:

$$\mathrm{WVD}(t,f)=\int_{-\infty}^{\infty} s(t+\frac{\tau}{2})s^{*}(t+\frac{\tau}{2})e^{-j2\pi f\tau}d\tau. \tag{4.2}$$

Moreover, the WVD in the frequency domain is defined by

$$\mathrm{WVD}(t,f)=\int_{-\infty}^{\infty} S(f+\frac{\theta}{2})S^{*}(f-\frac{\theta}{2})e^{-j2\pi t\theta}d\theta, \tag{4.3}$$

where $S(f)$ is the Fourier Transform of the analytic signal $s(t)$.

Among WVD properties [73]–[75], the next four properties are summarized. First, the WVD of any signal is always real.

Second, the marginal properties are satisfied and defined as [75]:

$$\int_{-\infty}^{\infty} \mathrm{WVD}(t,f)df=\left|s(t)\right|^{2}, \tag{4.4}$$

$$\int_{-\infty}^{\infty} \mathrm{WVD}(t,f)dt=\left|S(f)\right|^{2}. \tag{4.5}$$

Equation (4.4) obtains the instantaneous energy of the signal at a particular time instance, by summing the time-frequency distribution over all frequencies [73]. Moreover, the integration of (4.4) in the interval $t_a < t < t_b$ yields the relation of the energy contained in $s(t)$ in the same time interval, as follows [74]:

$$\int_{t_a}^{t_b}\int_{-\infty}^{\infty} \mathrm{WVD}(t,f)df\,dt=\int_{t_a}^{t_b}\left|s(t)\right|^{2}dt. \tag{4.6}$$

Additionally, equation (4.5) obtains the power spectrum of the signal at a particular frequency, by summing the time-frequency distribution over all time [73]. Integration of (4.5) over the frequency interval $f_a < f < f_b$ is equal to the energy contained in *s* in the same interval [74], [75]. This relation can be expressed as:

$$\int_{f_a}^{f_b}\int_{-\infty}^{\infty} \mathrm{WVD}(t,f)dtdf=\int_{f_a}^{f_b}\left|S(f)\right|^{2}df. \tag{4.7}$$

Therefore, the total energy of the signal $s(t)$ is the integral of the WVD over the whole plane (t, f), as follows [74]:

$$\int_{-\infty}^{\infty}\int_{-\infty}^{\infty} \mathrm{WVD}(t, f)df\,dt = \int_{-\infty}^{\infty} |s(t)|^2\,dt = \|s(t)\|^2. \tag{4.8}$$

Third, the WVD of the sum of two signals $s(t) = s_1(t) + s_2(t)$ is defined as [73]:

$$\begin{aligned} &\mathrm{WVD}_s(t, f) = \mathrm{WVD}_{s1}(t, f) + \mathrm{WVD}_{s2}(t, f) + \mathrm{WVD}_{s1s2}(t, f) + \mathrm{WVD}_{s2s1}(t, f), \\ &\mathrm{WVD}_s(t, f) = \mathrm{WVD}_{s1}(t, f) + \mathrm{WVD}_{s2}(t, f) + 2\,\mathrm{Re}(\mathrm{WVD}_{s1s2}(t, f)), \end{aligned} \tag{4.9}$$

where the cross-WVD is calculated by:

$$\mathrm{WVD}_{s1s2}(t, f) = \int_{-\infty}^{\infty} s_1(t + \frac{\tau}{2}) s_2^*(t + \frac{\tau}{2}) e^{-j2\pi f\tau} d\tau. \tag{4.10}$$

The cross-terms interference is a drawback of the WVD. These terms appear in the WVD of multicomponent signals [73], [76].

Fourth, the WVD distribution of a time-limited signal is also time-limited. Similarly, if a signal is frequency-limited, its WVD distribution is frequency-limited [75].

In general, cross-terms of the WVD can appear due to multiple ground surface reflections or by reflections from the air-soil interface. Therefore, this unwanted effect was avoided by calculating the WVD of the signal after clutter removal.

In particular, the WVD is a 2-D representation of an A-scan. Moreover, the WVD of a target-signal after clutter removal is concentrated inside a dense zone of the time-frequency plane. Therefore, a submatrix was extracted by using a time-limited A-scan and knowing the bandwidth of the system. The time window width is fixed and it guarantees that at least a depth of 20 cm in the A-scan is processed.

4.3 Construction of the target feature vector

In this section, we describe the TFVs constructed from the CWT and WVD transformations applied to the polarimetric measurements.

As described in section 3.2.4, a polarimetric measurement is composed of two A-scans with co-polarized antenna configuration, and two with cross-polarized configuration. Therefore, the

application of the CWT or the WVD transformation in a single polarimetric measurement produces four matrices. This transformation of a polarimetric measurement can be expressed as a matrix of matrices as follows:

$$\begin{pmatrix} \mathbf{M}_{11} & \mathbf{M}_{12} \\ \mathbf{M}_{21} & \mathbf{M}_{22} \end{pmatrix}, \tag{4.11}$$

where the matrices $\mathbf{M}_{11}$ and $\mathbf{M}_{22}$ are the time-frequency representation of an A-scan measured with the co-polarized antennas in X and Y direction, respectively. $\mathbf{M}_{12}$ is the cross-polar configuration, i.e. when the Y-polarized antenna is transmitting and the X-polarized antenna is receiving. Similarly, $\mathbf{M}_{21}$ is the time-frequency representation when the X-polarized antenna is transmitting and the Y-polarized antenna is receiving.

As an example, Figure 4-1 shows the WVD of a polarimetric measurement arranged as the matrix representation (4.11). The four processed A-scans are located at 0.98 m in the field measurement of the IED 4, depicted in Figure 3-22.

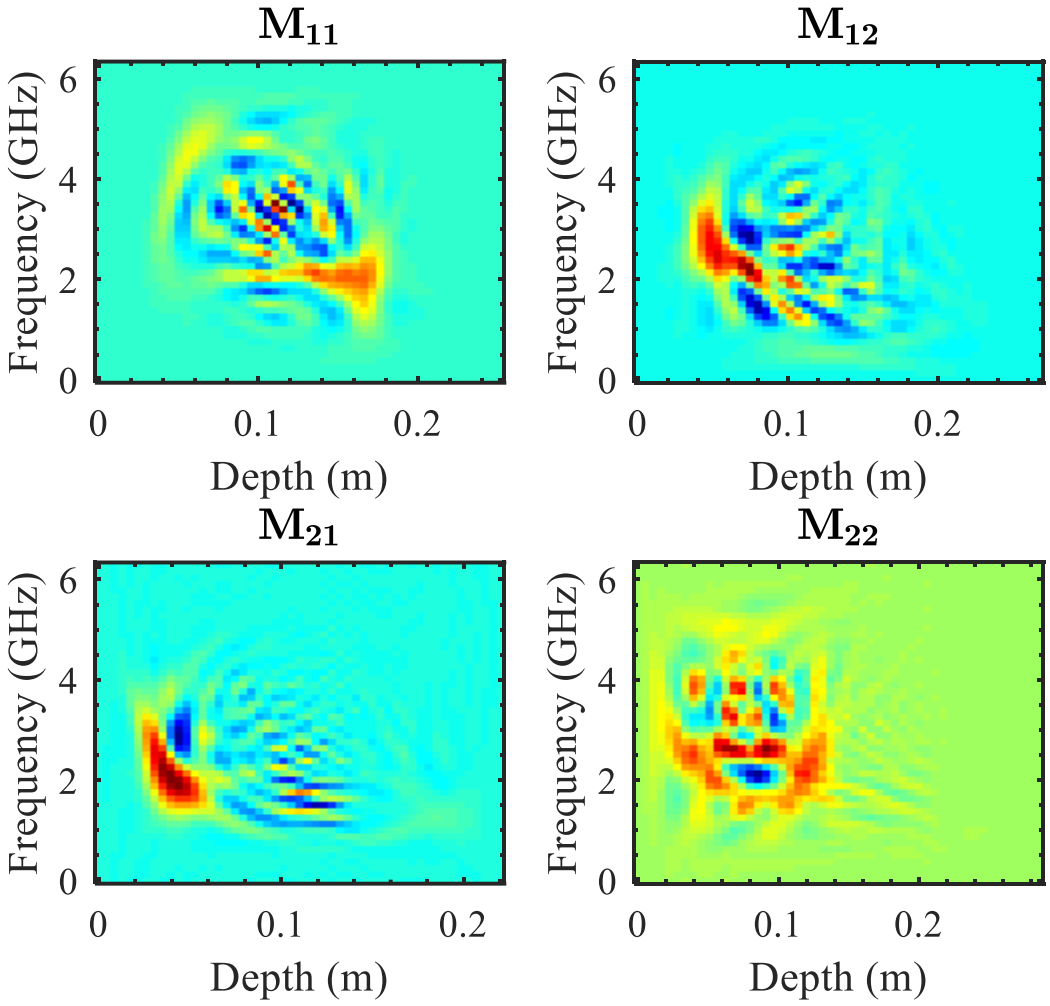

Figure 4-1: Matrix representation of the WVD of a polarimetric measurement. The processed data are from the antenna position 0.98m in the field19 measurement, target IED4.

In order to reduce the dimensionality of these data, we propose to construct the feature vectors from the singular value decomposition (SVD) of each of these matrices, as follows.

The SVD of any individual submatrix $\mathbf{M}$ in (4.11) is given by:

$$\underset{mxn}{\mathbf{M}} = \underset{mxm}{\mathbf{U}}\ \underset{mxn}{\mathbf{\Sigma}}\ \underset{nxn}{\mathbf{V}^T}, \quad \mathbf{\Sigma} = \mathrm{diag}(\sigma_k), \text{ with } k = 1, \cdots, R \quad , \tag{4.12}$$

where the columns of the orthogonal matrices $\mathbf{U}$ and $\mathbf{V}$ are the left-singular and right-singular vectors, respectively; σ_k are the singular values arranged in the rectangular diagonal matrix $\mathbf{\Sigma}$; R is the rank of the matrix $\mathbf{M}$ defined as $R = \min(m, n)$. The original image matrix $\mathbf{M}$ in Equation (4.12) can be decomposed by matrices or images $\mathbf{A}_k$ as:

$$\mathbf{M} = \sum_{k}^{R} \mathbf{A}_k = \sum_{k}^{R} \sigma_k \mathbf{u}_k \otimes \mathbf{v}_k, \tag{4.13}$$

$$\tilde{\mathbf{M}} = \sum_{k=1}^{K} \mathbf{A}_k = \sum_{k=1}^{K} \sigma_k \mathbf{u}_k \otimes \mathbf{v}_k, K \le R, \tag{4.14}$$

where $\mathbf{A}_k$ is a matrix of dimension mxn and $\mathbf{u}_k \otimes \mathbf{v}_k$ is the outer product of the k^{th} left-singular and right-singular columns. In consequence, $\tilde{\mathbf{M}}$ in (4.14) is the approximation of the matrix $\mathbf{M}$ by using K images.

Since the total energy contained in $\mathbf{M}$ can be calculated by:

$$E_{\mathrm{M}} = \sum_{k=1}^{R} \sigma_k{}^2, \tag{4.15}$$

the energy contained by the approximation $\tilde{\mathbf{M}}$ (4.14) can be calculated as:

$$E_{\tilde{\mathrm{M}}} = \sum_{k=1}^{K} \sigma_k{}^2. \tag{4.16}$$

Additionally, if the rows of the time-frequency transformation correspond to time-domain and the columns correspond to frequency-domain; then $\mathbf{u}_k$ can be interpreted as the distribution of energy in frequency-domain and $\mathbf{v}_k$ in time-domain.

The next stage is to extract σ_k, u_k, v_k from the first K images, which are the most energetic components in Equation (4.16), and use them as parameters in a feature vector. Therefore, two sets of parameters are calculated as the normalized center of gravity of the singular vectors, as follows [33], [61]:

$$\delta_{t,k} = \frac{1}{t_2 - t_1} \frac{\sum_{n=1}^{N} t(n) \left| \mathbf{v}_k(n) \right|^2}{\sum_{n=1}^{N} \left| \mathbf{v}_k(n) \right|^2}, \quad \mathrm{k} = 1, \cdots, K \ , \tag{4.17}$$

$$\delta_{f,k} = \frac{1}{f_2 - f_1} \frac{\sum_{m=1}^{M} f(m) \left| \mathbf{u}_k(m) \right|^2}{\sum_{m=1}^{M} \left| \mathbf{u}_k(m) \right|^2}, \quad \mathrm{k} = 1, \cdots, K \ , \tag{4.18}$$

where $t_2 - t_1$ is the effective time duration of $\mathbf{M}$; $f_2 - f_1$ are their bandwidth; t and f are the vectors of time and frequency, respectively. If the singular vectors of the SVD are normalized to the unit, then (4.17) and (4.18) are simplified as

$$\delta_{t,k} = \frac{1}{t_2 - t_1} \sum_{n=1}^{N} t(n) \left| \mathbf{v}_k(n) \right|^2, \quad k = 1, \cdots, K \quad , \tag{4.19}$$

$$\delta_{f,k} = \frac{1}{f_2 - f_1} \sum_{m=1}^{M} f(m) \left| \mathbf{u}_k(m) \right|^2, \quad k = 1, \cdots, K \quad , \tag{4.20}$$

In addition, the parameters extracted from σ_k comprise the normalized singular values of the energy of $\mathbf{M}$, which are defined as [33], [72]:

$$\delta_{e,k} = \frac{\sigma_k}{\sqrt{\sum_{k=1}^{R} {\sigma_k}^2}} = \frac{\sigma_k}{\sqrt{E_{\mathrm{M}}}}, \quad k = 1, \cdots, K \quad . \tag{4.21}$$

Finally, the feature vectors are assembled using the parameters $\delta_{t,k}, \delta_{f,k}, \delta_{e,k}$, called herein singular parameters. The proposed polarimetric feature vectors are summarized in Table 4-1. Therefore, by using (4.17), (4.18), and (4.21), the required parameters are extracted from each of the four submatrices $\mathbf{M}$ in Equation (4.11). For example, the feature vector $\mathbf{D}_1(\delta_{t,1})$ uses the first right- singular vector of the SVD, that is, the parameter $\delta_{t,1}$ of the first set of singular parameters. Therefore, the total number of features in $\mathbf{D}_1$ is equal to four. Similarly, the feature vectors from $\mathbf{D}_1$ to $\mathbf{D}_6$ use the parameters $\delta_{t,k}, \delta_{f,k}, \delta_{e,k}$ separately, where *k* takes the value of one or two in order to use the first or second singular parameters. The feature vectors $\mathbf{D}_7$ to $\mathbf{D}_{13}$ combine the first three singular parameters.

Table 4-1: Polarimetric target feature vectors.

Name (δ parameters)	Target Feature Vector	Length
$\mathbf{D}_1(\delta_{t,1})$	$[\delta_{t,1}(\mathbf{M}_{1,1}),\delta_{t,1}(\mathbf{M}_{1,2}),\delta_{t,1}(\mathbf{M}_{2,1}),\delta_{t,1}(\mathbf{M}_{2,2})]$	4
$\mathbf{D}_2(\delta_{f,1})$	$[\delta_{f,1}(\mathbf{M}_{1,1}),\delta_{f,1}(\mathbf{M}_{1,2}),\delta_{f,1}(\mathbf{M}_{2,1}),\delta_{f,1}(\mathbf{M}_{2,2})]$	4
$\mathbf{D}_3(\delta_{\sigma,1})$	$[\delta_{\sigma,1}(\mathbf{M}_{1,1}),\delta_{\sigma,1}(\mathbf{M}_{1,2}),\delta_{\sigma,1}(\mathbf{M}_{2,1}),\delta_{\sigma,1}(\mathbf{M}_{2,2})]$	4
$\mathbf{D}_4(\delta_{t,2})$	$[\delta_{t,2}(\mathbf{M}_{1,1}),\delta_{t,2}(\mathbf{M}_{1,2}),\delta_{t,2}(\mathbf{M}_{2,1}),\delta_{t,2}(\mathbf{M}_{2,2})]$	4
$\mathbf{D}_5(\delta_{f,2})$	$[\delta_{f,2}(\mathbf{M}_{1,1}),\delta_{f,2}(\mathbf{M}_{1,2}),\delta_{f,2}(\mathbf{M}_{2,1}),\delta_{f,2}(\mathbf{M}_{2,2})]$	4
$\mathbf{D}_6(\delta_{\sigma,2})$	$[\delta_{\sigma,2}(\mathbf{M}_{1,1}),\delta_{\sigma,2}(\mathbf{M}_{1,2}),\delta_{\sigma,2}(\mathbf{M}_{2,1}),\delta_{\sigma,2}(\mathbf{M}_{2,2})]$	4
$\mathbf{D}_7(\delta_{t,1},\delta_{f,1},\delta_{\sigma,1})$	$[\delta_{t,1}(\mathbf{M}_{i,j}),\delta_{f,1}(\mathbf{M}_{i,j}),\delta_{\sigma,1}(\mathbf{M}_{i,j})];\ i,j=1,2.$	12
$\mathbf{D}_8(\delta_{t,2},\delta_{f,2},\delta_{\sigma,2})$	$[\delta_{t,2}(\mathbf{M}_{i,j}),\delta_{f,2}(\mathbf{M}_{i,j}),\delta_{\sigma,2}(\mathbf{M}_{i,j})];$ i,j=1,2.	12
$\mathbf{D}_9(\delta_{t,1}\cdot\delta_{f,1},\delta_{t,2}\cdot\delta_{f,2},\delta_{\sigma,1})$	$[\delta_{t,1}\cdot\delta_{f,1}(\mathbf{M}_{i,j}),\delta_{t,2}\cdot\delta_{f,2}(\mathbf{M}_{i,j}),\delta_{\sigma,1}(\mathbf{M}_{i,j})];\ i,j=1,2.$	12
$\mathbf{D}_{10}(\delta_{t,1}\cdot\delta_{f,1},\delta_{t,2}\cdot\delta_{f,2},\delta_{\sigma,1},\delta_{\sigma,2})$	$[\delta_{t,1}\cdot\delta_{f,1}(\mathbf{M}_{i,j}),\delta_{t,2}\cdot\delta_{f,2}(\mathbf{M}_{i,j}),\delta_{\sigma,1}(\mathbf{M}_{i,j}),\delta_{\sigma,2}(\mathbf{M}_{i,j})];$ $i,j=1,2.$	16
$\mathbf{D}_{11}(\delta_{t,1},\delta_{f,1},\delta_{\sigma,1},\delta_{t,2},\delta_{f,2})$	$[\delta_{t,1}(\mathbf{M}_{i,j}),\delta_{f,1}(\mathbf{M}_{i,j}),\delta_{\sigma,1}(\mathbf{M}_{i,j}),\delta_{t,2}(\mathbf{M}_{i,j}),\delta_{f,2}(\mathbf{M}_{i,j})];$ $i,j=1,2.$	20
$\mathbf{D}_{12}(\delta_{t,k},\delta_{f,k},\delta_{\sigma,k}),\ \mathrm{k}=1,\cdots,2$	$[\delta_{t,k}(\mathbf{M}_{i,j}),\delta_{f,k}(\mathbf{M}_{i,j}),\delta_{\sigma,k}(\mathbf{M}_{i,j})];\ k=1,\cdots,2;$ $i,j=1,2.$	24
$\mathbf{D}_{13}(\delta_{t,k},\delta_{f,k},\delta_{\sigma,k}),\ \mathrm{k}=1,\cdots,3$	$[\delta_{t,k}(\mathbf{M}_{i,j}),\delta_{f,k}(\mathbf{M}_{i,j}),\delta_{\sigma,k}(\mathbf{M}_{i,j})];\ k=1,\cdots,3;$ $i,j=1,2.$	36

4.4 Experimental data collection

In order to extract the TFVs and discriminate between IEDs and clutter objects, the following data processing procedure, shown in Figure 3-11, is proposed. The polarimetric B-scan and the target position, calculated in the previous chapter, are used as inputs in the current procedure.

1. Targets were detected in the normalized B-scan. Then, using the target position and the polarimetric B-scan, five A-scans were extracted from the region where each target was detected.
2. The time-frequency transformation was applied to the selected A-scans and the result is the **M** matrix, as expressed in Equation (4.11). Notice that, this transformation was applied to the A-scans before normalization.
3. The SVD was applied to each submatrix $\mathbf{M}$ and the approximation $\tilde{\mathbf{M}}$ was calculated using the Equation (4.12) and Equation (4.14), illustrative results of the matrices $\mathbf{M}$ and $\tilde{\mathbf{M}}$ are depicted in Appendix B. Then, using the first three most energetic components of $\tilde{\mathbf{M}}$, the 13 TFVs presented in Table 4-1 were constructed. The 30 targets measured in the experimental GPR data collection (section 3.4) were used and their TFVs were constructed.
4. The TFVs of the 30 targets were partitioned in two data sets to train and test the SVM, which use a radial basis function kernel.
5. The performance of the SVM was assessed. The experiment was validated by using leave-two-out cross-validation [77], which will be explained in the following section.

The described procedure was performed with all the processing alternatives proposed, i.e. using the four time-frequency transformations and the two adaptive filters. Therefore, eight data processing methods are proposed, as presented in Table 4-2. In total, 104 TFVs were constructed and validated with the above-explained procedure.

Table 4-2: Data processing methods.

Method		**Feature vectors**
1	RLS+WVD	$\{\mathbf{D}_1,\cdots,\mathbf{D}_{13}\}$
2	RLS+Morse	$\{\mathbf{D}_1,\cdots,\mathbf{D}_{13}\}$
3	RLS+Morlet	$\{\mathbf{D}_1,\cdots,\mathbf{D}_{13}\}$
4	RLS+Bump	$\{\mathbf{D}_1,\cdots,\mathbf{D}_{13}\}$
5	LPC+WVD	$\{\mathbf{D}_1,\cdots,\mathbf{D}_{13}\}$
6	LPC+Morse	$\{\mathbf{D}_1,\cdots,\mathbf{D}_{13}\}$
7	LPC+Morlet	$\{\mathbf{D}_1,\cdots,\mathbf{D}_{13}\}$
8	LPC+Bump	$\{\mathbf{D}_1,\cdots,\mathbf{D}_{13}\}$

4.5 Validation

In general, the SVM is a supervised machine learning algorithm that can be used for regression or classification problems. In this research, it is used in a binary classification problem where the true class is the IED and the false class is the Non-IED. The results of the SVM decision stage are analyzed under the leave-two-out cross-validation structure and the SVM classifier performance are evaluated using the metrics that will be explained in the next subsection. The cross-validation of the experiment is performed in order to get an accurate classifier performance estimation and avoid biased analysis of its metrics.

In the leave-two-out cross-validation, a given data set of N elements are partitioning into two subsets, training and testing. This partition leaves out two elements from the training set, which are included in the testing set, but one of these elements must be from the true class and one from the negative class. Consequently, the SVM is trained on a subset and the testing data is used to evaluate the SVM performance. In a random partition of the data set, using a run of the leave-two-out cross-validation method, we get N/2 different pairs of leave-two-out elements. Therefore, in order to get more reliable error estimates and using average over averages, the cross-validation is performed multiples times for different random partitions.

4.5.1 Performance metrics

The performance metrics of the SVM classifiers are based on: false positives (FP), which are the number of Non-IED misclassified as IEDs; true positives (TP), i.e. the number of IEDs correctly classified; false negatives (FN), which are the number of IEDs misclassified as Non-IEDs; and true negatives (TN), i.e. the number of Non-IEDs correctly classified.

Three metrics are selected, which can be expressed as:

$$\begin{aligned} \text{Recall} &= \frac{\text{TP}}{\text{P}} = \frac{\text{TP}}{\text{TP+FN}}; \\ \text{Specificity} &= \frac{\text{TN}}{\text{N}} = \frac{\text{TN}}{\text{TN+FP}}; \\ \text{Accuracy} &= \frac{\text{TP+TN}}{\text{P+N}} = \frac{\text{TP+TN}}{\text{TP+TN+FP+FN}}, \end{aligned} \tag{4.22}$$

where recall is the rate of true positives out of the total positives samples; specificity is the rate of true negatives out of the total negatives samples; and accuracy is the proportion of samples, TP and TN, correctly classified.

4.6 Results

The SVMs classifiers of each feature vector (Table 4-1) were implemented in every data processing method presented in Table 4-2. These classifiers were trained and tested using leave-two-out cross-validation. The experiment was repeated 30 times using different random initializations in order to partition the data differently. Consequently, training and testing sets were unlike at each experiment. Finally, the performance metrics of the SVM were computed in each classification run; the results are averaged and the best classification methods are reported in Table 4-3.

Table 4-3: SVM performance metrics of the proposed data processing methods.

Method		Best feature vector	Recall %	Specificity %	Accuracy %
1	RLS+WVD	$\mathbf{D_1}$	80.40 ± 2.16	83.87 ± 1.81	67.13 ± 1.51
2	RLS+Morse	$\mathbf{D_1}$	75.20 ± 1.51	72.13 ± 1.23	73.67 ± 1.09
3	RLS+Morlet	$\mathbf{D_{13}}$	84.58 ± 2.52	89.47 ± 2.14	87.02 ± 1.81
4	RLS+Bump	$\mathbf{D_1}$	86.62 ± 2.44	52.00 ± 1.95	69.31 ± 1.65
5	LPC+WVD	$\mathbf{D_4}$	84.71 ± 1.67	42.04 ± 3.53	63.38 ± 1.61
6	LPC+Morse	$\mathbf{D_2}$	72.67 ± 2.66	72.62 ± 1.71	72.64 ± 1.91
7	LPC+Morlet	$\mathbf{D_1}$	78.53 ± 3.36	59.24 ± 0.76	68.89 ± 1.71
8	LPC+Bump	$\mathbf{D_2}$	73.42 ± 1.48	77.47 ± 3.10	75.44 ± 1.59

Besides, classification methods can be analyzed in the humanitarian demining context, where IEDs classification requires that all IED targets are detected and deactivated. Therefore, the ideal classifier must have 100% in recall (true positive rate) and a lower false positive rate (FPR). Moreover, some level of missed mines (false negatives rate FNR) means that the area cannot be declared free of IEDs and also leading risky conditions for the deminers. For this reason, currently, all targets detected by deminers are treated as IEDs and the deminers must perform the manual search in order to deactivate it or visually confirm that the target is a Non-IED.

Among the proposed classifiers methods, method eight has well-balanced metrics, but the accuracy is only 75%. The method four has the best recall with 86.62%, but this value is not suitable for humanitarian demining.

Therefore, the best accuracy result is 87.02%, and it is obtained with method three. Moreover, its recall is 84,58% and consequently, the FNR is 15.42%, which meets no safety condition (FNR = 0%) for identifying IEDs. Despite the requirement in the false negative rate, method three has promising specificity values of 89.47% and consequently, the FPR is 10.53%. This means that our best classifier has a good performance assuring that a target is a Non–IED (True negative); an illustrative result is shown in Figure 4-2. In conclusion, the classifier method three (i.e. RLS filter, Morlet CWT transform and feature vector D13) can be used in humanitarian demining as negative test evaluation, increasing the demining rate because manual exploration of Non-IED targets is reduced.

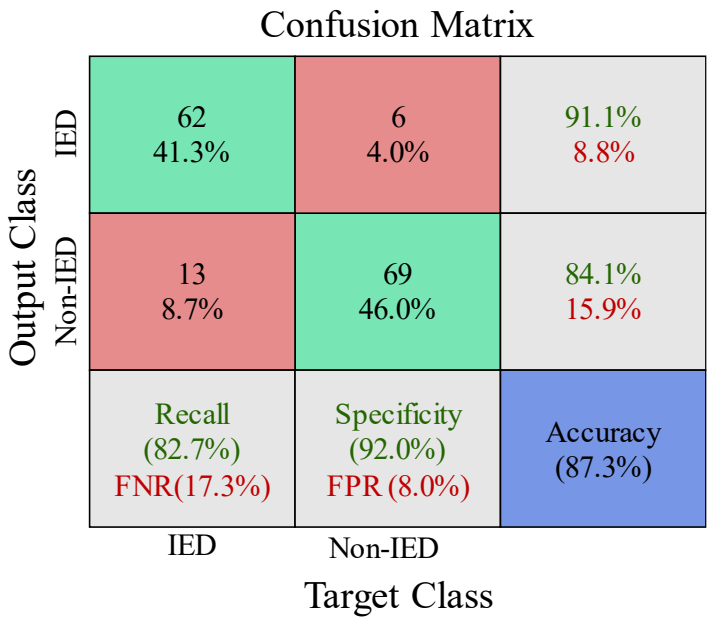

Figure 4-2: Confusion matrix for an experiment of the classification method 3.

4.7 Conclusion

In this chapter, a procedure to construct target feature vectors from polarimetric GPR measurements was presented. Moreover, target feature vectors were validated and used as input of an SVM algorithm, in order to discriminate IEDs from Non-IEDs under different test conditions.

The SVM and the constructed target feature vectors have promising results of being used as a negative test in the humanitarian demining context. However, the accuracy of the SVM performance is affected by the clutter removal stage and data processing of the polarimetric GPR measurements. That is, among the eight data processing structures, the best results were obtained in those that use the RLS adaptive filter in the clutter removal stage. Similarly, although the WVD provides a better resolution in the time-frequency plane, the data processing methods that use the CWT have better accuracy results for discriminating IEDs and Non-IEDs targets.

In general, the proposed classification methods require further field measurements in order to train them under more test conditions and increasing the number of samples. Moreover, other machine learning techniques such as convolutional neural networks can be tested and compared with the performance of the SVM.

5. Conclusion

In this chapter, the main results of the thesis are summarized. First, the results of the ANFO permittivity measurement stage are described. Afterward, the main achievements reached with time-frequency transformations applied to polarimetric GPR measurements are described. Then, the main results of the polarimetric target feature extraction and the SVM classification performance are explained. At the end of this chapter, the main conclusions and future work are presented.

5.1 Main results

As part of the permittivity measurements of ANFO, a field-deployable concept for permittivity measurement of explosives was introduced. Moreover, an integrate procedure with the reference plane invariant equations, the manufacturing of coaxial probes, and the calibration method was presented as an improvement of field calibration issues such as errors in the reference plane positioning, and asymmetrical error-terms of the mechanical transitions that adapt the coaxial specimen holder. Furthermore, the simplified direct method to calculate the permittivity can be implemented in a small PC due to its low computational requirements, besides being suitable to measure low-loss and lossy materials under field conditions.

For the first time, complex permittivity measurements of improvised ANFO explosives were reported. The results indicate a clear separation of the studied materials. The achieved precision of the measurements is sufficient for the purposes of this research. Moreover, the ANFO permittivity results contribute to the knowledge of the electrical properties of this kind of improvised explosives and of Colombian IEDs. In this research, the permittivity results were used to formulate an inert material-mixture that provides similar dielectric properties to those of ANFO.

Surrogate inert IEDs were manufactured and a comparable dielectric fingerprint of the most common Colombian IEDs was emulated. These surrogate IEDs are a product of this research and allowed us to set up GPR test targets. Furthermore, the developed material will be used to manufacture more

surrogate IEDs in order to perform further measuring campaigns under several field conditions. Moreover, these objects can be used to train deminers and test the performance of detection devices (e.g. GPR and metal detectors).

Polarimetric GPR measurements in laboratory and field scenarios were carried out by using dual-polarized Vivaldi antennas and ultra-wideband MIMO-GPR systems. Moreover, a data processing structure for polarimetric GPR measurements was set up and implemented. Two recursive algorithms, recursive least square and linear predictive coding, were used for data processing and clutter removal in time-domain.

In order to decrease the ground reflection in the polarimetric GPR system, we proposed to use forward-looking and side-looking antenna configuration, unlike hand-held detection devices that operate in a downward-looking antenna configuration. The proposed polarimetric GPR hardware/software structure shows satisfactory results removing clutter under laboratory and field measurements scenarios. The best results in terms of target localization were obtained by using the RLS structure. However, both RLS and LPC adaptive filters are useful for clutter removal in irregular surfaces and harsh soils conditions.

The UWB-MIMO-GPR system and data processing structure presented in this thesis allowed us to remove undesired clutter effects, produce polarimetric radar images, and localize target in the radar image. Moreover, these polarimetric GPR measurements were used to increase the extracted information from the backscattered signal of the buried targets.

Regarding the extraction of features of a common Colombian IED from their backscattered signal, it was done by time-frequency transformations of the A-scans, combined with singular value decomposition. This data processing procedure was applied to the polarimetric GPR measurements of 30 buried targets (between surrogate IEDs and clutter objects). In total, 13 feature vectors were assembled for each of the eight proposed data processing methods.

The proposed data processing methods and the polarimetric feature extraction approach provide more electromagnetic information of the common Colombian IEDs. Besides, the described data processing structure was decisive to find discriminating features between IEDs and clutter objects (Non-IED targets). For example, in the polarimetric B-scan, some targets were detected only in the

cross-polarized measure and no discontinuity was evidenced in the co-polarization measure, which affects directly the polarimetric features extracted to that target.

In order to compare the performance of the target features to discriminate Colombian IEDs from clutter objects, the assembled targets feature vectors were assessed in an SVM classification structure and the results were validated by using leave-two out cross-validation. Accuracy of 87.02% was obtained for the best classifier, i.e. the RLS structure, the Morlet CWT and the feature vector $\mathbf{D}_{13}$, which was assembled from the polarimetric features of the first three singular parameters.

The proposed approach for the extraction of targets features allows the detection of buried IEDs, based on their polarimetric properties. Moreover, the classification results by using SVM increases the demining rate, compared with metal detectors in a humanitarian demining context, because the manual exploration of Non-IED targets is reduced if the reported classifier methods are used as negative test evaluation.

5.2 Conclusion

Results show that integration between the polarimetric GPR measurements, the explained data processing structure and the construction of the target feature vector using the proposed methodology allows discrimination between IEDs and Non-IEDs targets. Furthermore, the best classifier reported in this thesis has an accuracy of 87.02% and an FPR of 10.53%, which means an improvement in the accuracy in 37.02% and the FPR is better in 89.47% compared with the metal detector, whose performance has an accuracy of 50% and an FPR of 100%.

The Polarimetric B-scan structure is determining in the discrimination of targets because some measurements are only detected in the cross-polarized measure and no target discontinuity is evidenced in the co-polarization measure. Therefore, if a GPR uses only the co-polarization configuration, then is not able to detect this kind of targets, which affects directly the discrimination performance and increase the risk for the deminers.

It was shown that methodologies that improve the detection and localization of targets may decrease the quality of the constructed target feature vectors, e.g. the sliding normalization improves the target discontinuity in the B-scans. However, apply the WVD to normalized B-scans produce a spread of energy in the time-frequency plane and is not possible to extract useful features from that results.

The tilted antenna configuration and polarimetric GPR measurements improve the clutter removal performance due to the low cross-polarization levels of the ground reflections. Moreover, tilt the antenna incidence angle decreases the surface ground reflections and increase the soil-transmitted power. Therefore, the combination of those effects with the sensitivity of the polarimetric GPR system to polarizing targets increases the target discontinuity and the image contrast in the polarimetric B-scan. However, the optimum incidence angle must be adjusted depending on the permittivity of the soil. Currently, in order to change the incidence angle dynamically, the antenna structure is being redesigned and those modifications will be considered in future work.

The ANFO permittivity can be measured on the field with the proposed measurement methodology by using coaxial probes. Moreover, further explosives materials can be characterized. However, security procedures, explosive experts, handling restrictions and law constraints must be considered for characterization of any kind of explosive material.

The manufacturing of an inert material that has the same permittivity of the ANFO explosive was done by mixing dielectric materials. Furthermore, fabrication of surrogate objects of Colombian IEDs types was developed satisfactorily by using this inert developed material. Surrogate objects, such as those manufactured in this research, can be used to test electromagnetic detection devices.

5.3 Future work

In general, the proposed classifications methods are promising for IEDs classification in the humanitarian demining scenario. However, further field measurements are required in order to train all the proposed classifiers under more test conditions and with a higher number of target samples. In fact, other machine learning techniques can be tested and compared with the SMV presented here.

Polarimetric GPR measurements are useful to increase the number of features extracted from the backscattered signal of buried targets. However, the quality of the data is affected by the clutter removal stage and data processing. Strategies as tilt the antenna incidence angle decrease the undesired effects of ground reflections. However, optimal off-normal incidence angle should be calculated and adjusted in an optimal way, for example, using the soil permittivity properties combined with preliminary GPR measurements of know targets.

Development of clutter removal algorithms applied in polarimetric GPR measurements and improvement of the techniques to increase the signal to clutter ratio are still topics of investigation. However, special care should be taken with the effects that these procedures and techniques produce on the feature extraction and classification performance.

The complex permittivity measurements of improvised ANFO explosives can be used to improve the electromagnetic models of IEDs. Furthermore, the results evince that these measurements could be used as an identification mechanism aimed to classify the explosives by their origin, however, further research is required.

Construction of a hand-held dual detector can be done in future research by combining the UWB-MIMO-GPR and metal detector. Additionally, the proposed polarimetric features and additional features extracted from the metal detector can be integrated into a classification algorithm.

Appendix A. Surrogate IEDs

In order to manufacture inert surrogates of IEDs, an inert material was developed by mixing a casting resin with Barium Titanate ($BaTiO_3$), where the resin was used as host material and the $BaTiO_3$ as inclusion material. Consequently, the permittivity of the produced material is the total effect of the dielectric mixing of these ingredients. Basically, the host material permittivity is modified with the variation in the percentage of the inclusion added.

Since the ingredients used in the mixture have unknown permittivities, then materials were manufactured for different percentages of inclusion. Afterward, the permittivities of the produced materials were measured and a mixing equation curve was calculated, as explained in [78] an depicted in Figure A-1.

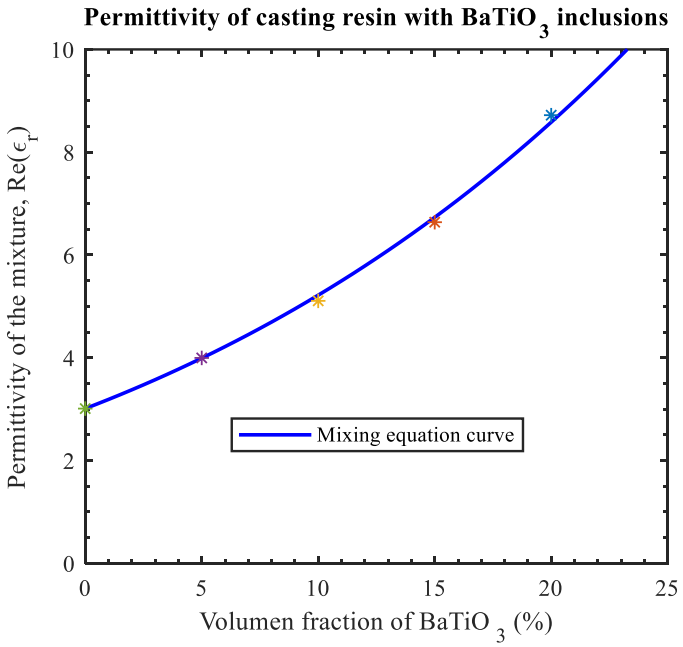

Figure A-1: Permittivity of casting resin with $BaTiO_3$ inclusions.

In order to produce a material with similar dielectric properties to ANFO, the results presented in section 2.6 were used in the mixture curve shown in Figure A-1. Therefore, the required volume fraction of the inclusion material $BaTiO_3$ can be between 6.5% and 7.5%. Figure A-2 shows the manufacturing process stage where the air inclusions are extracted from the liquid mixture by using a vacuum chamber. However, the final appearance of the material is solid.

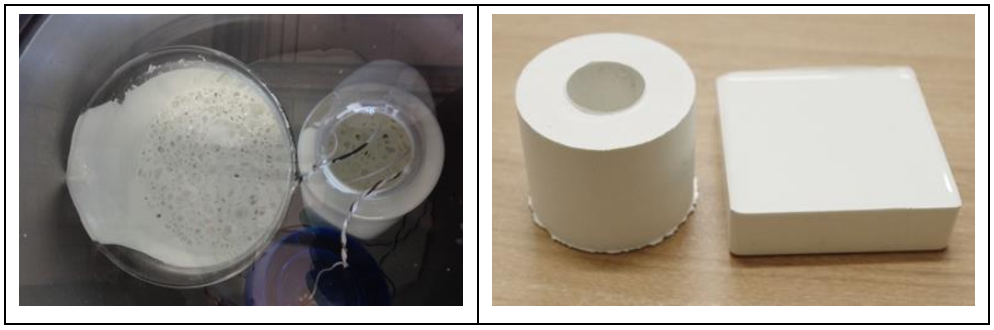

(a) (b)

Figure A-2: Inert material in two stages of manufacturing: a) Liquid stage during air extraction, b) solid stage in the final process.

The inert material sample of Figure A-2 has a volume fraction of 6.5% and its permittivity has similar dielectric properties to ANFO, as shown in Figure A-3.

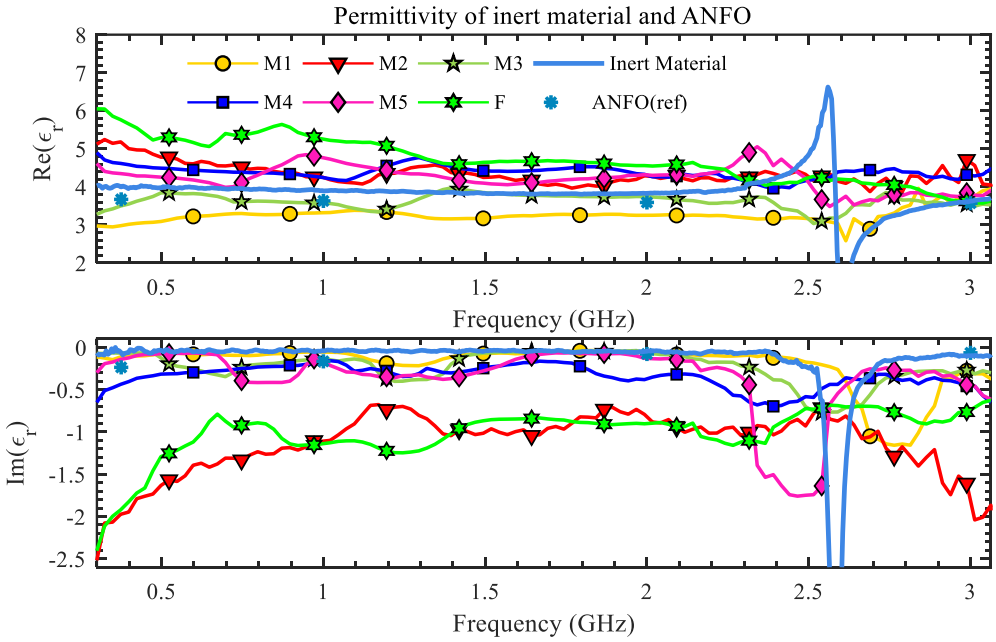

Figure A-3: Permittivity of inert material compared to ANFO measurements.

Finally, in order to set up radar test targets, several IEDs were filled with the processed surrogate material. The inert surrogate IEDs and clutter objects used for radar measurements are shown in Figure A-4 and Figure A-5.

IEDs	Clutter objects
Image removed by the author	

Figure A-4: Surrogate inert IEDs and clutter objects used for laboratory measurements.

IEDs	Clutter objects
Image removed by the author	

Figure A-5: Surrogate inert IEDs and clutter objects used for field measurements.

Appendix B. Time-frequency transformations and data processing methods

Time-frequency transformations applied to polarimetric measurements are presented in this section. In general, each target has a particular polarimetric time-frequency representation and their differences are managed with the polarimetric feature extraction and SVM classification approach. Consequently, the images presented in this section only have illustrative purposes to show the time-frequency representation of the eight data processing methods described in Table 4-2. Additionally, an SVD polarimetric image approximation of a time-frequency representation is also presented.

Figure B-1 to Figure B-5 shows time-frequency transformations applied in a polarimetric A-scan. The data are extracted from field19 measurement for the IED_2. We can see in Figure B-1 that the WVD representation obtained with RLS and LPC data processing methods are different from each other. However, both data processing methods with the WVD transformation produce a distribution of energy in a well-defined dense zone in the time-frequency plane. Notice that the time-frequency transformations are applied after clutter removal and to not normalized polarimetric data, as explained in the second step of the procedure described in section 4.4. In fact, if the time-frequency transformations are applied to normalized polarimetric data, then the energy distribution is spread and no dense region can be identified, as shown in Figure B-2. In other words, some procedures as normalization enhance, in the B-scan, the discontinuity produced by the targets. However, some of these procedures are not useful in feature extraction and must be used as a separate data processing, i.e. only for localization of target discontinuity and not in the extraction of target features.

Additionally, time-frequency transformations using the Morse, Morlet and Bump CWT are presented in Figure B-3, Figure B-4 and Figure B-5, respectively. In general, the CWT transformations provide different time and frequency resolutions between each other. However, the distribution of energy is concentrated in a dense region, which allows the extraction of target features.

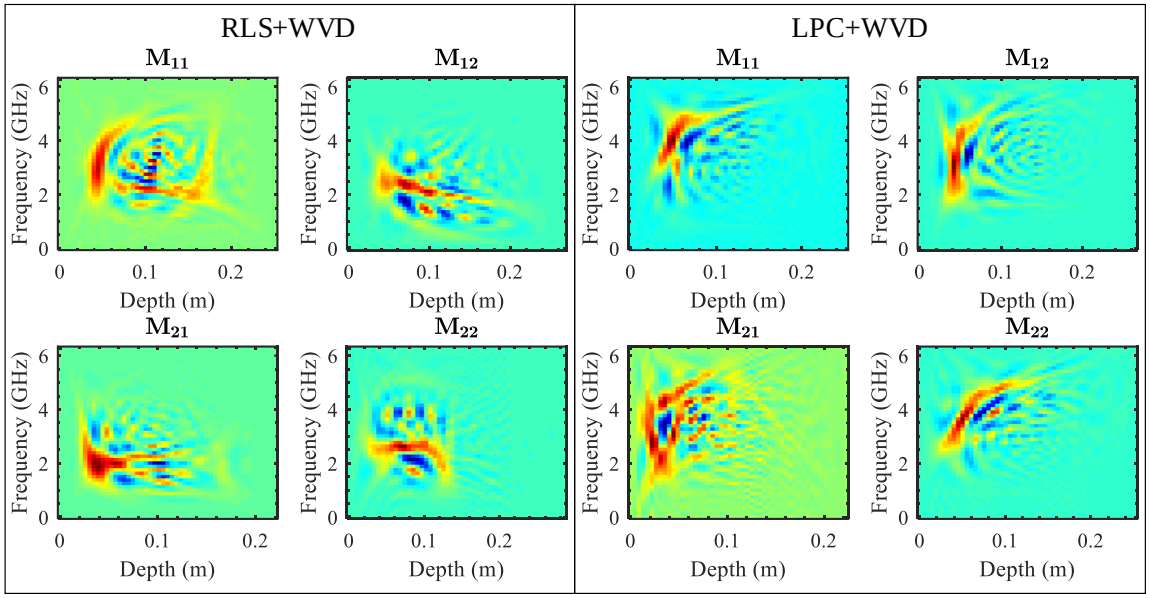

Figure B-1: Results of WVD applied in polarimetric data processed with a) RLS filter and b) LPC filter. The time-domain is expressed in term of depth (m). The energy distribution is concentrated in regions where the time-frequency resolution allows identification of the target position and its frequency components.

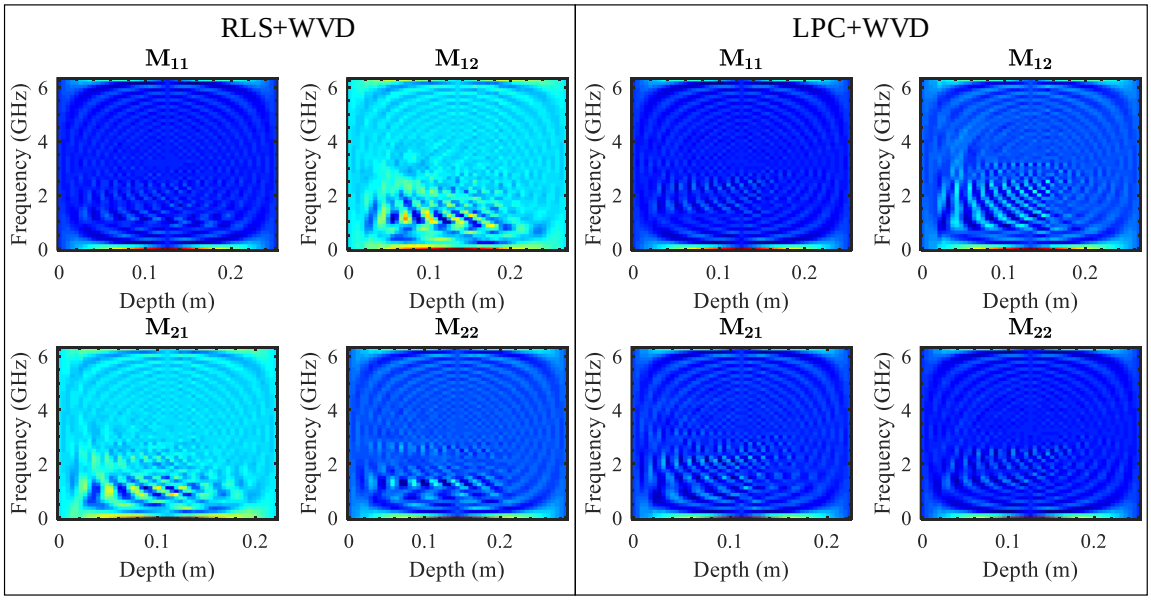

Figure B-2: Results of WVD applied after normalize polarimetric data processed with a) RLS filter and b) LPC filter. The energy distribution is spread in the whole time-frequency plane and the target position and its frequency components are not identified.

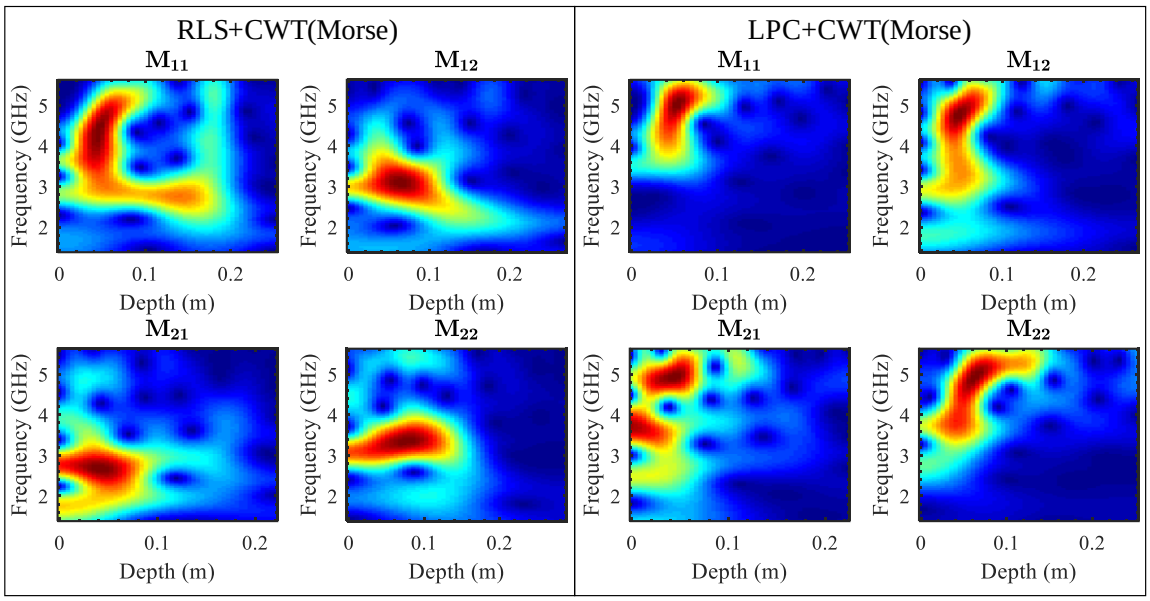

Figure B-3: Results of Morse CWT applied in the data processed with a) RLS filter and b) LPC filter. The energy distribution is localized in dense regions in the time-frequency plane. The frequency components detected by the RLS filter data processing are different from those that use the LPC filter.

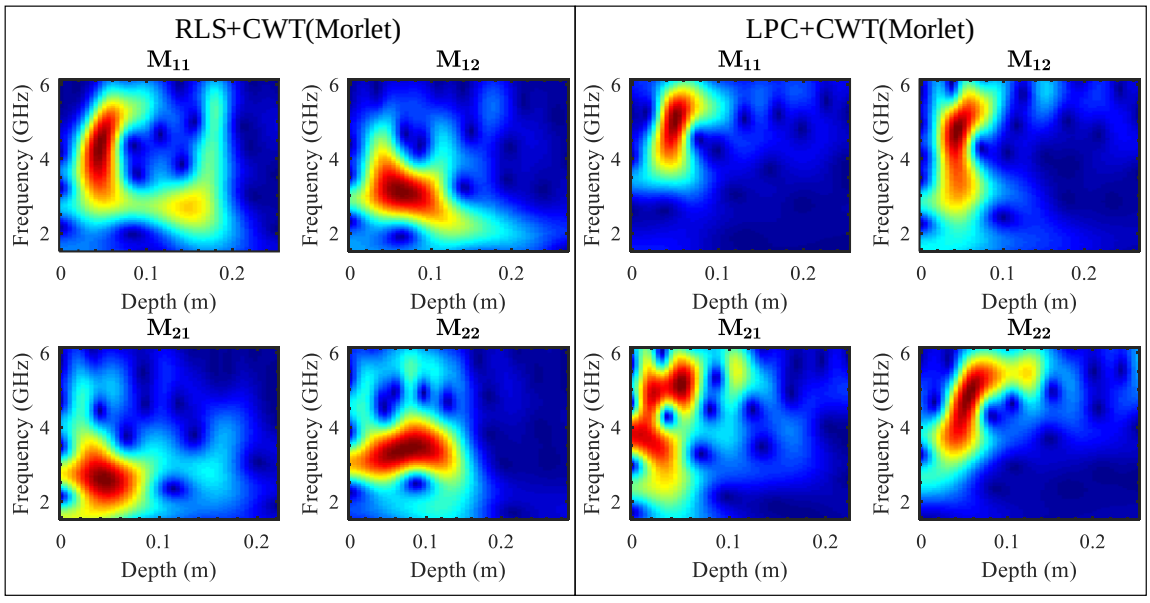

Figure B-4: Results of Morlet CWT applied in the data processed with a) RLS filter and b) LPC filter. The energy is localized in dense regions in the time-frequency plane. In this case, the results are similar to those produced by the Morse CWT.

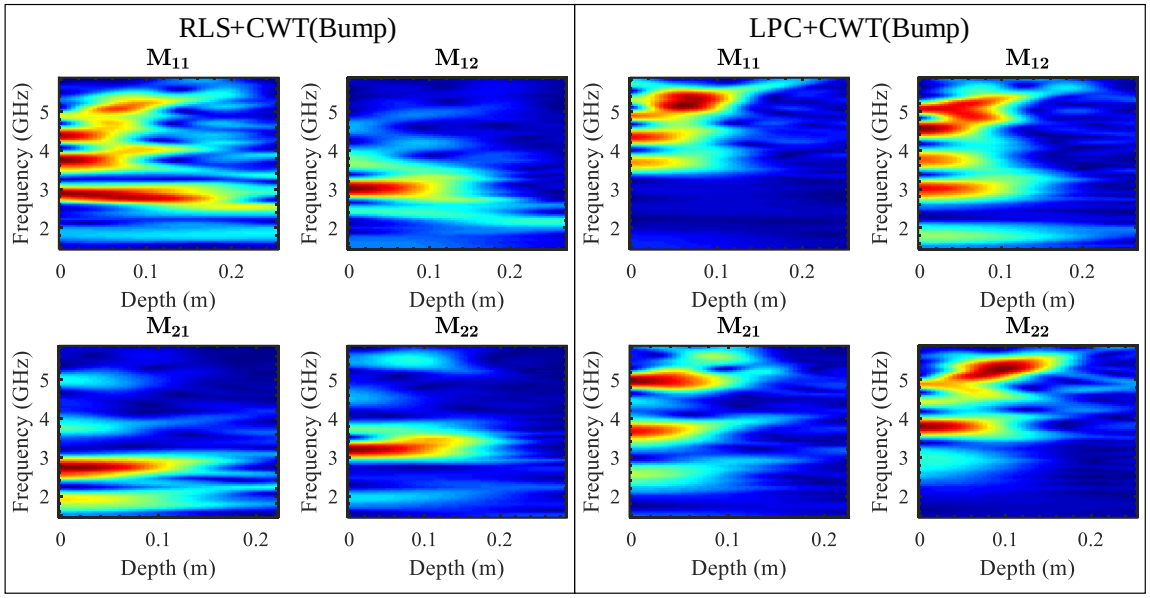

Figure B-5: Results of Bump CWT applied in the data processed with a) RLS filter and b) LPC filter. The time-frequency resolution is low and the target position is difficult to be identified.

In this research, the SVD is used to approximate each individual submatrix **M** of the polarimetric time-frequency representation by using A_k images. This image decomposition is part of the steps required to extract target features, as explained in section 4.3. In general, the images A_k are used to extract the singular parameters $\delta_{t,k}, \delta_{f,k}, \delta_{e,k}$, by using equations (4.17), (4.18) and (4.21).

Figure B-6 to Figure B-9 use the results of the WVD transformations applied to a polarimetric A-scan processed with the RLS filter. The data are extracted from the measurement of sandbox174 for the IED_{16}. We can see the image approximations after the SVD is applied to the time-frequency representation, and the most energetic components are used. Additionally, we can observe each of the first A_k images, as defined in Equation (4.14). Figure B-6 shows the approximation of M using the first A_k component. We can observe that the time and frequency components are well-localized in all the polarizations. Moreover, as the number of images increased, the approximation to the original time-frequency representation is improved and more information is extracted from the polarimetric time-frequency transformation, as depicted in Figure B-7 and Figure B-8. In fact, using the first five A_k images, the approximation is around 70% of the original image.

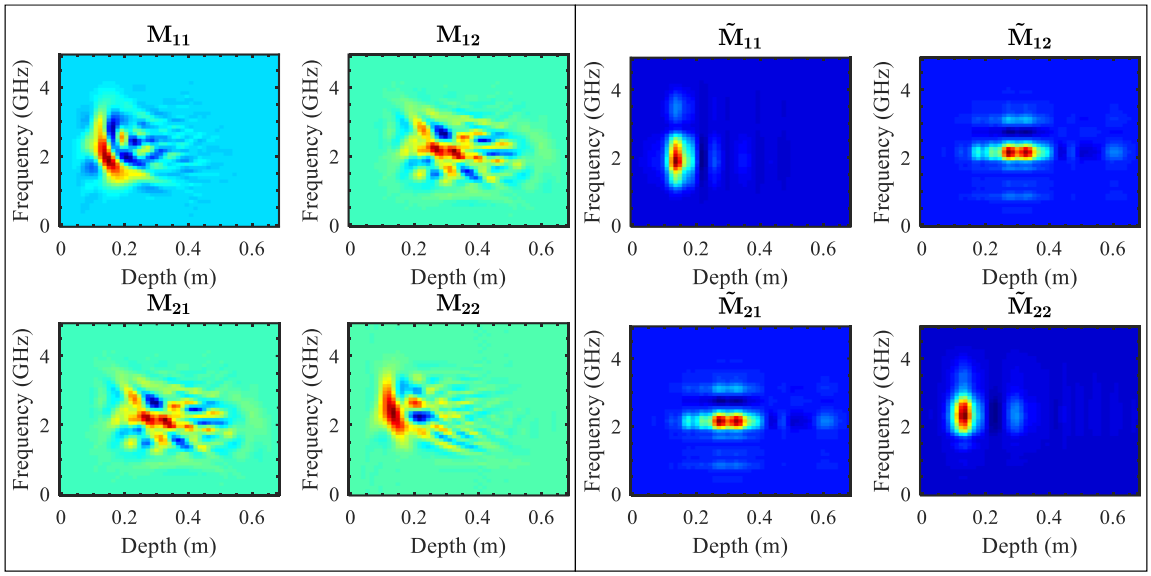

Figure B-6: Polarimetric time-frequency representation. a) Original time-frequency representation, b) time-frequency approximation using the SVD and the first A_k image (A_1). The target is well localized in the time-frequency plane. The main frequency components of this target are localized at 2 GHz and it is equal in all the $\tilde{M}$ images.

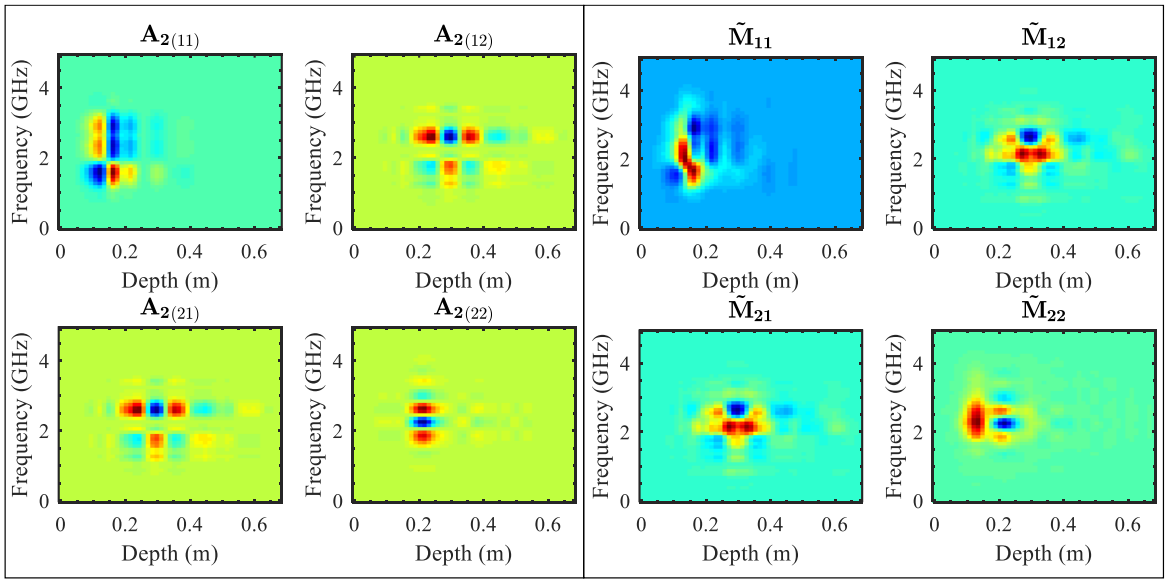

Figure B-7: Polarimetric time-frequency representation. a) Polarimetric representation of the second image component of the SVD (A_2), b) Time-frequency approximation using the first two A_k images $(A_1 + A_2)$.

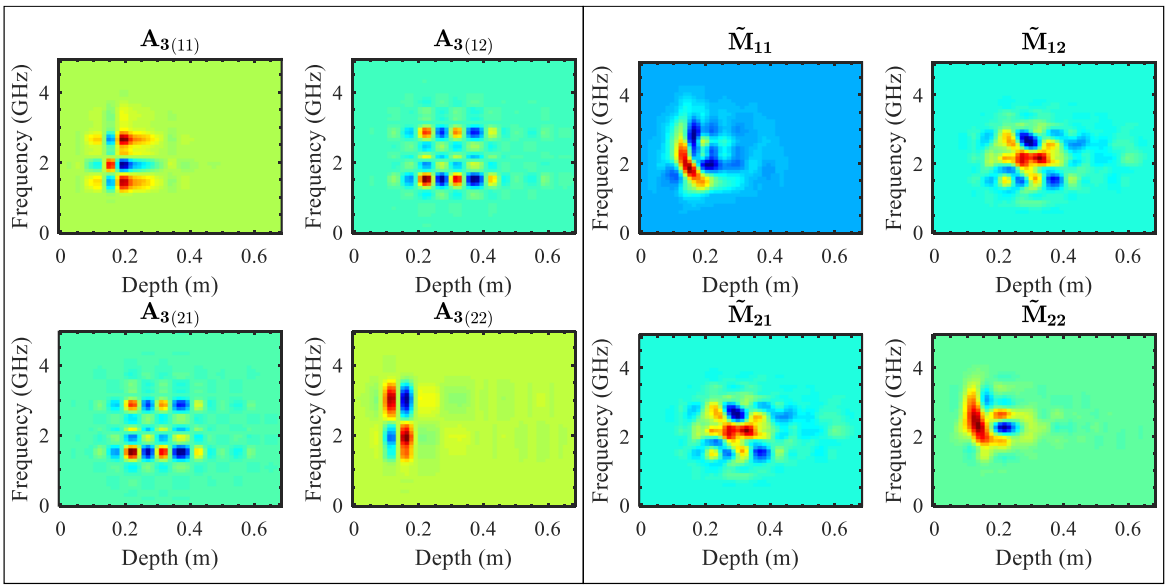

(a) (b)

Figure B-8: Polarimetric time-frequency representation. a) Polarimetric representation of the third image component of the SVD (A_3), b) Time-frequency approximation using the first three A_k images $(A_1+A_2+A_3)$. Several time-frequency components are well identified.

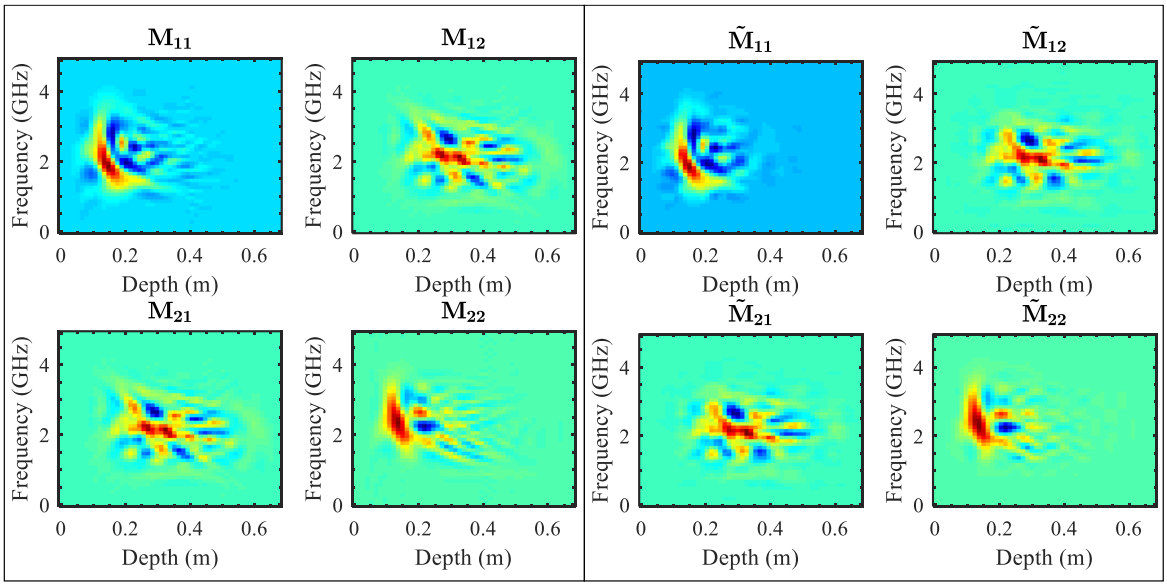

(a) (b)

Figure B-9: Polarimetric time-frequency representation. a) Original time-frequency representation, b) Time-frequency approximation using the first five A_k images $(A_1+\cdots+A_5)$.

Appendix C. List of publications

Journal paper

S. Gutierrez, T. Just, J. Sachs, C. Baer, and F. Vega, 'Field-Deployable System for the Measurement of Complex Permittivity of Improvised Explosives and Lossy Dielectric Materials', IEEE Sensors Journal, vol. 18, no. 16, pp. 6706–6714, 2018. DOI: 10.1109/JSEN.2018.2849322.

S. Gutierrez, F. Vega, F.A. González, C. Baer, and J. Sachs, 'Application of Polarimetric Features and Support Vector Machines for Classification of Improvised Explosive Devices', IEEE Antennas and Wireless Propagation Letters. pp. 1–4, 2019. DOI: 10.1109/LAWP.2019.2934691.

Conference papers

C. Baer, C. Schulz, T. Just, S. Gutierrez et al., 'Humanitarian Microwave Detection of Improvised Explosive Devices in Colombia', in Proceedings of the 2018 20th International Conference on Electromagnetics in Advanced Applications, ICEAA 2018, 2018, pp. 372–375. DOI: 10.1109/ICEAA.2018.8520508.

C. Baer, S. Gutierrez, J. Jebramcik, J. Barowski, F. Vega, and I. Rolfes, 'Ground penetrating synthetic aperture radar imaging providing soil permittivity estimation', in IEEE MTT-S International Microwave Symposium Digest, 2017. DOI: 10.1109/MWSYM.2017.8058868.

S. Gutierrez, T. Just, J. Sach, C. Baer, F. Vega, and R. Bustamante, 'Permittivity of improvised explosives made of ammonium nitrate and fuel oil', Europe Electromagnetic Conference. EUROEM 2016, 2016.

S. A. Gutierrez, E. Neira, J. J. Pantoja, and F. Vega, 'The effect of ANFO on the Complex Resonance Frequencies of an IED', in Asia Electromagnetic Conference. ASIAEM, 2015.

Bibliography

[1] United Nations Mine Action Service, 'International Mine Action Standards 04.10. Glossary of mine action terms, definitions and abbreviations'. United Nations Mine Action Service, New York, p. 44, 2019.

[2] United Nations Mine Action Service, 'United Nations Improvised Explosive Device Disposal Standards'. p. 135, 2018.

[3] Colombian Army, 'Colombian Army News', 2015. [Online]. Available: https://www.ejercito.mil.co/?idcategoria=32. [Accessed: 02-Apr-2015].

[4] Descontamina Colombia, 'Víctimas de Minas Antipersonal y Municiones sin Explosionar', 2019. [Online]. Available: http://www.accioncontraminas.gov.co/estadisticas/Paginas/victimas-minas-antipersonal.aspx. [Accessed: 16-Apr-2019].

[5] J. M. H. Hendrickx, A. Molina, D. Diaz, M. Grasmueck, H. A. Moreno, and R. D. Hernández, 'Humanitarian IED clearance in Colombia', *Proc. SPIE*, vol. 6953, pp. 69530C-69530C–9, 2008.

[6] Descontamina Colombia, 'Subcomisión Técnica unifica las cifras de víctimas de minas antipersonal en Colombia', 2018. [Online]. Available: http://www.accioncontraminas.gov.co/prensa/2018/Paginas/181228-Subcomision-Tecnica-unifica-cifras-de-victimas-de-MAP-en-Colombia.aspx. [Accessed: 16-Apr-2019].

[7] Landmine and Cluster Munition Monitor, 'Colombia casualties', 2018. [Online]. Available: http://www.the-monitor.org/en-gb/reports/2019/colombia/casualties.aspx. [Accessed: 16-Apr-2019].

[8] Landmine and Cluster Munition Monitor, 'Colombia Support for Mine Action', 2018. [Online]. Available: http://www.the-monitor.org/en-gb/reports/2019/colombia/support-for-mine-action.aspx#ftnref1. [Accessed: 16-Apr-2019].

[9] Landmine and Cluster Munition Monitor, 'Colombia mine action', 2018. [Online]. Available: http://www.the-monitor.org/en-gb/reports/2019/colombia/mine-action.aspx. [Accessed: 17-Apr-2019].

[10] Descontamina Colombia, 'Estadísticas de desminado humanitario', 2019. [Online]. Available: http://www.accioncontraminas.gov.co/estadisticas/Paginas/Estadisticas-Desminado-Humanitario.aspx. [Accessed: 17-Apr-2019].

[11] Descontamina Colombia, 'Estándares Nacionales de Acción Integral Contra Minas Antipersonal - AICMA', 2017. [Online]. Available: http://www.accioncontraminas.gov.co/accion/Paginas/Estandares-Nacionales-AICMA.aspx. [Accessed: 17-Apr-2019].

[12] Descontamina Colombia, 'Desminado Humanitario', 2019. [Online]. Available: http://www.accioncontraminas.gov.co/accion/desminado/Paginas/Desminado-Humanitario.aspx. [Accessed: 16-Apr-2019].

[13] Descontamina Colombia, 'Técnica de despeje manual'. p. 12, 2018.

[14] H. Kasban, O. Zahran, S. M. Elaraby, M. El-Kordy, and F. E. Abd El-Samie, 'A Comparative Study of Landmine Detection Techniques', *Sens. Imaging An Int. J.*, vol. 11, no. 3, pp. 89–

112, Sep. 2010.
[15] J. (Ed. . Byrnes, *Unexploded Ordnance Detection and Mitigation*. Dordrecht: Springer Netherlands, 2009.
[16] D. J. Daniels and I. of Electrical Engineers, *Ground Penetrating Radar*, no. v. 1. Institution of Engineering and Technology, 2004.
[17] GICHD, 'Guidebook on Detection Technologies and Systems for Humanitarian Demining'. 2006.
[18] C. E. Baum, *Detection and identification of visually obscured targets*. Taylor & Francis, 1999.
[19] L. Peters, J. J. Daniels, and J. D. Young, 'Ground penetrating radar as a subsurface environmental sensing tool', *Proc. IEEE*, vol. 82, no. 12, pp. 1802–1822, 1994.
[20] A. P. Annan, 'Chapter 1 - Electromagnetic Principles of Ground Penetrating Radar', in *Ground Penetrating Radar Theory and Applications*, H. M. Jol, Ed. Amsterdam: Elsevier, 2009, pp. 1–40.
[21] J. Sachs, *Handbook of Ultra-wideband Short-range Sensing: Theory, Sensors, Applications*. John Wiley & Sons, 2013.
[22] H. M. Jol, Ed., *Ground penetrating radar theory and applications*. Elsevier, 2008.
[23] K. Takahashi, J. Igel, and H. Preetz, 'Clutter Modeling for Ground-Penetrating Radar Measurements in Heterogeneous Soils', *Sel. Top. Appl. Earth Obs. Remote Sensing, IEEE J.*, vol. 4, no. 4, pp. 739–747, 2011.
[24] L. M. van Kempen, H. Sahli, J. Brooks, and J. P. Cornelis, 'New results on clutter reduction and parameter estimation for land mine detection using GPR', in *Proc. SPIE 4084. 8th Int. Conf. Ground Penetrating Radar*, 2000, pp. 872–879.
[25] O. Lopera, E. C. Slob, N. Milisavljevic, and S. Lambot, 'Filtering Soil Surface and Antenna Effects From GPR Data to Enhance Landmine Detection', *IEEE Trans. Geosci. Remote Sens.*, vol. 45, no. 3, pp. 707–717, Mar. 2007.
[26] Bart Scheers, 'Ultra-Wideband Ground Penetrating Radar, with Application to the Detection of Anti Personnel Landmines', Université Catholique De Louvain, Royal Military Academy, 2001.
[27] L. van Kempen and H. Sahli, 'Signal processing techniques for clutter parameters estimation and clutter removal in GPR data for landmine detection', in *Proc. 11th IEEE Signal Process. Workshop Statistical Signal Process. (Cat. No.01TH8563)*, 2001, pp. 158–161.
[28] K. Furuta and J. Ishikawa, *Anti-personnel landmine detection for humanitarian demining*. Springer, 2009.
[29] F. Soldovieri, O. Lopera, and S. Lambot, 'Combination of Advanced Inversion Techniques for an Accurate Target Localization via GPR for Demining Applications', *IEEE Trans. Geosci. Remote Sens.*, vol. 49, no. 1, pp. 451–461, Jan. 2011.
[30] L. Van Kempen and H. Sahli, 'Ground penetrating radar data processing: a selective survey of the state of the art literature', Brussels, 1999.
[31] T. U. Gurbuz, B. Aslanyurek, E. P. Karabulut, and I. Akduman, 'An Efficient Nonlinear Imaging Approach for Dielectric Objects Buried Under a Rough Surface', *Geosci. Remote Sensing, IEEE Trans.*, vol. 52, no. 5, pp. 3013–3022, May 2014.
[32] C. E. Baum, 'Identification of buried unexploded ordnance', in *2008 International Conference on Radar*, 2008, pp. 17–18.
[33] T. G. Savelyev, L. van Kempen, H. Sahli, J. Sachs, and M. Sato, 'Investigation of Time/Frequency Features for GPR Landmine Discrimination', *Geosci. Remote Sensing, IEEE Trans.*, vol. 45, no. 1, pp. 118–129, 2007.
[34] K. H. Ko, G. Jang, K. Park, and K. Kim, 'GPR-based landmine detection and identification using multiple features', *Int. J. Antennas Propag.*, vol. 2012, 2012.

[35] G. Alli, C. Bonopera, A. Sarri, G. Pinelli, and G. De Pasquale, 'Data processing for mine-detection polarimetric ground penetrating radar array', in *Proceedings of the Tenth International Conference on Grounds Penetrating Radar, 2004. GPR 2004.*, 2004, pp. 669–672.

[36] J. Sachs, P. Peyerl, and G. Alli, 'Ultra-wideband polarimetric GPR-array stimulated by pseudo random binary codes', in *Proceedings of the Tenth International Conference on Grounds Penetrating Radar, 2004. GPR 2004.*, 2004, vol. 1, pp. 163–166.

[37] S. Gutierrez, T. Just, J. Sachs, C. Baer, and F. Vega, 'Field-Deployable System for the Measurement of Complex Permittivity of Improvised Explosives and Lossy Dielectric Materials', *IEEE Sens. J.*, vol. 18, no. 16, pp. 6706–6714, 2018.

[38] S. A. Gutierrez, E. Neira, J. J. Pantoja, and F. Vega, 'The effect of ANFO on the Complex Resonance Frequencies of an IED', in *Asia Electromagn. Conf. ASIAEM*, 2015.

[39] A. H. Boughriet, C. Legrand, and A. Chapoton, 'Noniterative stable transmission/reflection method for low-loss material complex permittivity determination', *{IEEE} Trans. Microw. Theory Techn.*, vol. 45, no. 1, pp. 52–57, 1997.

[40] J. Baker Jarvis, E. J. Vanzura, and W. A. Kissick, 'Improved technique for determining complex permittivity with the transmission/reflection method', *{IEEE} Trans. Microw. Theory Techn.*, vol. 38, no. 8, pp. 1096–1103, 1990.

[41] J. J. Baker *et al.*, 'Measuring the Permittivity and Permeability of Lossy Materials: Solids, Liquids, Metals, Building Materials, and Negative-index Materials', *NIST Tech. Note.*, vol. 1536, 2005.

[42] K. Chalapat, K. Sarvala, J. Li, and G. S. Paraoanu, 'Wideband Reference-Plane Invariant Method for Measuring Electromagnetic Parameters of Materials', *{IEEE} Trans. Microw. Theory Techn.*, vol. 57, no. 9, pp. 2257–2267, Sep. 2009.

[43] U. C. Hasar and C. R. Westgate, 'A Broadband and Stable Method for Unique Complex Permittivity Determination of Low-Loss Materials', *{IEEE} Trans. Microw. Theory Techn.*, vol. 57, no. 2, pp. 471–477, Feb. 2009.

[44] U. C. Hasar, 'Explicit Permittivity Determination of Medium-Loss Materials From Calibration-Independent Measurements', *{IEEE} Sensors J*, vol. 16, no. 13, pp. 5177–5182, 2016.

[45] C. Wan, B. Nauwelaers, W. De Raedt, and M. Van Rossum, 'Two new measurement methods for explicit determination of complex permittivity', *{IEEE} Trans. Microw. Theory Techn.*, vol. 46, no. 11, pp. 1614–1619, Nov. 1998.

[46] M. D. Janezic and J. A. Jargon, 'Complex permittivity determination from propagation constant measurements', *IEEE Microw. Guid. Wave Lett.*, vol. 9, no. 2, pp. 76–78, Feb. 1999.

[47] A. L. Higginbotham Duque, W. L. Perry, and C. M. Anderson-Cook, 'Complex Microwave Permittivity of Secondary High Explosives', *Propellants, Pyrotech., Explos.*, vol. 39, no. 2, pp. 275–283, 2014.

[48] M. E. Daily, B. B. Glover, S. F. Son, and L. J. Groven, 'X-Band Microwave Properties and Ignition Predictions of Neat Explosives', *Propellants, Pyrotech., Explos.*, vol. 38, no. 6, pp. 810–817, 2013.

[49] B. W. VanderGaast, J. E. McFee, K. L. Russell, and A. A. Faust, 'Design and validation of inert homemade explosive simulants for ground penetrating radar', *Proc. SPIE*, vol. 9454, pp. 945412–945413, 2015.

[50] K. C. Yaw, 'Measurement of dielectric material properties', *Appl. Note. Rohde Schwarz*, 2012.

[51] L. F. Chen, C. K. Ong, C. P. Neo, V. V Varadan, and V. K. Varadan, *Microwave Electronics: Measurement and Materials Characterization*. West Sussex, U.K.: Wiley, 2004.

[52] A. V Oppenheim and R. W. Schafer, *Discrete-Time Signal Processing*, 3rd ed. Upper Saddle River, NJ, USA: Prentice Hall Press, 2009.
[53] D. K. Rytting, 'Appendix to an analysis of vector measurement accuracy enhancement techniques', in *Hewlett-Packard RF & Microw. Meas. Symp. Exhib.*, 1982.
[54] J. Sachs, P. Peyerl, and M. Rossberg, 'A new UWB-principle for sensor-array application', in *Proc. IEEE Instrum. Meas. Technol. Conf. IMTC/99.*, 1999, vol. 3, pp. 1390–1395 vol.3.
[55] J. Sachs, M. Kmec, R. Herrmann, M. Helbig, and K. Schilling, 'Integrated pseudo-noise device with network analyzer performance for UWB sensing and component test', in *Int. Symp. Signals, Syst., Electron.(ISSSE)*, 2012, pp. 1–6.
[56] E. G. Mahadevan, *Ammonium nitrate explosives for civil applications: slurries, emulsions and ammonium nitrate fuel oils*. John Wiley & Sons, 2013.
[57] S. Gutierrez, F. Vega, F. A. Gonzalez, C. Baer, and J. Sachs, 'Application of Polarimetric Features and Support Vector Machines for Classification of Improvised Explosive Devices', *IEEE Antennas Wirel. Propag. Lett.*, pp. 1–1, 2019.
[58] D. J. Daniels, P. Curtis, and O. Lockwood, 'Classification of landmines using GPR', in *Radar Conference, 2008. RADAR '08. IEEE*, 2008, pp. 1–6.
[59] H. Frigui, L. Zhang, and P. D. Gader, 'Context-Dependent Multisensor Fusion and Its Application to Land Mine Detection', *Geosci. Remote Sensing, IEEE Trans.*, vol. 48, no. 6, pp. 2528–2543, 2010.
[60] A. Yarovoy, 'Chapter 14 - Landmine and Unexploded Ordnance Detection and Classification with Ground Penetrating Radar', in *Ground Penetrating Radar Theory and Applications*, H. M. Jol, Ed. Amsterdam: Elsevier, 2009, pp. 445–478.
[61] T. G. Savelyev, L. van Kempen, and H. Sahli, 'GPR antipersonnel mine detection: improved deconvolution and time-frequency feature extraction', in *Proc. SPIE 5046*, 2003, p. 232.
[62] G. T. Tesfamariam, D. Mali, and A. M. Zoubir, 'Clutter reduction techniques for GPR based buried landmine detection', in *Int. Conf. Signal Process. Commun. Comput. Netw. Technol. ICSCCN*, 2011, pp. 182–186.
[63] C. Baer, T. Musch, C. Schulz, and I. Rolfes, 'A polarimetrie, low ringing UWB antenna for ground penetrating radar operation', in *2016 IEEE Int. Symp. Antennas and Propagation (APSURSI)*, 2016, pp. 2121–2122.
[64] T. G. Savelyev, T. Kobayashi, X. Feng, and M. Sato, 'Robust target discrimination with UWB GPR', in *Ultra-Wideband, Short-Pulse Electromagnetics 7*, Springer, 2007, pp. 732–739.
[65] K. A. Lee, W. S. Gan, and S. M. Kuo, *Subband Adaptive Filtering: Theory and Implementation*. Wiley, 2009.
[66] S. S. Haykin, *Adaptive Filter Theory*. Prentice Hall, 2002.
[67] V. MADISETTI, *The Digital Signal Processing Handbook*. Taylor & Francis, 1997.
[68] J. J. Pantoja, N. Pena, F. Rachidi, F. Vega, and F. Roman, 'Susceptibility of Electro-explosive Devices to Microwave Interference', *Def. Sci. J.*, vol. 63, no. 4, pp. 386–392, Jul. 2013.
[69] S. Abrahamsson, B. Brusmark, H. C. Strifors, and G. C. Gaunaurd, 'Extraction of target signature features in the combined time-frequency domain by means of impulse radar', in *SPIE Defense, Security, and Sensing*, 1992, pp. 102–113.
[70] Y. Sun and J. Li, 'Time–frequency analysis for plastic landmine detection via forward-looking ground penetrating radar', *IEE Proc. - Radar, Sonar Navig.*, vol. 150, no. 4, p. 253, 2003.
[71] L. Van Kempen, 'Signal processing and pattern recognition methods for radar AP mine detection and identification', in *2th Int. Conf. Detection Abandoned Land Mines*, 1998, vol. 1998, pp. 81–85.
[72] T. G. Savelyev and M. Sato, 'Comparative analysis of UWB deconvolution and feature-

extraction algorithms for GPR landmine detection', in *Proc. SPIE 5415*, 2004, p. 1008.
[73] V. C. Chen and H. Ling, *Time-frequency transforms for radar imaging and signal analysis*. Artech House, 2002.
[74] T. Claasen, 'The Wigner distribution—A tool for time-frequency signal analysis', *Philips J. Res*, vol. 35, no. 3, pp. 217–250, 1980.
[75] L. Cohen, 'Time-frequency distributions-a review', *Proc. IEEE*, vol. 77, no. 7, pp. 941–981, Jul. 1989.
[76] B. Boashash, *Time-Frequency Signal Analysis and Processing: A Comprehensive Reference*. Elsevier Science, 2015.
[77] E. Alpaydin, *Introduction to machine learning*, 2nd ed. MIT press, 2010.
[78] B. Hattenhorst, M. Mallach, C. Baer, T. Musch, J. Barowski, and I. Rolfes, 'Dielectric phantom materials for broadband biomedical applications', in *2017 First IEEE MTT-S International Microwave Bio Conference (IMBIOC)*, 2017, pp. 1–4.